The Stability and Slow Dynamics of Spot Patterns in the 2D Brusselator Model: The Effect of Open Systems and Heterogeneities

J. C. Tzou*, M. J. Ward †

February 2, 2018

Abstract

Spot patterns, whereby the activator field becomes spatially localized near certain dynamically-evolving discrete spatial locations in a bounded multi-dimensional domain, is a common occurrence for two-component reaction-diffusion (RD) systems in the singular limit of a large diffusivity ratio. In previous studies of 2-D localized spot patterns for various specific well-known RD systems, the domain boundary was assumed to be impermeable to both the activator and inhibitor, and the reaction-kinetics were assumed to be spatially uniform. As an extension of this previous theory, we use formal asymptotic methods to study the existence, stability, and slow dynamics of localized spot patterns for the singularly perturbed 2-D Brusselator RD model when the domain boundary is only partially impermeable, as modeled by an inhomogeneous Robin boundary condition, or when there is an influx of inhibitor across the domain boundary. In our analysis, we will also allow for the effect of a spatially variable bulk feed term in the reaction kinetics. By applying our extended theory to the special case of one-spot patterns and ring patterns of spots inside the unit disk, we provide a detailed analysis of the effect on spot patterns of these three different sources of heterogeneity. In particular, when there is an influx of inhibitor across the boundary of the unit disk, a ring pattern of spots can become pinned to a ring-radius closer to the domain boundary. Under a Robin condition, a quasi-equilibrium ring pattern of spots is shown to exhibit a novel saddle-node bifurcation behavior in terms of either the inhibitor diffusivity, the Robin constant, or the ambient background concentration. A spatially variable bulk feed term, with a concentrated source of "fuel" inside the domain, is shown to yield a saddle-node bifurcation structure of spot equilibria, which leads to qualitatively new spot-pinning behavior. Results from our asymptotic theory are validated from full numerical simulations of the Brusselator model.

1 Introduction

Localized spot patterns, whereby a solution component becomes concentrated near certain dynamically-evolving discrete spatial locations in a bounded multi-dimensional domain, is a well-known phenomena for certain two-component reaction-diffusion (RD) systems in the singular limit of a large diffusivity ratio (cf. [3, 11, 13, 20, 22, 28–32, 36]). As surveyed in [27], localized spot patterns arise in many diverse physical and chemical experiments, and they represent a particular class of "far-from equilibrium" patterns [17]. Spot patterns can exhibit a rather wide variety of instabilities such as spot self-replication, spot annihilation due to overcrowding effects, and spot amplitude temporal oscillations, all of which can, typically, be triggered through dynamic bifurcations resulting from the slow spot evolution. In 2-D spatial domains, the stability and dynamics of localized spot patterns have been analyzed for many prototypical RD systems, including the Gierer-Meinhardt (GM) model [11, 28, 29], the Gray-Scott model [3, 30, 31], the Schnakenberg model [13, 32, 36], and the Brusselator model posed on the boundary of the unit sphere [20, 22]. More recently, in [25], the Schnakenberg model was used to provide the first study of spot stability and dynamics in a bounded 3-D domain. A more extensive set of references for the analysis of 2-D spot patterns, and corresponding 1-D spike patterns, is given in the references of these cited articles and in the monograph [35].

The primary new focus of this paper is to provide the first systematic analysis of 2-D spot patterns for a RD system that accounts for some exchange of material between a bounded 2-D domain and the outside environment. Previous studies

*Dept. of Mathematics, University of British Columbia, Vancouver, BC, Canada tzou.justin@gmail.com
†Dept. of Mathematics, University of British Columbia, Vancouver, BC, Canada ward@math.ubc.ca

of spot patterns in a 2-D domain have considered only "closed" systems, modeled by homogeneous Neumann boundary conditions, where the domain boundary is impermeable. While in many cases this may be a realistic assumption, there are other modeling scenarios, such as in skeletal limb development [4], where the boundary is either a source of some chemical morphogen or is only partially impermeable. In the latter case, the boundary is modeled by an inhomogeneous Robin-type condition. We will show that such "open systems" can have rather pronounced effects on the bifurcation properties, stability, and dynamics of localized spot patterns. In our 2-D model we will also consider the effect of a spatially inhomogeneous term in the reaction kinetics, which can lead to new pinning behavior of spot patterns. For concreteness, we will analyze spot patterns for two classes of "open" systems for the classic Brusselator RD model [19] in the singular limit of a large diffusivity ratio, while allowing for a spatially inhomogeneous bulk feed term. We remark that a similar analysis can be done for other RD systems in the large diffusivity ratio limit.

The non-dimensional Brusselator RD model with small activator diffusivity $0 < \varepsilon_0^2 \ll 1$ takes the form [19]

$$U_\sigma = \varepsilon_0^2 \Delta U + \mathcal{E} - (B+1)U + VU^2\,, \qquad V_\sigma = \mathcal{D}\Delta V + BU - VU^2\,; \qquad \sigma > 0\,, \quad \mathbf{x} \in \Omega\,, \tag{1.1a}$$

where the bulk feed $\mathcal{E} = \mathcal{E}(\mathbf{x}) > 0$ is allowed to be spatially dependent. In contrast to the usual analysis of closed systems in which $\partial_n U = \partial_n V = 0$ on the boundary $\partial\Omega$, we will consider two scenarios for the inhibitor V on $\partial\Omega$ that model an exchange of material with the outside environment:

$$\text{(I):} \quad \mathcal{D}\partial_n V = \mathcal{A}\,, \quad \partial_n U = 0\,, \quad \mathbf{x} \in \partial\Omega\,; \qquad \text{(II):} \quad \mathcal{D}\partial_n V + k(V - V_{\rm out}) = 0\,, \quad \partial_n U = 0\,, \quad \mathbf{x} \in \partial\Omega\,. \tag{1.1b}$$

Here, ∂_n denotes the outward normal derivative on $\partial\Omega$. When $\mathcal{A} > 0$ in (1.1b), Case I models influx of the inhibitor from the boundary, while in Case II with $k > 0$ and $V_{\rm out} > 0$, we have influx (leakage) when $V(\mathbf{x}) < V_{\rm out}$ ($V(\mathbf{x}) > V_{\rm out}$) for $\mathbf{x} \in \partial\Omega$. We refer to (1.1a) with boundary conditions I and II as "open" systems in contrast to a closed system with homogeneous Neumann boundary conditions. For these open systems, our goal is to investigate new behavior regarding the existence, dynamics, and stability of spot patterns. As shown in [20, 22], spot patterns occur when $\mathcal{E} = \mathcal{O}(\varepsilon_0)$. Therefore, in (1.1a) we introduce $\mathcal{E} = \varepsilon_0 \mathcal{E}_0 E(\mathbf{x})$, with $\mathcal{E}_0 > 0$, and assume that $\mathcal{A} = \mathcal{O}(\varepsilon_0)$ and $V_{\rm out} = \mathcal{O}(\varepsilon_0)$. We then rescale $U = \mathcal{E}_0 u/\varepsilon_0$, $V = \varepsilon_0 B v/\mathcal{E}_0$, and $\sigma = t/(B+1)$, so that (1.1b) reduces to

$$u_t = \varepsilon^2 \Delta u + \varepsilon^2 E(\mathbf{x}) - u + fvu^2\,, \qquad \tau v_t = D\Delta v + \frac{1}{\varepsilon^2}\left(u - vu^2\right)\,; \qquad t > 0\,, \qquad \mathbf{x} \in \Omega\,, \tag{1.2a}$$

with either of the following two sets of boundary conditions (Case I and Case II):

$$\text{(I):} \quad \partial_n u = 0\,, \quad D\partial_n v = A\,, \quad \mathbf{x} \in \partial\Omega\,; \qquad \text{(II):} \quad \partial_n u = 0\,, \quad \partial_n v + \kappa_0(v - v_b) = 0\,, \quad \mathbf{x} \in \partial\Omega\,; \qquad \kappa_0 \equiv \kappa/D\,. \tag{1.2b}$$

In (1.2a) and (1.2b), the positive $\mathcal{O}(1)$ parameters are

$$f \equiv \frac{B}{B+1} < 1\,, \quad \tau \equiv \frac{(B+1)^2}{\mathcal{E}_0^2}\,, \quad D \equiv \frac{\mathcal{D}(B+1)}{\mathcal{E}_0^2}\,, \quad \mathcal{A} = \varepsilon_0 f \mathcal{E}_0 A\,, \quad \varepsilon \equiv \frac{\varepsilon_0}{\sqrt{B+1}}\,, \quad V_{\rm out} = \frac{\varepsilon_0 B}{\mathcal{E}_0}\,, \quad k \equiv \frac{\mathcal{D}}{D}\kappa\,. \tag{1.2c}$$

There have been relatively few studies of the effect of open systems on pattern formation in RD systems. In [4] a numerical study of an RD system comparing a variety of different boundary conditions was performed, showing that a Robin condition can lead to more predictable transitions between Turing-type patterns as the domain length increases. In [21] the effect of a Robin condition on periodic wave generation for a class of RD systems was analyzed. A boundary flux has also been used to both control and select certain spatio-temporal patterns in specific RD systems (cf. [14], [37]). Boundary fluxes also arise in RD systems that couple nonlinear bulk diffusion to surface diffusion effects [15]. For spike solutions, [2] proves the existence of a new class of near-boundary steady-state spike solutions for the scalar problem $\varepsilon^2\Delta w - w + w^2 = 0$ in a multi-dimensional domain under a Robin boundary condition. For the shadow limit of the GM model, corresponding to a large inhibitor diffusivity, the linear stability properties of this class of near-boundary spikes under a Robin condition was analyzed in [16]. For the singularly perturbed Brusselator model in a 1-D domain, the existence, linear stability, and slow dynamics of spike patterns was analyzed in [23] and [24] for Case I flux-type boundary conditions. One key finding of [23] is that steady-state spikes are located closer to the endpoints of the 1-D spatial domain whenever there is an influx of material from the boundary. The present study can be viewed as an extension of [23] and [24] to 2-D domains, imposing boundary conditions of either type I and II in (1.2b).

A further goal of this paper is to analyze spot-pinning phenomena resulting from a spatially variable bulk feed $E = E(\mathbf{x})$ in (1.2a). For the 1-D GM model, spike-pinning behavior resulting from a piecewise constant inhibitor diffusivity was

analyzed in [34]. Spot-pinning behavior associated with two types of precursor gradients in the 2-D GM model was studied in [33] and [28]. In [1], spot alignment due to a spatially inhomogeneous auxin gradient was analyzed for a generalized Schnakenberg system modeling root hair profusion in plant cells. Reflection and transmission properties of pulses and spots across a step-function type barrier in a three-component Fitzhugh-Nagumo system has been studied in [38] and [18]. Pulse dynamics in a 1-D model with strongly localized spatial coefficients was studied recently in [5]. For front-type or transition-layer solutions, pinning effects due to either spatial inhomogeneities or jumps in the nonlinear kinetics were analyzed for various specific RD models in [6], [26], and [10] (see also the references therein).

The outline of this paper is as follows. In §2 we use the method of matched asymptotic expansions to construct N-spot quasi-equilibrium patterns for (1.2a) for both types of boundary conditions in (1.2b). For the Case I flux-type condition, we will also allow for $E = E(\mathbf{x}) > 0$. In our construction, which accounts for all logarithmic terms of order $\nu \equiv -1/\log\varepsilon$ in the expansion, we will focus primarily on aspects of the analysis that differ from that in [20] for N-spot quasi-equilibria on the surface of the sphere with a constant bulk feed. The problem of constructing quasi-equilibrium spot patterns is shown to reduce to the study of a nonlinear algebraic system that is defined in terms of the local spot profile, the Neumann Green's function for the Case I flux-type boundary condition or the Robin Green's function for the Case II Robin condition, and certain integrals that incorporate the spatial heterogeneities in the system. In §3 we use a higher order matching procedure to derive a DAE system characterizing slow spot dynamics over the long time scale $t = \mathcal{O}(\varepsilon^{-2})$ for either type of boundary conditions. In §5 we study the linear stability of N-spot quasi-equilibrium solutions to three distinct types of $\mathcal{O}(1)$ time-scale instabilities: peanut-splitting instabilities leading to spot self-replication, competition instabilities leading to spot annihilation, and spot amplitude oscillations arising from a Hopf bifurcation. These latter two types of instabilities are characterized by the spectra of a globally coupled eigenvalue problem (GCEP), defined in terms of certain eigenvalue-dependent Green's matrices.

Although our asymptotic results for the existence, linear stability, and slow dynamics, of spot patterns are derived for arbitrary 2-D domains, in the implementation of our theory in §4 we will focus exclusively on either a one-spot pattern or a ring pattern of spots, whereby $N \geq 2$ spots are equidistantly-placed on a circular ring that is concentric within the unit disk. For the unit disk, the Neumann Green's function and the Robin Green's function, and their regular parts, have explicit analytical formulae that can readily be used in our asymptotic analysis. This explicit formula for the Robin Green's function and its regular part is a new result. In addition, for ring patterns, and when E is radially symmetric, the study of the GCEP, characterizing competition or oscillatory instabilities, becomes significantly more tractable analytically. These simple one-spot and ring-type patterns in the unit disk are sufficiently rich for highlighting some of the key new phenomena associated with "open" RD systems with a spatially variable bulk feed. Our asymptotic results for the slow spot dynamics and the linear stability of quasi-equilibrium spots for these simple patterns are validated from full numerical simulations of the Brusselator model (1.2a) with (1.2b) using FlexPDE [7].

We now highlight a few specific results. In particular, consider (1.2a) with Case I boundary conditions (1.2b) with $A > 0$ and where $E > 0$ is a radially symmetric monotonically increasing function. In §4.1 we show that if a quasi-equilibrium ring pattern of $N \geq 2$ spots is linearly stable on an $\mathcal{O}(1)$ time-scale it will become pinned to a steady-state ring radius that is larger than that for the corresponding problem with $A = 0$ and a constant bulk feed (see Fig. 3 below). In this sense, the spots get pinned to spatial locations closer to where the fuel is larger. Moreover, when the bulk feed is sufficiently concentrated at the center of the disk, we show that a ring-pattern with $N \geq 2$ spots can undergo a finite-time collapse at the center of the disk where the "fuel" supply is largest. For a one-spot solution where $A > 0$ and E is radially symmetric, the spot always tends to the center of the disk with no monotonicity requirement on $E(|\mathbf{x}|)$. However, when E is not radially symmetric, but instead is highly concentrated near some point in the unit disk, a qualitatively new type of spot-pinning phenomenon can occur. We will show that, depending on the initial spot location, a spot can either tend to the point of concentration of the bulk feed as time increases (see Fig. 6 below), or else become pinned at some intermediate steady-state location, which is determined by a new saddle-node bifurcation structure of spot equilibria. The basin of attraction for initial spot locations corresponding to these two possible final states is determined numerically. For Case I boundary conditions, and with $E = E(|\mathbf{x}|)$, the analysis of peanut-splitting instabilities for ring patterns leads to an explicit threshold on A for the onset of self-replication behavior, which is independent of the ring radius. In addition, for $\tau \ll 1$ and $E = E(|\mathbf{x}|)$ in (1.2a), we show that ring patterns with $N \geq 2$ are linearly stable to peanut-splitting and competition instabilities whenever D satisfies $D_{\rm split} < D < D_{\rm comp}$, where $D_{\rm split} = \mathcal{O}(1)$ and $D_{\rm comp} = \mathcal{O}(\nu^{-1})$, with $\nu = -1/\log\varepsilon$, are two thresholds defined explicitly in terms of A, $\int_0^1 rE(r)\,dr$, N, and the Brusselator parameter f. These two thresholds are independent of the ring radius. Within this interval of D, our computations based on the GCEP shows that an oscillatory amplitude instability occurs whenever τ in (1.2a) exceeds a threshold.

One of the key new features for spot patterns of (1.2a) under the Case II Robin-type condition of (1.2b) is that a quasi-equilibrium ring pattern of spots can exhibit a saddle-node bifurcation structure in terms of either the inhibitor diffusivity D, the Robin constant κ_0, or the ambient external concentration v_b in (1.2a)-(1.2b). The location of these saddle-node points all depend on the ring radius r_0. A leading-order theory in ν to analytically reveal this saddle-node behavior is given in §5.2.1. With regards to spot dynamics, we show for a one-spot pattern that the steady-state spot location at the center of the unit disk becomes unstable as a solution to the DAE system for spot dynamics whenever the Robin constant exceeds a certain threshold. When this threshold is exceeded, the quasi-equilibrium spot slowly drifts to a new steady-state closer to the domain boundary. For the linear stability problem, in contrast to the situation with Case I flux-type boundary conditions, the peanut-splitting instability threshold for a quasi-equilibrium ring pattern under a Robin boundary condition now depends on the ring radius. As a result, spot self-replication behavior for a ring pattern of spots can be dynamically triggered by slow spot motion (see Fig. 13 below). Further linear stability results are given in §5.2. Finally, in §6 we list a few additional problems relating to open systems that warrant further study.

2 N-spot quasi-equilibria

In this section, we construct N-spot quasi-equilibrium solutions of (1.2) for Case I where we allow for both a boundary feed A and a spatially heterogeneous bulk feed $E(\mathbf{x})$. We will also analyze Case II, in which an inhomogeneous Robin boundary condition holds. However, for this case we will only consider a spatially uniform bulk feed E. The possibility of a non-zero boundary feed, a spatially inhomogeneous bulk feed, and a Robin boundary condition, all represent distinct types of heterogeneity in the Brusselator RD system. To asymptotically construct a quasi-equilibrium spot pattern in the presence of such heterogeneities, we must extend the hybrid asymptotic-numerical approach employed in [3, 13, 20, 22] for closed systems with spatially uniform reaction kinetics. In our analysis below for Cases I and II we will focus primarily on how to incorporate the various possible sources of heterogeneity into our asymptotic construction of N-spot quasi-equilibrium solutions. Overall, our analysis leads to a new hybrid asymptotic-numerical formulation of quasi-equilibrium spot patterns in the presence of heterogeneities in arbitrary 2-D domains.

2.1 Case I: Constant boundary feed and $E = E(\mathbf{x})$

We first construct an N-spot quasi-equilibrium solution for Case I of (1.2) where $E = E(\mathbf{x}) > 0$. We assume that the spot centers $\mathbf{x}_1, \ldots, \mathbf{x}_N$ within Ω are separated by an $\mathcal{O}(1)$ distance as $\varepsilon \to 0$. Then, in the inner $\mathcal{O}(\varepsilon)$ region near the j-th spot, we let $\mathbf{x} = \mathbf{x}_j + \varepsilon \mathbf{y}$, $u \sim \sqrt{D} u_j(\rho)$, and $v \sim v_j(\rho)/\sqrt{D}$ to obtain the radially symmetric core problem (cf. [20])

$$\begin{aligned} &\Delta_\rho u_j - u_j + f v_j u_j^2 = 0\,, \qquad \Delta_\rho v_j + u_j - v_j u_j^2 = 0\,, \qquad \rho \equiv |\mathbf{y}| > 0\,, \\ &u_j'(0) = v_j'(0) = 0\,; \qquad u_j \to 0\,, \qquad v_j \sim S_j \log\rho + \chi(S_j) \quad \text{as} \quad \rho \to \infty\,, \qquad j = 1, \ldots, N\,, \end{aligned} \tag{2.1a}$$

where $\chi(S_j)$ also depends on f and where $\Delta_\rho \equiv \partial_{\rho\rho} + \rho^{-1}\partial_\rho$. One key relationship needed for the construction of the outer solution is the readily-derived integral identity

$$S_j = \int_0^\infty (v_j u_j^2 - u_j)\rho\, d\rho = (1-f)\int_0^\infty v_j u_j^2 \rho\, d\rho\,. \tag{2.1b}$$

We refer to S_j as the spot strength for the j-th spot. The key quantity in the core problem is $\chi(S_j)$, which was computed numerically in [20] (see Fig. 3 therein) in the study of spot patterns on the sphere. For completeness, we reproduce it in Fig. 1 for a few values of f, along with typical spot profiles for various values of S_j.

In the outer region, we have from (1.2a) that $u = E(\mathbf{x})\varepsilon^2 + \mathcal{O}(\varepsilon^4)$ and $v \sim \mathcal{O}(1)$. Then, upon using the integral identity (2.1b), we have in the limit $\varepsilon \to 0$ that the $\varepsilon^{-2}(u - vu^2)$ term in (1.2a) can be written in terms of distributions as

$$\varepsilon^{-2}\left(u - vu^2\right) \to E(\mathbf{x}) + 2\pi\sqrt{D}\varepsilon^{-2}\sum_{j=1}^N \varepsilon^2 \left(\int_0^\infty (u_j - v_j u_j^2)\rho\, d\rho\right)\delta(\mathbf{x} - \mathbf{x}_j) = E(\mathbf{x}) - 2\pi\sqrt{D}\sum_{j=1}^N S_j \delta(\mathbf{x} - \mathbf{x}_j)\,. \tag{2.2}$$

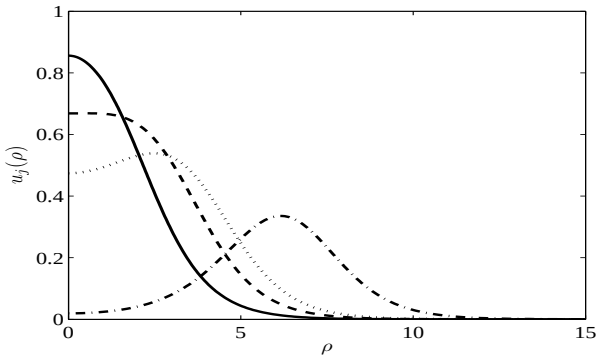

(a) spot profiles for $f = 0.4$

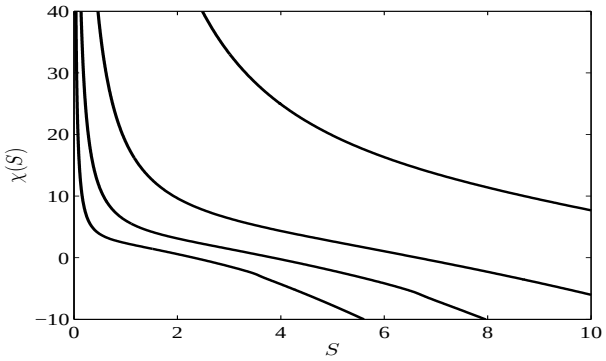

(b) $\chi(S)$ for various f

Figure 1: Left panel: typical spot profiles $u_j(\rho)$ with $f = 0.4$ and $S_j = 5.47$ (solid) $S_j = 9.1$ (dashed) $S_j = 10.92$ (dotted), $S_j = 13.34$ (dash-dotted). As S_j increases past $S_j \approx 9.1$, the spot develops a volcano profile. Right panel: $\chi(S; f)$ for $f = 0.2$, 0.4, 0.6 and 0.8. The higher (lower) curves correspond to smaller (larger) values of f. Notice that $\chi \to \infty$ as $S \to 0$ for any f in $0 < f < 1$.

In this limit, and upon matching to the far-field behavior of the inner core solution, the outer problem for v is

$$D\Delta v = -E(\mathbf{x}) + 2\pi\sqrt{D}\sum_{j=1}^{N} S_j\delta(\mathbf{x}-\mathbf{x}_j)\,, \quad \mathbf{x}\in\Omega\,; \qquad D\partial_n v = A\,, \quad \mathbf{x}\in\partial\Omega\,, \tag{2.3a}$$

$$v \sim D^{-1/2}\left(S_j \log|\mathbf{x}-\mathbf{x}_j| + S_j/\nu + \chi_j\right) \quad \text{as} \quad \mathbf{x}\to\mathbf{x}_j\,, \quad j = 1,\dots,N\,. \tag{2.3b}$$

In (2.3b), we have defined $\nu \equiv -1/\log\varepsilon \ll 1$ and $\chi(S_j) \equiv \chi_j$. The divergence theorem applied to (2.3a) provides a constraint on the spot strengths. This constraint is

$$\sum_{j=1}^{N} S_j = p_E\,; \qquad p_E \equiv \frac{A|\partial\Omega| + \int_\Omega E(\mathbf{x})\,d\mathbf{x}}{2\pi\sqrt{D}}\,, \tag{2.4}$$

where $|\Omega|$ is the area of Ω, and $|\partial\Omega|$ is its perimeter. Together with the singularity conditions (2.3b), (2.4) constitutes a system of $N+1$ nonlinear algebraic equations for the spot strengths S_j, $j = 1,\dots,N$, and for $\bar{v} = |\Omega|^{-1}\int_\Omega v\,d\mathbf{x}$.

The key new feature of the quasi-equilibrium analysis, distinct from that in [3, 13, 20, 22], concerns how to incorporate the boundary feed and bulk feed into the derivation of the nonlinear algebraic system for the spot strengths. To do so, we use superposition to conveniently decompose the solution to (2.3a) as

$$v = \frac{A}{D}v_{1p}(\mathbf{x}) + \frac{1}{D}v_2(\mathbf{x}) - 2\pi D^{-1/2}\sum_{i=1}^{N} S_i G(\mathbf{x};\mathbf{x}_i) + \bar{v}\,, \tag{2.5}$$

where $G(\mathbf{x};\mathbf{x}_0)$, with $\mathbf{x}_0\in\Omega$, is the unique Neumann Green's function satisfying

$$\begin{aligned} &\Delta G = \frac{1}{|\Omega|} - \delta(\mathbf{x}-\mathbf{x}_0)\,, \quad \mathbf{x}\in\Omega\,, \qquad \partial_n G = 0\,, \quad \mathbf{x}\in\partial\Omega\,; \\ &\int_\Omega G\,d\mathbf{x} = 0\,, \qquad G \sim -\frac{1}{2\pi}\log|\mathbf{x}-\mathbf{x}_0| + R(\mathbf{x}_0) + \mathcal{O}(1) \quad \text{as} \quad \mathbf{x}\to\mathbf{x}_0\,. \end{aligned} \tag{2.6}$$

Here $R(\mathbf{x}_0)$ is called the regular part of G at $\mathbf{x} = \mathbf{x}_0$. In our decomposition (2.5), the function $v_{1p}(\mathbf{x})$, which incorporates the boundary feed, is the unique solution to

$$\Delta v_{1p} = \frac{|\partial\Omega|}{|\Omega|}\,, \quad \mathbf{x}\in\Omega\,; \qquad \partial_n v_{1p} = 1\,, \quad \mathbf{x}\in\partial\Omega\,; \qquad \int_\Omega v_{1p}\,d\mathbf{x} = 0\,. \tag{2.7}$$

This solution is given explicitly in terms of G by the boundary integral

$$v_{1p}(\mathbf{x}) = \int_{\partial\Omega} G(\mathbf{x};\boldsymbol{\xi})\, d\boldsymbol{\xi}\,. \tag{2.8}$$

The second term $v_2(\mathbf{x})$ in (2.5), which allows for a spatially heterogeneous bulk feed, is the unique solution to

$$\Delta v_2 = \left(-E(\mathbf{x}) + \frac{1}{|\Omega|}\int_\Omega E(\mathbf{x})\, d\mathbf{x}\right), \quad \mathbf{x}\in\Omega\,, \qquad \partial_n v_2 = 0\,, \quad \mathbf{x}\in\partial\Omega\,, \qquad \int_\Omega v_2\, d\mathbf{x} = 0\,, \tag{2.9}$$

which is given explicitly by the bulk integral

$$v_2(\mathbf{x}) = \int_\Omega G(\mathbf{x};\boldsymbol{\xi})E(\boldsymbol{\xi})\, d\boldsymbol{\xi}\,. \tag{2.10}$$

We remark that when E is spatially uniform, i.e. $E(\mathbf{x}) = E_0$ with E_0 constant, we have $v_2 \equiv 0$ in Ω. With v_{1p}, v_2, and G, being uniquely defined in our decomposition (2.5), we need only determine $\bar{v}$ and the spot strengths $S_1,\ldots,S_N$. The divergence condition (2.4) provides one equation relating the spot strengths, while the remaining N equations are obtained by expanding v in (2.5) as $\mathbf{x}\to\mathbf{x}_j$ and enforcing the required singularity behavior in (2.3b). This yields that

$$S_j + 2\pi\nu\left(S_jR_j + \sum_{\substack{i=1\\ i\neq j}}^{N} S_iG_{ji}\right) + \nu\chi(S_j) = \nu D^{1/2}\left(\frac{A}{D}v_{1p}(\mathbf{x}_j) + \frac{v_2(\mathbf{x}_j)}{D} + \bar{v}\right), \qquad j = 1,\ldots,N\,, \tag{2.11}$$

where $R_j \equiv R(\mathbf{x}_j)$, $G_{ji}\equiv G(\mathbf{x}_j;\mathbf{x}_i)$, and the constraint (2.4) holds.

We can readily re-write the $(N+1)$-dimensional nonlinear algebraic system (2.4) and (2.11) in matrix form so as to isolate $\mathbf{s}\equiv(S_1,\ldots,S_N)^T$ and $\bar{v}$ separately. We readily calculate that

$$\begin{aligned} \mathbf{s} + 2\pi\nu\left(\mathcal{I}-\mathcal{E}\right)\mathcal{G}\mathbf{s} + \nu\left(\mathcal{I}-\mathcal{E}\right)\boldsymbol{\chi} &= \frac{p_E}{N}\,\mathbf{e} + \frac{\nu}{\sqrt{D}}\left[A\left(\mathcal{I}-\mathcal{E}\right)\mathbf{v}_{1p} + (\mathcal{I}-\mathcal{E})\mathbf{v}_2\right], \\ \bar{v} &= \frac{1}{N}\left[\frac{1}{\nu\sqrt{D}}\left(p_E + 2\pi\nu\mathbf{e}^T\mathcal{G}\mathbf{s} + \nu\mathbf{e}^T\boldsymbol{\chi}\right) - \frac{1}{D}\left(A\mathbf{e}^T\mathbf{v}_{1p} + \mathbf{e}^T\mathbf{v}_2\right)\right]. \end{aligned} \tag{2.12}$$

In (2.12), $(\cdot)^T$ denotes the transpose, $\mathcal{I}$ is the $N\times N$ identity matrix, while the rest of the quantities are defined as

$$\begin{gathered} \mathbf{s}\equiv\begin{pmatrix} S_1\\ \vdots\\ S_N\end{pmatrix}, \quad \mathbf{v}_{1p}\equiv\begin{pmatrix} v_{1p}(\mathbf{x}_1)\\ \vdots\\ v_{1p}(\mathbf{x}_N)\end{pmatrix}, \quad \mathbf{v}_2\equiv\begin{pmatrix} v_2(\mathbf{x}_1)\\ \vdots\\ v_2(\mathbf{x}_N)\end{pmatrix}, \quad \boldsymbol{\chi}\equiv\begin{pmatrix}\chi_1\\ \vdots\\ \chi_N\end{pmatrix}, \quad \mathbf{e}\equiv\begin{pmatrix}1\\ \vdots\\ 1\end{pmatrix}, \\ p_E\equiv\frac{A|\partial\Omega| + \int_\Omega E(\mathbf{x})\,d\mathbf{x}}{2\pi\sqrt{D}}, \quad \mathcal{E}\equiv\frac{1}{N}\mathbf{e}\mathbf{e}^T, \quad (\mathcal{G})_{ij}\equiv\begin{cases} R_j & i=j\\ G(\mathbf{x}_i;\mathbf{x}_j) & i\neq j\end{cases}, \quad i,j=1,\ldots,N\,. \end{gathered} \tag{2.13}$$

We summarize our asymptotic result characterizing N-spot quasi-equilibria for Case I in the following formal proposition:

Proposition 2.1 *For $\varepsilon\to 0$ the Brusselator model (1.2a) under Case I boundary conditions in (1.2b), allowing for a boundary feed and a spatially variable bulk feed $E = E(\mathbf{x})$, has an N-spot quasi-equilibrium solution u_e, v_e with spots centered at $\mathbf{x}_j$ for $j = 1,\ldots,N$, where u_e has the uniformly valid asymptotic representation*

$$u_e \sim \varepsilon^2 E(\mathbf{x}) + \sqrt{D}\sum_{j=1}^{N} u_j\left(\varepsilon^{-1}|\mathbf{x}-\mathbf{x}_j|\right). \tag{2.14}$$

Here $u_j(\rho)$ is the solution to the core problem (2.1). In the outer region, where $|\mathbf{x}-\mathbf{x}_j|\gg\mathcal{O}(\varepsilon)$ for $j=1,\ldots,N$, the quasi-equilibrium solution v_e for v is

$$v_e \sim \frac{A}{D}v_{1p}(\mathbf{x}) + \frac{1}{D}v_2(\mathbf{x}) - 2\pi D^{-1/2}\sum_{i=1}^{N} S_iG(\mathbf{x};\mathbf{x}_i) + \bar{v}\,, \tag{2.15}$$

while within an $\mathcal{O}(\epsilon)$ neighborhood of the j-th spot we have $v_e\sim v_j\left(\varepsilon^{-1}|\mathbf{x}-\mathbf{x}_j|\right)/\sqrt{D}$, where v_j satisfies the core problem (2.1). In (2.15), v_{1p} and v_2 are given in terms of the Neumann Green's function G of (2.6) by (2.8) and (2.10), respectively. The spot strengths S_j for $j=1,\ldots,N$ and $\bar{v}$ are determined from the nonlinear algebraic system (2.12).

The quasi-equilibrium solution construction in Proposition 2.1, which shows how to treat the two sources of heterogeneities of Case I of a non-zero boundary feed and a spatially variable bulk feed, extends the previous quasi-equilibrium analysis of [20] for a closed system with a spatially uniform bulk feed. In order to numerically compute quasi-equilibrium solutions for the heterogeneous case for a given spatial configuration $\mathbf{x}_1, \ldots, \mathbf{x}_N$ of spots, the key step is to numerically solve the nonlinear algebraic system (2.12) for the spot strengths. This involves the Neumann Green's function G of (2.6), the boundary integral of (2.8), and the bulk integral of (2.10) determined in terms of $E(\mathbf{x})$ and G. The nonlinear system (2.12) also involves the numerically computed function $\chi(S)$, as determined from the core problem (2.1). Overall this provides a hybrid asymptotic-numerical characterization of quasi-equilibria in the presence of heterogeneities, in which asymptotic analysis was used to derive (2.12), but numerical methods are required to compute its solutions.

To illustrate the new solution behavior associated with a nonzero boundary flux and a spatially non-uniform $E(\mathbf{x})$, for analytical tractability we will only consider the special case where Ω is the unit disk, for which the Neumann Green's function is known analytically [12], and for which v_{1p} is the radially symmetric function

$$v_{1p} = \frac{r^2}{2} - \frac{1}{4}\,, \qquad r \equiv |\mathbf{x}|\,. \tag{2.16}$$

In the unit disk, in §4 we will consider either a one-spot pattern or a "ring-pattern" of $N > 1$ spots, whereby the spot locations are equally-spaced on a circular ring of radius r_0, with $0 < r_0 < 1$, that is concentric within the unit disk.

We now show from (2.12) that such a quasi-equilibrium ring pattern of spots exists when E is radially symmetric, i.e. when $E = E(r)$ with $r = |\mathbf{x}|$. To establish this we first observe that for a ring-pattern the Neumann Green's matrix $\mathcal{G}$ is a cyclic symmetric matrix, so that $\mathcal{G}\mathbf{e} = \kappa_1\mathbf{e}$, where $\mathbf{e} = (1, \ldots, 1)^T$. Moreover, we observe that $\mathbf{v}_{1p} = v_{1p}(r_0)\mathbf{e}$, and $\mathbf{v}_2 = v_2(r_0)\mathbf{e}$ when $E = E(r)$. Then, since $(\mathcal{I} - \mathcal{E})\mathbf{e} = \mathbf{0}$, (2.12) yields the common spot strength solution $\mathbf{s} = S_c\mathbf{e}$, where

$$S_c = \frac{1}{N\sqrt{D}}\left[A + \int_0^1 rE(r)\,dr\right]\,. \tag{2.17}$$

We will show below in §5 that as the common spot strength S_c of a ring pattern increases past a certain threshold Σ_2, which depends on the Brusselator parameter f, a simultaneous peanut-splitting instability for the spots on the ring is initiated. From full numerical simulations of the Brusselator PDE system this linear instability is shown to lead to nonlinear spot self-replication events. A key observation from (2.17) is that this spot replication behavior can be triggered either through increases in the boundary flux A or from increasing the spatial average of the bulk feed $E(r)$.

2.2 Case II: Robin boundary condition with constant E

Next, we construct an N-spot quasi-equilibrium solution for Case II of (1.2) where v_b is a prescribed constant. We will assume a spatially uniform bulk feed rate, and set $E = 1$ without loss of generality. The analysis follows that of Case I, except that we set $E = 1$ and replace the Neumann problem of (2.3) with the Robin problem. In this way, we get

$$D\Delta v = -1 + 2\pi\sqrt{D}\sum_{j=1}^{N} S_j\delta(\mathbf{x} - \mathbf{x}_j)\,, \quad \mathbf{x} \in \Omega\,; \qquad \partial_n v + \kappa_0(v - v_b) = 0\,, \quad \mathbf{x} \in \partial\Omega\,, \tag{2.18}$$

with the same singularity conditions as given in (2.3b). To solve (2.18) when $\kappa_0 > 0$ we introduce the unique Robin Green's function $G_\kappa(\mathbf{x}; \mathbf{x}_0)$, satisfying

$$\begin{aligned} &\Delta G_\kappa = -\delta(\mathbf{x} - \mathbf{x}_0)\,, \quad \mathbf{x} \in \Omega\,, \qquad \partial_n G_\kappa + \kappa_0 G_\kappa = 0\,, \quad \mathbf{x} \in \partial\Omega\,; \\ &G_\kappa \sim -\frac{1}{2\pi}\log|\mathbf{x} - \mathbf{x}_0| + R_\kappa(\mathbf{x}_0) + \mathcal{O}(1) \quad \text{as} \quad \mathbf{x} \to \mathbf{x}_0\,. \end{aligned} \tag{2.19}$$

In terms of this Robin Green's function, the solution to (2.18) is

$$v = \frac{1}{D}v_3(\mathbf{x}) + v_b - \frac{2\pi}{\sqrt{D}}\sum_{j=1}^{N} S_j G_\kappa(\mathbf{x}; \mathbf{x}_j)\,, \tag{2.20}$$

where v_3 is the unique solution to

$$\Delta v_3 = -1\,, \quad \mathbf{x} \in \Omega\,; \qquad \partial_n v_3 + \kappa_0 v_3 = 0\,, \quad \mathbf{x} \in \partial\Omega\,, \tag{2.21}$$

which is given in terms of G_κ by

$$v_3(\mathbf{x}) = \int_\Omega G_\kappa(\mathbf{x};\boldsymbol{\xi})\, d\boldsymbol{\xi}\,. \tag{2.22}$$

By imposing the matching condition (2.3b), we then obtain the following nonlinear algebraic system for S_j, $j = 1,\dots,N$:

$$\mathbf{s} + 2\pi\nu\mathcal{G}_\kappa\mathbf{s} + \nu\boldsymbol{\chi} = \sqrt{D}\nu\left(\frac{1}{D}\mathbf{v}_3 + v_b\mathbf{e}\right)\,, \tag{2.23a}$$

where $\mathbf{v}_3$, and the symmetric $N\times N$ Robin Green's matrix $\mathcal{G}_\kappa$, are defined by

$$\mathbf{v}_3 \equiv (v_3(\mathbf{x}_1),\dots,v_3(\mathbf{x}_N))^T\,, \qquad (\mathcal{G}_\kappa)_{ij} \equiv \begin{cases} R_{\kappa j} & i = j \\ G_\kappa(\mathbf{x}_i;\mathbf{x}_j) & i\neq j \end{cases}\,, \quad i,j = 1,\dots,N\,. \tag{2.23b}$$

We summarize this formal construction of quasi-equilibrium spot patterns for Case II as follows:

Proposition 2.2 *For $\varepsilon\to 0$ the Brusselator model (1.2a) under Case II boundary conditions in (1.2b), and with constant bulk feed $E\equiv 1$, has an N-spot quasi-equilibrium solution u_e, v_e with spots centered at $\mathbf{x}_j$ for $j = 1,\dots,N$, where u_e is given in (2.14) with $E\equiv 1$. In the outer region, the quasi-equilibrium solution v_e for v is*

$$v_e \sim \frac{1}{D}v_3(\mathbf{x}) + v_b - \frac{2\pi}{\sqrt{D}}\sum_{j=1}^N S_j G_\kappa(\mathbf{x};\mathbf{x}_j)\,, \tag{2.24}$$

while in the inner region near the j-th spot we have $v_e \sim v_j\left(\varepsilon^{-1}|\mathbf{x}-\mathbf{x}_j|\right)/\sqrt{D}$. Here v_j satisfies the core problem (2.1), G_κ is the Robin Green's function of (2.19), and v_3 is given in terms of G_κ by (2.22). The spot strengths S_j for $j = 1,\dots,N$ satisfy the nonlinear algebraic system (2.23).

Although this new hybrid asymptotic-numerical formulation of quasi-equilibrium spot patterns under an inhomogeneous Robin boundary condition applies to an arbitrary 2-D domain, in order to readily exhibit the qualitatively new phenomena associated with the Robin condition, we will proceed as in Case I by considering only the case where Ω is the unit disk. When Ω is the unit disk, the explicit solution to (2.21) is

$$v_3(r) = \frac{(1-r^2)}{4} + \frac{1}{2\kappa_0}\,, \qquad r = |\mathbf{x}|\,. \tag{2.25}$$

In addition, for the unit disk, the Robin Green's function can be obtained analytically by decomposing it as $G_\kappa = (2\pi)^{-1}(-\log|\mathbf{x}-\mathbf{x}_0| + H(\mathbf{x}))$ and solving for $H(\mathbf{x})$ via a Fourier series. In terms of the complex variables $z = re^{i\theta}$ and $\zeta = r_0 e^{i\theta_0}$, where we specify the polar coordinates $\mathbf{x}\to(r,\theta)$ and $\mathbf{x}_0\to(r_0,\theta_0)$, we readily calculate that

$$G_\kappa(\mathbf{x};\mathbf{x}_0) = \frac{1}{2\pi}\left[\frac{1}{\kappa_0} - \log|z-\zeta| - \log|z\bar{\zeta}-1| - 2\kappa_0\sum_{n=1}^\infty \frac{(rr_0)^n}{n(n+\kappa_0)}\cos(n(\theta-\theta_0))\right]\,. \tag{2.26a}$$

In (2.26a), $\bar{\cdot}$ denotes the complex conjugate. From (2.19), the regular part of G_κ as $\mathbf{x}\to\mathbf{x}_0$ is then given by

$$R_\kappa(\mathbf{x}_0) = \frac{1}{2\pi}\left[\frac{1}{\kappa_0} - \log(1-r_0^2) - 2\kappa_0\sum_{n=1}^\infty \frac{r_0^{2n}}{n(n+\kappa_0)}\right]\,, \qquad r_0 = |\mathbf{x}_0|\,. \tag{2.26b}$$

When $\kappa_0 = 1$, the series in (2.26b) can be summed explicitly. To see this, we decompose the summand of (2.26b) in terms of its partial fraction expansion as $\sum_{n=1}^\infty \rho^n/[n(n+1)] = 1 + (1-\rho^{-1})\sum_{n=1}^\infty \rho^n/n$, where $\rho\equiv r_0^2 < 1$. Then, by recalling the Taylor series representation of $-\log(1-\rho)$ for $\rho<1$, we calculate from (2.26b) that for $\kappa_0 = 1$

$$R_1(\mathbf{x}_0) = -\frac{1}{2\pi}\left[1 + \left(\frac{2}{r_0^2} - 1\right)\log(1-r_0^2)\right]\,, \qquad \text{where} \qquad r_0 = |\mathbf{x}_0|\,. \tag{2.27}$$

For a ring pattern, where N spots are spaced equally on a ring of radius $r_0 < 1$ concentric within the unit disk, the Robin Green's matrix $\mathcal{G}_\kappa$ in (2.23) is cyclic, and so has a constant row sum. As a result, we obtain that

$$\mathcal{G}_\kappa\mathbf{e} = \sigma_{\kappa,1}\mathbf{e}\,, \qquad \sigma_{\kappa,1} = R_\kappa(\mathbf{x}_1) + \sum_{j\neq 1}^N G_\kappa(\mathbf{x}_1;\mathbf{x}_j)\,, \tag{2.28}$$

where $\sigma_{\kappa,1} = \sigma_{\kappa,1}(r_0)$. For such a ring pattern, we look for a solution to (2.23) of the form $\mathbf{s} = S_c\mathbf{e}$. In this way, we obtain that the common spot strength S_c satisfies the scalar nonlinear algebraic equation

$$S_c + 2\pi\nu\sigma_{\kappa,1}S_c + \nu\chi(S_c) = \nu\sqrt{D}\left[\frac{1}{D}v_3(r_0) + v_b\right], \qquad \text{where} \qquad v_3(r) = \frac{(1-r^2)}{4} + \frac{1}{2\kappa_0}. \tag{2.29}$$

We will show below in §5.2.1 (see also Fig. 7(a) below) that the solution to (2.29) has a novel saddle-node bifurcation structure, which can be expressed in terms of either D or $\kappa_0 > 0$. Therefore, the existence problem for quasi-equilibrium ring patterns under a Robin condition is markedly different than under a homogeneous Neumann boundary condition where no such saddle-node structure occurs (as seen by setting $A = 0$ and $E = 1$ in (2.17)). From (2.29) we further observe, in contrast to (2.17) for Case I, that when a solution S_c exists, it will now depend on the radius r_0 of the ring on which the spots lie. We will show below in §4 in our study of slow spot dynamics that this leads to a coupled differential algebraic system of equations (DAE) for the slow evolution of the ring radius r_0 and for S_c.

3 Slow dynamics of spots: Derivation of DAE system

In this section, we analyze the slow dynamics of the N-spot quasi-equilibria of §2, under the assumption that the quasi-equilibrium solution is linearly stable on $\mathcal{O}(1)$ time-scales. This stability problem is analyzed below in §5. We will analyze slow dynamics for both Case I, where $E = E(\mathbf{x})$ is spatially non-homogeneous, and Case II under the Robin condition and a constant bulk feed. To do so, we use a higher order asymptotic matching of the inner and outer solutions and obtain that the spot locations in (2.14) depend on slow time as $x_j = x_j(\varepsilon^2 t)$. We then invoke a solvability condition in the inner region to obtain an ODE for $x_j(\varepsilon^2 t)$. Together with the nonlinear algebraic systems derived in §2 for the spot strengths S_j, for $j = 1, \ldots, N$, we derive a system of differential algebraic equations (DAEs) for the spot locations $x_j(\varepsilon^2 t)$ coupled to the S_j. Since the analysis is similar to that of [3, 13, 25] for closed systems in two and three spatial dimensions, we will give only an abbreviated analysis here. For further details, see [3, 13, 25].

We first consider Case I with a boundary feed and a spatially inhomogeneous bulk feed $E = E(\mathbf{x})$.

In the inner region near the j-th spot, we let $\mathbf{y} = \varepsilon^{-1}(\mathbf{x} - \mathbf{x}_j(\sigma))$ with $\sigma = \varepsilon^2 t$ representing slow time. We also expand

$$u \sim D^{1/2}(u_j(\rho) + \varepsilon u_{j1}(\mathbf{y}) + \cdots), \qquad v \sim D^{-1/2}(v_j(\rho) + \varepsilon v_{j1}(\mathbf{y}) + \cdots),$$

where u_j and v_j are the radially symmetric solutions satisfying the core problem (2.1). Substituting this expansion into (2.1), and collecting terms at $\mathcal{O}(\varepsilon)$, we obtain the inhomogeneous system

$$\Delta_{\mathbf{y}}\mathbf{w}_1 + \mathcal{M}_j\mathbf{w}_1 = -\mathbf{f}_j, \qquad \mathbf{y} \in \mathbb{R}^2, \tag{3.1a}$$

where $\Delta_{\mathbf{y}}$ is the Laplacian with respect to the inner variable $\mathbf{y} = (y_1, y_2)^T = (\rho\cos\phi, \rho\sin\phi)^T$, while

$$\mathbf{w}_1 = \begin{pmatrix} u_{j1} \\ v_{j1} \end{pmatrix}, \quad \mathcal{M}_j = \begin{pmatrix} -1 + 2fu_jv_j & fu_j^2 \\ 1 - 2u_jv_j & -u_j^2 \end{pmatrix}, \qquad \mathbf{f}_j = \begin{pmatrix} u_j'\mathbf{e}_\phi \cdot \mathbf{x}_j' \\ 0 \end{pmatrix}, \qquad \mathbf{e}_\phi = \begin{pmatrix} \cos\phi \\ \sin\phi \end{pmatrix}. \tag{3.1b}$$

To determine the far-field condition for $\mathbf{w}_1$, the matching condition (2.3b) must be expanded to higher order. The leading order matching leads to (2.12), while at the next order, we have

$$\varepsilon D^{-1/2}v_{j1} \sim \left(\frac{A\nabla_{\mathbf{x}}v_{1p}(\mathbf{x}_j) + \nabla_{\mathbf{x}}v_2(\mathbf{x}_j)}{D} - 2\pi D^{-1/2}\sum_{i\neq j}^{N} S_i\nabla_{\mathbf{x}}G_{ji} - 2\pi D^{-1/2}S_j\nabla_{\mathbf{x}}R_j\right)\cdot(\mathbf{x} - \mathbf{x}_j) \quad \text{as} \quad \mathbf{x} \to \mathbf{x}_j. \tag{3.2}$$

In (3.2), $\nabla_{\mathbf{x}}f(\mathbf{x}_j)$ and $\nabla_{\mathbf{x}}f_j$ both denote the gradient of $f(\mathbf{x})$ evaluated at $\mathbf{x} = \mathbf{x}_j$. Defining

$$\mathbf{B}_j \equiv D^{-1/2}\left[A\nabla_{\mathbf{x}}v_{1p}(\mathbf{x}_j) + \nabla_{\mathbf{x}}v_2(\mathbf{x}_j)\right] - 2\pi\left(S_j\nabla_{\mathbf{x}}R_j + \sum_{i\neq j}^{N} S_i\nabla_{\mathbf{x}}G_{ji}\right), \tag{3.3}$$

we obtain the required far-field behavior for (3.1)

$$\mathbf{w}_1 \sim \begin{pmatrix} 0 \\ \rho \mathbf{B}_j \cdot \mathbf{e}_\phi \end{pmatrix} \quad \text{as} \quad \rho \to \infty \,. \tag{3.4}$$

Since the homogeneous problem $\Delta_{\mathbf{y}} \mathbf{\Phi} + \mathcal{M}_j \mathbf{\Phi} = 0$ with $\Phi \to \mathbf{0}$ as $\rho \to \infty$ has two non-trivial solutions, as observed from differentiating the core problem (2.1) with respect to y_1 and y_2, the corresponding adjoint problem

$$\Delta_{\mathbf{y}} \mathbf{\Psi} + \mathcal{M}_j^T \mathbf{\Psi} = \mathbf{0} \,, \qquad \mathbf{\Psi} \to \mathbf{0} \quad \text{as} \quad \rho \to \infty \,, \tag{3.5}$$

must have a nullspace of dimension at least two. We will assume that this nullspace is exactly two-dimensional. The right-hand side of (3.1a) along with the far-field condition (3.4) must therefore satisfy two solvability conditions corresponding to the two homogeneous solutions of (3.5), which we write as

$$\mathbf{\Psi}_c = \mathbf{P}(\rho) \cos\phi \,, \qquad \mathbf{\Psi}_s = \mathbf{P}(\rho) \sin\phi \,, \tag{3.6}$$

where $\mathbf{P}(\rho) = (P_1(\rho), P_2(\rho))^T$ is the unique solution of

$$\Delta_\rho \mathbf{P} - \frac{1}{\rho^2} \mathbf{P} + \mathcal{M}_j^T \mathbf{P} = 0 \,, \quad \rho > 0 \,; \qquad \mathbf{P} \sim \begin{pmatrix} 1/\rho \\ 1/\rho \end{pmatrix} \quad \text{as} \quad \rho \to \infty \,. \tag{3.7}$$

In (3.7), we set the far-field condition for P_2 as a normalization condition, while that for P_1 follows from the condition $P_1 \sim P_2$ for $\rho \to \infty$, as dictated by the limiting form of $\mathcal{M}_j^T$ as $\rho \to \infty$.

Invoking the solvability condition by multiplying (3.1) by $\mathbf{\Psi}_c^T$ and $\mathbf{\Psi}_s^T$ and applying Green's identity on a circle of radius $\rho_0 \gg 1$, while imposing the far-field conditions (3.4) and (3.7), we obtain an ODE for $x_j(\sigma)$, $j = 1, \ldots, N$, characterizing the slow spot dynamics. The result is summarized formally as follows:

Proposition 3.1 *Assuming that the quasi-equilibrium solution of Proposition 2.1 corresponding to Case I is stable on $\mathcal{O}(1)$ time-scales, the slow dynamics of a collection of spots on the time-scale $\sigma = \varepsilon^2 t$ is characterized by*

$$\frac{d\mathbf{x}_j}{d\sigma} = \gamma_j \left[\mathbf{F}_{jp} + \mathbf{F}_{jh} \right] \,, \tag{3.8a}$$

where

$$\mathbf{F}_{jp} = D^{-1/2} \left(A \nabla_{\mathbf{x}} v_{1p}(\mathbf{x}_j) + \nabla_{\mathbf{x}} v_2(\mathbf{x}_j) \right) \,, \qquad \mathbf{F}_{jh} = -2\pi \left(S_j \nabla_{\mathbf{x}} R_j + \sum_{i \neq j}^{N} S_i \nabla_{\mathbf{x}} G_{ji} \right) \,. \tag{3.8b}$$

Here S_j for $j = 1, \ldots, N$ satisfy the nonlinear system (2.12), while v_{1p} and v_2 are given in terms of the Neumann Green's function G of (2.6) by (2.8) and (2.10). In (3.8a), $\gamma_j = \gamma_j(S_j)$ is defined in terms of $u_j'(\rho)$ and the adjoint solution $P_1(\rho)$ by

$$\gamma_j = -\frac{2}{\int_0^\infty P_1 u_j' \rho \, d\rho} \,. \tag{3.8c}$$

In (3.8a), the new term $\mathbf{F}_{jp}$ in the slow spot dynamics acts as a "pinning potential", while $\mathbf{F}_{jh}$ involves the Green's function and its regular part and has the same form as in earlier studies of spot dynamics [3, 13]. This new term $\mathbf{F}_{jp}$, which arises due to the heterogeneity induced by the boundary feed and non-uniform bulk feed, acts to "pin" spots away from their usual steady-state locations determined by the zeroes of $\mathbf{F}_{jh}$ in an otherwise identical closed system with spatially homogeneous feed. In §4.1 we will use (3.8) to illustrate new types of spot-pinning behavior in the unit disk.

In Fig. 2 we plot the numerically computed function $\gamma_j(S)$, as determined from the adjoint problem (3.7) for a few values of f. These computations show that $\gamma_j > 0$ on the range $S_j < \Sigma_2(f)$ for which there are no peanut-splitting instabilities of the spot profile. This threshold $\Sigma_2(f)$ for peanut-splitting is obtained in §5.1.

Next, we consider Case II with the inhomogeneous Robin boundary condition of (1.2b) and with $E \equiv 1$. In this case, the outer solution for v is given by (2.20) where $v_3(\mathbf{x})$ and $G_\kappa(\mathbf{x}; \mathbf{x}_0)$ satisfy (2.21) and (2.19), respectively. The local behavior of v as $\mathbf{x} \to \mathbf{x}_j$ determines the far-field behavior of v_{j1} in (3.2), so that in place of (3.3) we have

$$\mathbf{B}_j \equiv D^{-1/2} \nabla_{\mathbf{x}} v_3(\mathbf{x}_j) - 2\pi \left[S_j \nabla_{\mathbf{x}} R_{\kappa j} + \sum_{i \neq j}^{N} S_i \nabla_{\mathbf{x}} G_{\kappa j i} \right] \,. \tag{3.9}$$

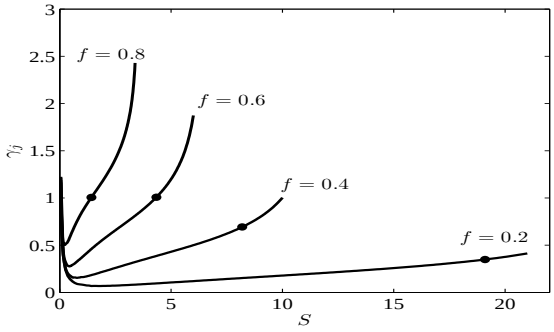

Figure 2: Plot of $\gamma_j(S)$ versus S for a few values of f, as computed numerically from the adjoint problem (3.7) and (3.8c). The peanut-splitting instability threshold value of S, labeled by $\Sigma_2(f)$ and analyzed in §5.1, is indicated by the bullet points. For $S < \Sigma_2(f)$, the spot pattern is linearly stable to peanut-splitting instabilities.

By the same procedure leading to (3.8), we obtain the following DAE system characterizing the slow dynamics of the spot locations $\mathbf{x}_j$ and spot strengths S_j, for $j = 1, \ldots, N$:

Proposition 3.2 *Assuming that the quasi-equilibrium solution of Proposition 2.2 corresponding to Case II is stable on $\mathcal{O}(1)$ time-scales, the slow dynamics of a collection of spots on the time-scale $\sigma = \varepsilon^2 t$ is characterized by the DAE system consisting of the dynamics*

$$\frac{d\mathbf{x}_j}{d\sigma} = \gamma_j \left[D^{-1/2} \nabla_{\mathbf{x}} v_3(\mathbf{x}_j) - 2\pi \left(S_j \nabla_{\mathbf{x}} R_{\kappa j} + \sum_{i \neq j}^{N} S_i \nabla_{\mathbf{x}} G_{\kappa j i} \right) \right] , \tag{3.10}$$

coupled to the nonlinear algebraic system (2.23) for the spot strengths S_j, for $j = 1, \ldots, N$. Here $v_3(\mathbf{x})$ is given in terms of the Robin Green's function G_κ of (2.19) by (2.22), while γ_j is defined in (3.8c).

4 Ring patterns and one-spot dynamics in the unit disk

We now use our results in §2 and §3 for quasi-equilibria and slow spot dynamics for Case I and II to exhibit new spot-pinning and bifurcation behavior for both a one-spot solution and for a ring pattern of spots in the unit disk.

4.1 Case I: Dynamics and quasi-equilibria

We first consider a ring pattern of N spots concentric within the unit disk for the case where the bulk feed is radially symmetric, i.e. $E(\mathbf{x}) = E(r)$ with $r = |\mathbf{x}|$. We use Propositions 2.1 and 3.1 to derive an explicit ODE for the slow dynamics of the ring radius r_0 under the assumption that the ring profile is linearly stable on $\mathcal{O}(1)$ time-scales. To analyze such a ring pattern, we recall from [13] that

$$\nabla_{\mathbf{x}} R_j + \sum_{k \neq j}^{N} \nabla_{\mathbf{x}} G_{jk} = \frac{p'(r_0)}{2N} \mathbf{e}_{\theta_j} , \qquad \text{where} \qquad \mathbf{e}_{\theta_j} \equiv (\cos(\theta_j), \sin(\theta_j))^T , \qquad \theta_j \equiv \frac{2\pi j}{N} , \quad j = 1, \ldots, N , \tag{4.1}$$

where $\mathbf{x}_j = r_0 \mathbf{e}_{\theta_j}$ for $j = 1, \ldots, N$, are the spot locations. In (4.1), $p(r_0)$ is proportional to the eigenvalue associated with the eigenvector $\mathbf{e}$ of the Neumann Green's matrix $\mathcal{G}$, which necessarily has a cyclic matrix structure for a ring pattern. Since the Neumann Green's function is known analytically for the unit disk, $p(r_0)$ can be calculated explicitly for a ring pattern. From Eq. (4.11) of [12] we have that

$$\mathcal{G}\mathbf{e} = \frac{p(r_0)}{N} \mathbf{e} , \qquad \text{where} \qquad p(r_0) \equiv \mathbf{e}^T \mathcal{G} \mathbf{e} = \frac{1}{2\pi} \left[-N \log(N r_0^{N-1}) - N \log(1 - r_0^{2N}) + r_0^2 N^2 - \frac{3N^2}{4} \right] , \tag{4.2}$$

so that (4.1) becomes

$$\nabla_{\mathbf{x}} R_j + \sum_{k\neq j}^{N} \nabla_{\mathbf{x}} G_{j,k} = \frac{1}{2\pi}\left[-\frac{(N-1)}{2r_0} + \frac{N r_0^{2N-1}}{1-r_0^{2N}} + r_0 N \right] \mathbf{e}_{\theta_j} \,. \tag{4.3}$$

Finally, with $\mathbf{x}_j = r_0(\sigma)\mathbf{e}_{\theta_j}$, v_{1p} given by (2.16), and $v_2 = v_2(r_0)$ satisfying (2.9) with $E = E(r)$, we use (3.8) of Proposition 3.1 together with (4.3) to obtain an ODE for the ring radius

$$\frac{dr_0}{d\sigma} = \gamma(S_c)\left[D^{-1/2}\left(A r_0 + v_2'(r_0) \right) + S_c\left(\frac{(N-1)}{2r_0} - \frac{N r_0^{2N-1}}{1-r_0^{2N}} - r_0 N \right) \right] , \qquad \text{where} \qquad \sigma = \varepsilon^2 t \,. \tag{4.4}$$

In (4.4), the common spot strength S_c is given by (2.17). For an arbitrary radially symmetric bulk feed $E(r) > 0$, we can solve (2.9) for v_2' and then substitute into (4.4). This yields the following result:

Proposition 4.1 *For $\varepsilon \to 0$ and for Case I of (1.2b), consider a ring-pattern of $N \geq 2$ spots on a ring of radius r_0 concentric within the unit disk and where the bulk feed is radially symmetric so that $E = E(r)$. Assuming that the ring-pattern is stable on $\mathcal{O}(1)$ time-scales, the slow dynamics of the ring radius r_0 satisfies the ODE*

$$\frac{dr_0}{d\sigma} = \frac{\gamma(S_c)}{\sqrt{D}}\left[H_1(r_0) + H_0(r_0) \right] , \tag{4.5a}$$

where

$$H_1(r_0) \equiv A r_0 + \frac{\bar{E}}{r_0}\int_0^{r_0} \eta\left(1 - \frac{E(\eta)}{\bar{E}} \right) d\eta \,, \qquad H_0(r_0) \equiv \frac{S_{c0}}{N}\left(\frac{(N-1)}{2r_0} - \frac{N r_0^{2N-1}}{1-r_0^{2N}} - r_0 N \right) . \tag{4.5b}$$

Here S_{c0} and $\bar{E}$ are defined by

$$S_{c0} \equiv S_c N D^{1/2} \equiv A + \bar{E}/2 \,, \qquad \bar{E} \equiv 2\int_0^1 \eta E(\eta)\, d\eta \,. \tag{4.5c}$$

For $N \geq 2$, and when there is no boundary feed ($A = 0$) and a spatially constant bulk feed $E(r) \equiv E_0$, with E_0 a positive constant, we claim that the ODE (4.5a) has a unique stable steady-state solution r_{0E}^0 on $0 < r_{0E}^0 < 1$. Since $H_1 \equiv 0$ when $A = 0$ and $E(r) = E_0$, along with the fact that $\gamma(S_c) > 0$ for $S_c < \Sigma_2(f)$, we need only prove that $H_0(r_0)$ has a unique root r_{0E}^0 on $0 < r_{0E}^0 < 1$, with $H_0'(r_{0E}^0) < 0$. This follows readily from from the facts that

$$\lim_{r_0\to 0+} H_0(r) = +\infty \,, \quad \lim_{r_0\to 1-} H_0(r) = -\infty \,, \quad H_0'(r_0) = -\frac{S_{c0}}{N}\left[\frac{(N-1)}{2r_0^2} + \frac{N}{(1-r_0^{2N})^2}\left(2N - 1 + r_0^{2N} \right) r_0^{2N-2} + N \right] < 0 \,. \tag{4.6}$$

Next, for $N \geq 2$, we show for an open system with $A > 0$ and with a smooth monotone non-decreasing bulk feed that there is a unique and stable steady-state ring radius r_{0E} in $0 < r_{0E} < 1$, for which $r_{0E} > r_{0E}^0$. The result is as follows:

Proposition 4.2 *For a ring pattern of $N \geq 2$ spots for Case I, as characterized by Proposition 4.1, with a boundary feed $A > 0$ and a smooth monotone non-decreasing bulk feed $E(r) > 0$ with $E'(r) \geq 0$, the ODE (4.5a) has a unique and stable steady-state ring radius r_{0E} in $0 < r_{0E} < 1$. Moreover, $r_{0E} > r_{0E}^0$, where r_{0E}^0 is the unique and stable ring radius for the closed system with a spatially uniform bulk feed.*

Proof: We establish this result in several steps. We first show that (4.5a) has a unique root when $A > 0$, $E(r) > 0$ and $E'(r) > 0$. We observe that

$$\lim_{r_0\to 0+}\left(H_0(r) + H_1(r) \right) = +\infty \,, \quad \lim_{r_0\to 1-}\left(H_0(r) + H_1(r) \right) = -\infty \,, \tag{4.7}$$

and we use (4.5c) for S_{c0} to calculate

$$H_0(r_0) + H_1(r_0) = -\frac{1}{r_0}\int_0^{r_0} \eta E(\eta)\, d\eta + \frac{S_{c0}}{N}\left[\frac{(N-1)}{2r_0} - \frac{N r_0^{2N-1}}{1-r_0^{2N}} \right] .$$

By calculating the derivative of this expression, and then using integration by parts, we obtain that

$$H_0'(r_0)+H_1'(r_0)=-\frac{E(r_0)}{2}-\frac{1}{2r_0^2}\int_0^{r_0}\eta^2E'(\eta)\,d\eta-\frac{S_{c0}}{N}\left[\frac{(N-1)}{2r_0^2}+\frac{N}{(1-r_0^{2N})^2}\left(2N-1+r_0^{2N}\right)r_0^{2N-2}\right].$$

Since $E(r)>0$ and $E'(r)>0$ it follows that $H_0(r_0)+H_1(r_0)$ is monotone decreasing. In view of (4.7), we conclude that there is a unique steady-state ring radius r_{0E} in $0<r_{0E}<1$ for the slow dynamics (4.5a).

The second step is to show that $r_{0E}>r_{0E}^0$. Since $H_0(r_{0E}^0)=0$, and H_0+H_1 is monotone decreasing with $H_0+H_1\to-\infty$ as $r_0\to1^-$, we need only show that $H_1(r_{0E}^0)>0$. From (4.5b) we have for any r_0 that

$$H_1(r_0)\equiv Ar_0+\frac{\bar{E}}{r_0}\mathcal{H}_1(r_0)\,,\qquad \mathcal{H}_1(r_0)\equiv\int_0^{r_0}\eta\left(1-\frac{E(\eta)}{\bar{E}}\right)d\eta\,,\qquad \bar{E}\equiv2\int_0^1\eta E(\eta)\,d\eta\,.$$

To prove $H_1(r_{0E}^0)>0$, it suffices to prove that $\mathcal{H}_1(r_0)>0$ on $0<r_0<1$. To do so, we first observe that $\mathcal{H}_1(0)=\mathcal{H}_1(1)=0$. Then, since $E(0)<\bar{E}<E(1)$, we obtain that $\mathcal{H}_1$ is positive near the endpoints, with local behavior

$$\mathcal{H}_1(r_0)\sim\frac{r_0^2}{2}\left(1-\frac{E(0)}{\bar{E}}\right)>0\,,\quad 0<r_0\ll1\,;\qquad \mathcal{H}_1(r_0)\sim(1-r_0)\left(\frac{E(1)}{\bar{E}}-1\right)>0\,,\quad 0<1-r_0\ll1\,.\tag{4.8}$$

Therefore, $\mathcal{H}_1(r_0)>0$ if we can show that $\mathcal{H}_1$ has a unique critical point $r_0^\star$, with $0<r_0^\star<1$. This point must correspond to the positive global maximum of $\mathcal{H}_1$ on $0<r_0<1$. We readily calculate that any critical point of $\mathcal{H}_1$ on $0<r_0<1$ is a root of $C(r_0)=0$, where $C(r_0)\equiv E(r_0)-\bar{E}$. Since $E(0)<\bar{E}<E(1)$ and $E'(r_0)>0$, we calculate $C(0)<0$, $C(1)>0$, and $C'(r_0)=E'(r_0)>0$. This unique critical point of $\mathcal{H}_1$, in combination with the (positive) local behavior (4.8) near $r=0$ and $r=1$, proves that $\mathcal{H}_1(r_0)>0$ on $0<r_0<1$. ■

Qualitatively, this result shows that when both the bulk and boundary feed for the inhibitor is sufficiently biased toward the boundary, the spots will equilibrate at locations nearer to the domain boundary where there is more "fuel", than for the corresponding closed system with a spatially uniform bulk feed. A similar result characterizing the migration of 1-D spikes to the boundary for the Brusselator with a boundary feed was obtained in [23].

To illustrate Proposition 4.2, we choose $E=ar^2+1$ for which, from (2.9), we readily calculate

$$v_2(r)=a\left(\frac{r^2}{8}-\frac{r^4}{16}\right)-\frac{a}{24}\,.\tag{4.9}$$

For this choice, (4.5) becomes

$$\frac{dr_0}{d\sigma}=\frac{\gamma(S_c)}{D^{1/2}}\left[H_0(r_0)+H_1(r_0)\right],\qquad H_0(r_0)+H_1(r_0)=-\frac{1}{2}\left(r_0+\frac{ar_0^3}{2}\right)+\frac{S_{c0}}{N}\left(\frac{(N-1)}{2r_0}-\frac{Nr_0^{2N-1}}{1-r_0^{2N}}\right).\tag{4.10}$$

When $a>0$, then $E(r)$ is monotone increasing and from Proposition 4.2 the ODE (4.10) has a unique stable steady-state r_{0E} in $0<r_{0E}<1$, with $r_{0E}>r_{0E}^0$. Here r_{0E}^0 is the steady-state location for the closed system where $A=0$ and $E\equiv1$.

For $A=1$ and $a=5$, in Fig. 3(a) we show a favorable comparison between the slow dynamics of a ring of $N=5$ spots, as predicted by the asymptotics (4.10), and that obtained from a numerical finite element solution of (1.2) using FlexPDE [7] (on the order of 10000 nodes were used). For $A=1$ and $N=5$, in Fig. 3(b) we show a favorable comparison between the steady-state ring radius r_{0E} versus a, as obtained by numerically finding the root of $H_0(r_0)+H_1(r_0)=0$, and the corresponding value obtained from evolving the numerical solution to (1.2) to a steady-state. We remark that although the condition $E'(r)\geq0$ in Proposition 4.2 is sufficient for the existence of a unique stable steady-state ring radius, it is not necessary. In particular, for $E=1+ar^2$, the numerical computations in the right panel of Fig. 3 for the zeroes of H_0+H_1 when $A=1$ and $N=5$ shows that there is still a unique steady-state ring radius on the entire range $-1<a<0$ where E is positive but monotone decreasing.

When the bulk feed $E=E(r)$ is not monotone decreasing, we now show that an N-spot ring pattern can undergo distinctly different dynamics than for the case of a uniform bulk feed. We will illustrate this for the choice

$$E(\mathbf{x})=a_0+a_1\delta(\mathbf{x})\,,\tag{4.11}$$

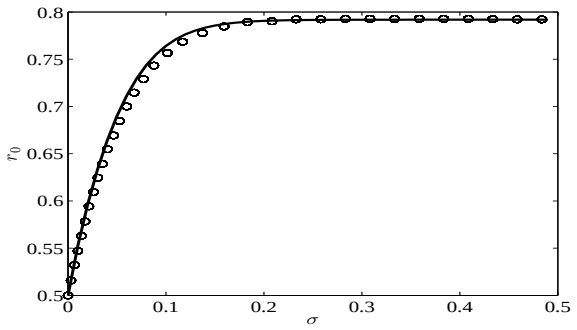

(a) ring radius dynamics for $N = 5$

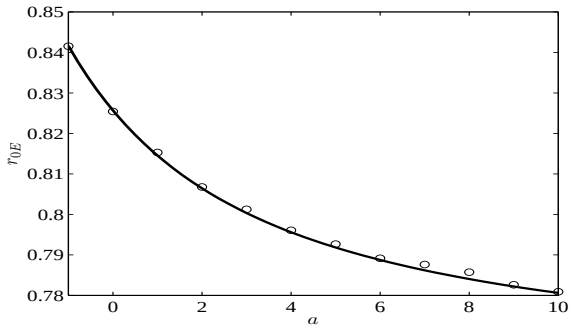

(b) r_{0E} versus a with $A = 1$

Figure 3: Left panel: evolution of the ring radius r_0 against slow time $\sigma = \varepsilon^2 t$ when $N = 5$. The parameters are $D = 0.08$, $f = 0.7$, $A = 1$, $a = 5$, and $\varepsilon = 0.01$. Right panel: steady-state ring radius when $N = 5$ and $A = 1$ for various a, where the bulk feed is radially symmetric and given by $E = ar^2 + 1$. For reference, we note that the steady-state ring radius for $a = A = 0$ is approximately $r_{0E}^0 = 0.625$. In both figures, the solid curve (open circles) is the asymptotic result (numerically computed values).

where $a_0 > 0$ and $a_1 > 0$, and $\delta(\mathbf{x})$ is the Dirac function. This choice models a concentrated source of "fuel" at the center of the disk. In terms of the Neumann Green's function, the solution v_2 to (2.9) is

$$v_2 = a_1 G(\mathbf{x}; \mathbf{0}) = a_1 \left(-\frac{1}{2\pi} \log r + \frac{r^2}{4\pi} - \frac{3}{8\pi} \right), \quad \text{where} \quad r = |\mathbf{x}| \,. \tag{4.12}$$

Moreover, since Ω is the unit disk, we calculate from (2.4) that the common spot source strength S_c is

$$S_c = \frac{A|\partial\Omega| + \int_\Omega E(\mathbf{x})\, d\mathbf{x}}{2\pi N\sqrt{D}} = \frac{1}{2\pi N\sqrt{D}} \left(2\pi A + a_0\pi + a_1 \right) . \tag{4.13}$$

Upon substituting (4.12) and (4.13) into (4.4), we obtain, after some algebra, that the ODE for the ring radius is

$$\frac{dr_0}{d\sigma} = -\frac{\gamma(S_c)}{2\pi r_0\sqrt{D}} \mathcal{N}(r_0) \,, \qquad \mathcal{N}(r_0) \equiv \beta + a_0\pi r_0^2 + (2\pi A + \pi a_0 + a_1) \frac{r_0^{2N}}{1 - r_0^{2N}} \,, \tag{4.14a}$$

where β is defined by

$$\beta \equiv \frac{(N+1)}{2N} \left[a_1 - (2\pi A + \pi a_0) \left(\frac{N-1}{N+1} \right) \right] . \tag{4.14b}$$

As we now show, the dynamics of the ring under (4.14a) depends critically on the sign of β in (4.14b).

Proposition 4.3 *For a ring pattern of $N \geq 2$ spots for Case I with a boundary feed and where the bulk feed is $E(\mathbf{x}) = a_0 + a_1\delta(\mathbf{x})$, with $a_0 > 0$ and $a_1 > 0$, there is a unique and stable steady-state of the ring dynamics (4.14) only when*

$$a_1 < a_{1c} \equiv \left(\frac{N-1}{N+1} \right) (2\pi A + \pi a_0) \,. \tag{4.15}$$

When $a_1 > a_{1c}$, then for any initial condition $r_0(0)$ in $0 < r_0(0) < 1$, r_0 tends to zero at some finite time $\sigma = \sigma_c$ with limiting asymptotics $r_0 \sim \sqrt{c(\sigma_c - \sigma)}$ as $\sigma \to \sigma_c^-$, where $c \equiv \gamma(S_c)\beta/(\pi\sqrt{D})$. Here $\sigma_c < \infty$ is called the collapse time for the ring.

Proof: We observe from (4.14b) that $\mathcal{N}(0) = \beta$, and that $\beta > 0$ iff $a_1 > a_{1c}$. Moreover, we have $\mathcal{N}(r_0) \to +\infty$ as $r_0 \to 1^-$, and

$$\mathcal{N}'(r_0) = 2a_0\pi r_0 + (2\pi A + \pi a_0 + a_1) \frac{2N r_0^{2N-1}}{\left(1 - r_0^{2N}\right)^2} > 0 \quad \text{on} \quad 0 < r_0 < 1 \,, \tag{4.16}$$

so that $\mathcal{N}$ is monotone increasing in r_0. It follows that the ODE (4.14a) has a unique stable steady-state solution only when $a_1 < a_{1c}$. When $a_1 > a_{1c}$, then $\mathcal{N}(r_0) > 0$ on $0 < r_0 < 1$, and we can separate variables in this ODE to get that $r_0 \to 0$ as $\sigma \to \sigma_c \equiv 2\pi\sqrt{D}[\gamma(S_c)]^{-1}\int_0^{r_0(0)}[\xi/\mathcal{N}(\xi)]\,d\xi$. This readily yields the local behavior $r_0 \sim \sqrt{c(\sigma_c - \sigma)}$ as $\sigma \to \sigma_c^-$, where $c \equiv \gamma(S_c)\beta/(\pi\sqrt{D})$. ■

Qualitatively this result shows that for a fixed boundary flux $A > 0$ and for a fixed background bulk "fuel" a_0, then as the "fuel" supply a_1 at the center of the disk is increased beyond a threshold, the spots on the ring will overcome the stabilizing effect of their mutual inter-spot repulsion and will drift slowly towards the center of the disk, which they reach in finite time. We remark that as the distance between the spots decreases as the ring collapses, a competition (overcrowding) instability may be triggered. Further, since our asymptotic derivation of the ODE for slow spot dynamics (4.14) is invalid when two spots are within a spatial distance of $\mathcal{O}(\varepsilon) \ll 1$, the ODE is no longer valid when $r_0 = \mathcal{O}(\varepsilon)$. As such, although we can predict a finite-time collapse of the ring, the dynamics during and after the triggering of the competition instability, along with the detailed behavior of the dynamics of the ring within $\mathcal{O}(\varepsilon)$ of the origin, cannot be captured by (4.14).

The result in Proposition 4.3 can be rephrased in terms of a critical value A_c of the boundary flux so as to prevent a finite-time collapse of the ring. We state our next result in terms of a normalized bulk fuel supply.

Corollary 4.4 *Consider a ring pattern of $N \geq 2$ spots for Case I with a boundary feed $A > 0$ and a bulk feed $E(\mathbf{x}) = a_0 + a_1\delta(\mathbf{x})$ normalized by $|\Omega|^{-1}\int_\Omega E(\mathbf{x})\,d\mathbf{x} = 1$, so that $a_0 + a_1/\pi = 1$ with $a_0 > 0$ and $a_1 > 0$. Then, if $A > A_c \equiv -1/2 + a_1 N/(\pi(N-1))$, the ODE (4.14) has a unique stable steady-state r_{0e} in $0 < r_{0e} < 1$ for any a_1 in $0 < a_1 < \pi$. Alternatively, if $0 \leq A < A_c$, the ring pattern undergoes a finite-time collapse at the origin when a_1 satisfies*

$$\frac{\pi(N-1)}{2N}(2A+1) < a_1 < \pi\,. \tag{4.17}$$

The proof of this result follows readily from Proposition 4.3 and is omitted. Qualitatively, this result shows that as the boundary flux is increased past a threshold, the destabilizing effect on the ring dynamics of the concentrated fuel supply at the origin, leading to a finite-time collapse, is overcome and the ring-radius has a stable steady-state in $0 < r_0 < 1$.

In Fig. 4, we demonstrate the two possible scenarios on a two-spot pattern initialized on a ring of radius $r_0(0) = 0.5$. With $a_0 = 1/2$ and $a_1 = \pi/2$, we calculate that $A_c = 1/2$. In Fig. 4(a), we set $A = 0 < A_c$ so that the theory (solid curve) predicts a finite-time collapse of the ring to a radius of zero. This is corroborated by the results of full numerical solutions (open circles) of (1.2a) with Case I of (1.2b). However, before the collapse completes, a competition instability is triggered as the distance between the spots is reduced past a critical threshold. The solid circle indicates the time at which the difference in height between the two spots is 5% of the quasi-equilibrium value. In Fig. 4(b), we set $A = 0.75 > A_c$. Instead of a finite-time collapse, the radius of the ring reaches an equilibrium value, similar to that predicted by the theory.

We remark that in the full numerical computation of (1.2) we cannot use (4.11) directly, but instead need a regularized form

$$E_\eta(\mathbf{x}) = a_0 + a_1 F(\mathbf{x};\boldsymbol{\xi},\eta)\,, \qquad \text{where} \qquad F(\mathbf{x};\boldsymbol{\xi},\eta) \equiv \frac{1}{\eta\pi}e^{-\frac{1}{\eta}|\mathbf{x}-\boldsymbol{\xi}|^2}\,. \tag{4.18}$$

Here we assume that $\eta > 0$ is $\mathcal{O}(1)$ with respect to ε, but is sufficiently small so that, for some $\mathcal{O}(1)$ value of k, we have

$$\int_{|\mathbf{x}-\boldsymbol{\xi}|<k\eta} F(\mathbf{x};\boldsymbol{\xi},\eta)\,d\mathbf{x} \approx 1\,.$$

As shown in Appendix A, with this regularization, an improved approximation for the spot source strength S_c in (4.13) is

$$S_c = \frac{1}{2\pi N\sqrt{D}}\left(2\pi A + a_0\pi + \tilde{a_1}\right)\,. \tag{4.19}$$

where $\tilde{a}_1$ is the effective strength of the source given by $\tilde{a}_1 = a_1 + \mathcal{O}(\varepsilon^2\eta^{-1})$ (see (A.3) in Appendix A). By using (4.19) for S_c in (4.14), we obtain better agreement between the theory and numerical results.

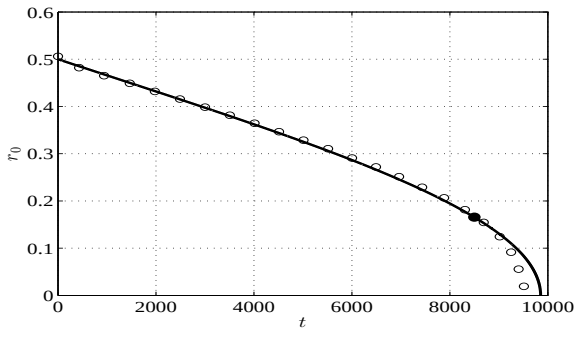

(a) finite-time collapse of ring when $A < A_c$

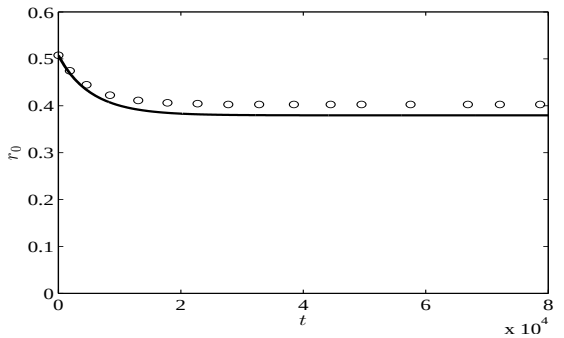

(b) stable ring steady-state when $A > A_c$

Figure 4: Left panel: Dynamics of the ring radius with $N = 2$ spots and $A < A_c$ under the influence of a concentrated source of fuel located at the origin, as given by (4.11) with $a_0 = 1/2$ and $a_1 = \pi/2$. Here, the critical value of A below which a finite-time collapse of the ring occurs is computed from Corollary 4.4 as $A_c = 1/2$. The open circles denote the numerical result for the time-evolution of the ring obtained from solving (1.2a) with Case I of (1.2b), while the solid line represents the asymptotic prediction given by (4.14). Consistent with the theory, the radius undergoes a finite-time collapse. Before the collapse is completed, the pattern undergoes a competition instability as the distance between the spots decreases. The solid circle indicates the time at which the difference in height between the two spots is 5% of the equilibrium value. The parameters are: $\varepsilon = 0.005$, $f = 0.7$, $D = 0.04$, $\tau = 0.02$, and $A = 0$. For the approximation of the Dirac function in (4.11), we use (4.18) with $\eta = 0.003$ and $\boldsymbol{\xi} = (0, 0)$. Right panel: Same parameters, except $A = 0.75 > A_c$. As predicted by the theory, the ring evolves to a non-zero equilibrium value.

4.1.1 One-spot dynamics for Case I

Here we study one-spot dynamics in the unit disk Ω. We will consider both a radially symmetric bulk feed $E(r)$, and a bulk feed that has concentration at some arbitrary point $\mathbf{x} = \boldsymbol{\xi} \in \Omega$.

For the case where E is radially symmetric, we can set $N = 1$ in (4.4) and then solve (2.9) for v_2'. In this way, we get that the distance r_0 of the spot from the center of the disk satisfies

$$\frac{dr_0}{d\sigma} = -\frac{\gamma(S_c)}{\sqrt{D}} r_0 \left[\frac{1}{r_0^2} \int_0^{r_0} \eta E(\eta)\, d\eta + \frac{S_{c0}}{1 - r_0^2} \right], \qquad \text{where} \quad S_{c0} = A + \int_0^1 \eta E(\eta)\, d\eta\,. \tag{4.20}$$

Since the term in the square brackets is always positive, it follows that $r_0 = 0$ is the unique steady-state, and that $r_0 \to 0$ as $\sigma \to \infty$ for any initial condition $r_0(0)$ in $0 < r_0(0) < 1$. Therefore, a one-spot solution always tends to the center of the disk for any boundary feed $A > 0$ and bulk feed $E(r) > 0$, with no monotonicity requirement on $E(r)$.

Next, we consider the qualitatively more interesting scenario where the bulk feed $E(\mathbf{x})$ is concentrated near some point $\boldsymbol{\xi} \in \Omega$ in the unit disk, with the form

$$E(\mathbf{x}) = a_0 + a_1 \delta(\mathbf{x} - \boldsymbol{\xi})\,, \tag{4.21}$$

where $a_0 > 0$ and $a_1 > 0$. We will show that this choice for E leads to a saddle-node bifurcation behavior of spot equilibria and a possible spot-pinning at the point of concentration of $E(\mathbf{x})$.

For this form of E, the solution v_2 to (2.9) is simply $v_2(\mathbf{x}) = a_1 G(\mathbf{x}; \boldsymbol{\xi})$, where $G(\mathbf{x}; \boldsymbol{\xi})$ is the Neumann Green's function of (2.6). From Proposition 3.1, and upon using $\nabla_{\mathbf{x}} v_{1p}(\mathbf{x}_1) = \mathbf{x}_1$ (see (2.8)) and $\nabla v_2(\mathbf{x}_1) = a_1 \nabla_{\mathbf{x}} G(\mathbf{x}_1; \boldsymbol{\xi})$, we obtain from (3.8) that the slow dynamics of the spot centered at $\mathbf{x}_1$ is

$$\frac{d\mathbf{x}_1}{d\sigma} = \gamma(S_1) \left[D^{-1/2} \left(A\mathbf{x}_1 + a_1 \nabla_{\mathbf{x}} G(\mathbf{x}_1; \boldsymbol{\xi}) \right) - 2\pi S_1 \nabla_{\mathbf{x}} R(\mathbf{x}_1) \right], \qquad S_1 = \frac{(2\pi A + a_0 \pi + a_1)}{2\pi\sqrt{D}}\,. \tag{4.22}$$

For the unit disk, $\nabla_{\mathbf{x}} G(\mathbf{x}_1; \boldsymbol{\xi})$ and $\nabla_{\mathbf{x}} R(\mathbf{x}_1)$ can be calculated explicitly as (see equation (4.2) of [13]),

$$\nabla_{\mathbf{x}} G(\mathbf{x}_1; \boldsymbol{\xi}) = \frac{1}{2\pi} \left[-\frac{(\mathbf{x}_1 - \boldsymbol{\xi})}{|\mathbf{x}_1 - \boldsymbol{\xi}|^2} - \frac{\mathbf{x}_1 |\boldsymbol{\xi}|^2 - \boldsymbol{\xi}}{|\mathbf{x}_1|^2 |\boldsymbol{\xi}|^2 - 2\mathbf{x}_1 \cdot \boldsymbol{\xi} + 1} + \mathbf{x}_1 \right], \qquad \nabla_{\mathbf{x}} R(\mathbf{x}_1) = \frac{1}{2\pi} \left[\frac{2 - |\mathbf{x}_1|^2}{1 - |\mathbf{x}_1|^2} \right] \mathbf{x}_1\,, \tag{4.23}$$

where $\cdot$ denotes the dot product. Upon substituting (4.23) into (4.22) we obtain the following result:

Proposition 4.5 *Consider one-spot dynamics for Case I with a boundary feed and with a concentrated bulk feed modeled by* $E(\mathbf{x}) = a_0 + a_1\delta(\mathbf{x}-\boldsymbol{\xi})$*, where* $a_0 > 0$ *and* $a_1 > 0$*. Then, assuming that the spot profile is stable on* $\mathcal{O}(1)$ *time-scales, the slow evolution of the spot centered at* $\mathbf{x} = \mathbf{x}_1$ *satisfies the ODE*

$$\frac{d\mathbf{x}_1}{d\sigma} = -\frac{a_1\gamma(S_1)}{2\pi\sqrt{D}}\mathcal{H}_A(\mathbf{x}_1)\,, \tag{4.24a}$$

where $\mathcal{H}_A(\mathbf{x}_1)$ *is defined by*

$$\mathcal{H}_A(\mathbf{x}_1) \equiv \frac{\mathbf{x}_1-\boldsymbol{\xi}}{|\mathbf{x}_1-\boldsymbol{\xi}|^2} + \frac{\mathbf{x}_1|\boldsymbol{\xi}|^2-\boldsymbol{\xi}}{|\mathbf{x}_1|^2|\boldsymbol{\xi}|^2-2\mathbf{x}_1\cdot\boldsymbol{\xi}+1} + \frac{\mathbf{x}_1}{1-|\mathbf{x}_1|^2}\left(b+\frac{a_0\pi}{a_1}\left(2-|\mathbf{x}_1|^2\right)\right), \qquad b \equiv 1+\frac{2\pi A}{a_1}\,. \tag{4.24b}$$

For a given $\boldsymbol{\xi}$, with $|\boldsymbol{\xi}| < 1$, we now investigate the steady-state solutions of the dynamics (4.24a), as given by the roots of $\mathcal{H}_A(\mathbf{x}_1) = 0$. We first claim that any such root $\mathbf{x}_{1e}$ must be on the same ray through the origin as the source point $\boldsymbol{\xi}$. To prove this, let $\mathbf{z}$ be a unit vector orthogonal to $\boldsymbol{\xi}$, i.e. $\mathbf{z}\cdot\boldsymbol{\xi} = 0$. Then, taking the dot product of the expression $\mathcal{H}_A(\mathbf{x}_1) = 0$ in (4.24b) we get that $\mathbf{z}\cdot\mathbf{x}_{1e} = 0$, which shows that the points $\mathbf{0}$, $\boldsymbol{\xi}$, and $\mathbf{x}_{1e}$ are colinear.

Therefore, without loss of generality we can take $\boldsymbol{\xi} = (\xi, 0)$, with $\xi > 0$, and $\mathbf{x}_{1e} = (x_e, 0)$. Then, the equilibria of the slow dynamics are roots $x_1 = x_e$ of the nonlinear equation

$$\frac{1}{x_1-\xi} + \frac{\xi}{\xi x_1 - 1} + \frac{x_1}{1-x_1^2}\left(b+\frac{a_0\pi}{a_1}\left(2-x_1^2\right)\right) = 0\,, \qquad b \equiv 1+\frac{2\pi A}{a_1}\,. \tag{4.25}$$

Although (4.25) is still rather intractable analytically, we can easily find its solutions numerically for a fixed ξ. To illustrate our results we set $A = 0$ (no boundary fuel) and $\xi = 0.7$, and in Fig. 5(a) we plot the roots of (4.25) as the ratio a_1/a_0 is varied. For small a_1/a_0, where there is relatively little concentrated "fuel", there is an equilibrium state near the origin and one near the fuel source ξ, as is evident from a simple perturbation calculation for (4.25) in the limit $a_1/a_0 \to 0$. As shown in Fig. 5(a), as a_1/a_0 is increased these two branches of equilibria of the one-spot ODE dynamics coalesce at a saddle-node bifurcation point. For $\xi = 0.7$, our computations show that the ODE dynamics has no steady-state when $a_1/a_0 > 0.721$. Moreover, from a numerical computation of the Jacobian of $\mathcal{H}_A(\mathbf{x}_1)$, we obtain that the left and right branches of equilibria in Fig. 5(a) are linearly stable and unstable fixed points, respectively, of the ODE dynamics.

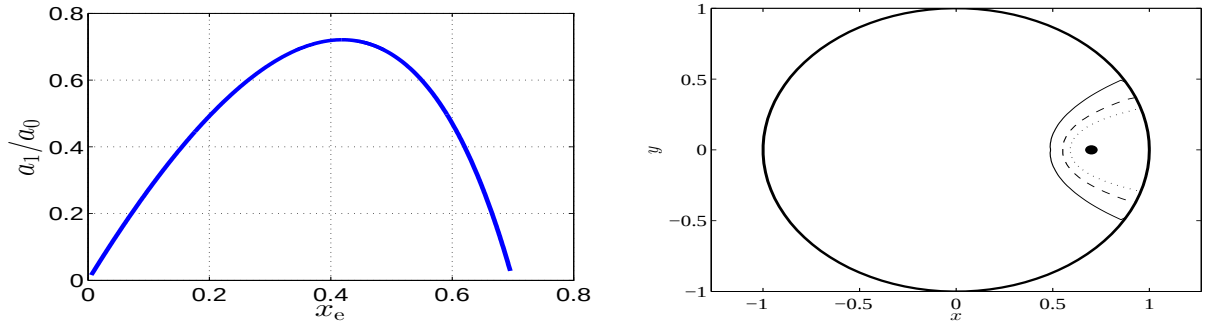

(a) equilibria of the ODE (4.24)

(b) basin of attraction in the unit disk for the ODE

Figure 5: Left panel: Bifurcation behavior of equilibria $\mathbf{x}_1 = (x_e, 0)$ *of the ODE dynamics (4.24) versus the ratio* a_1/a_0 *of the parameters in the bulk feed* $E(\mathbf{x}) = a_0 + a_1\delta(\mathbf{x}-\boldsymbol{\xi})$*. We neglect boundary feed (i.e.* $A = 0$*) and put the "fuel" source at* $\boldsymbol{\xi} = (0.7, 0)$*. The two branches of equilibria meet at a saddle-node point, and no equilibria, being roots of (4.25), exist when* $a_1/a_0 > 0.721$*. The left and right branches of equilibria are linearly stable and unstable fixed points of the ODE dynamics, respectively. Right panel: the boundary of the basin of attraction for the ODE (4.24) for* $a_1/a_0 = 0.5$ *(dotted curve), for* $a_1/a_0 = 0.6$ *(dashed curve), and for* $a_1/a_0 = 0.7$ *(solid curve). The fuel source is concentrated at* $\boldsymbol{\xi} = (0.7, 0)$ *(black dot). For an initial spot location* $\mathbf{x}_1(0)$ *in the rightmost region bounded by these curves and the domain boundary, the spot will become pinned to the fuel source in finite time. Otherwise, the spot will drift to the unique stable steady-state of the ODE (4.24) corresponding to the left branch of Fig. 5(a).*

When (4.24) has no equilibria in the unit disk, a spot can become pinned in finite time at the point $\boldsymbol{\xi}$ of concentration of E. From (4.24a), we observe that when $\mathbf{x}_1$ is near $\boldsymbol{\xi}$, then $\mathbf{x}_1(\sigma)$ has the local behavior $d\mathbf{x}_1/d\sigma \sim -c(\mathbf{x}_1-\boldsymbol{\xi})/|\mathbf{x}_1-\boldsymbol{\xi}|^2$ for some $c>0$. This yields that $d|\mathbf{x}_1-\boldsymbol{\xi}|/d\sigma \sim -c/|\mathbf{x}_1-\boldsymbol{\xi}|$, so that $|\mathbf{x}_1-\boldsymbol{\xi}| \sim \sqrt{2c(\sigma_c-\sigma)} \ll 1$ as $\sigma \to \sigma_c^-$ for some finite $\sigma_c < \infty$. Our ODE for spot dynamics, however, is invalid when $|\mathbf{x}-\boldsymbol{\xi}| = \mathcal{O}(\varepsilon)$.

When $a_1/a_0 < 0.721$ and $\boldsymbol{\xi} = (0.7, 0)$, the ultimate fate of the dynamics of a spot under the ODE (4.24a) depends on its initial location $\mathbf{x}_1(0)$. If the initial spot location is relatively close to the point $\boldsymbol{\xi}$ of concentration of the fuel, it will become pinned there at some finite time. Otherwise, the spot slowly drifts to an intermediate steady state location corresponding to the left branch of Fig. 5(a). The basin of attraction for initial spot locations corresponding to these two distinct realizations of the ODE dynamics is shown in Fig. 5(b) for three values of the ratio a_1/a_0.

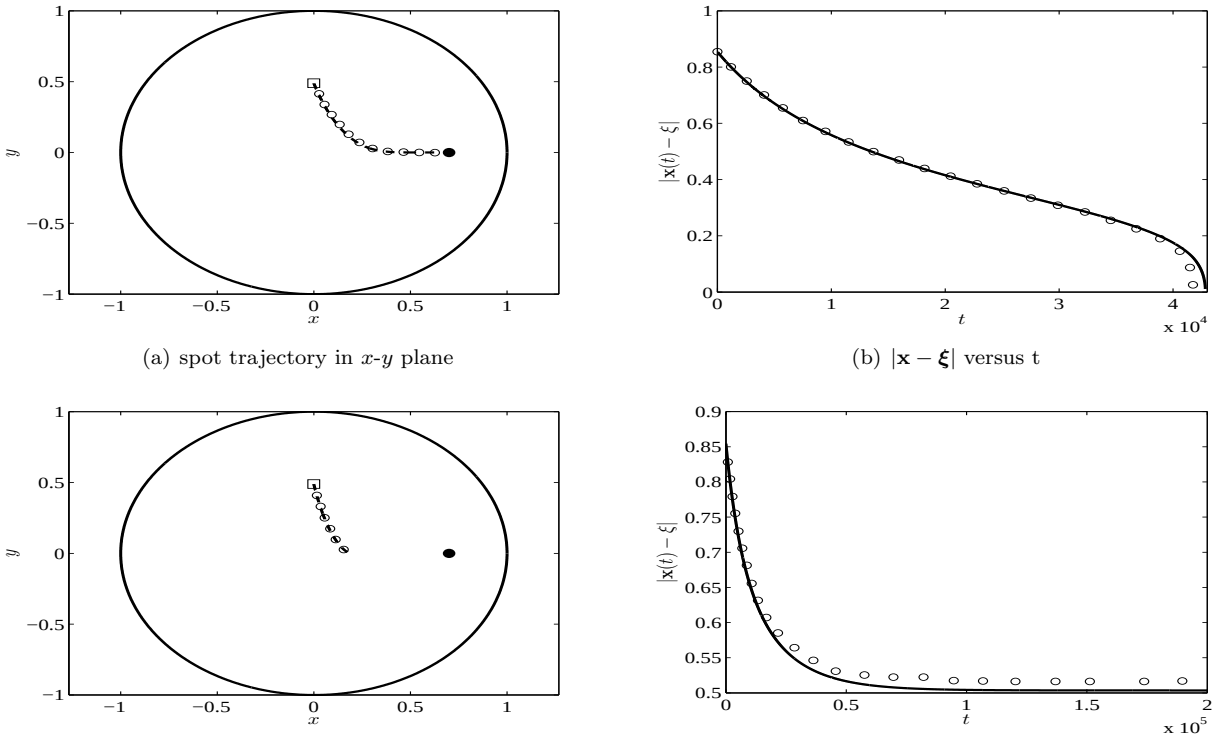

(a) spot trajectory in x-y plane

(b) $|\mathbf{x}-\boldsymbol{\xi}|$ versus t

(c) spot trajectory in x-y plane

(d) $|\mathbf{x}-\boldsymbol{\xi}|$ versus t

Figure 6: Top left panel: the trajectory $\mathbf{x}_1$ of the spot in the unit disk, as computed from the ODE (4.24), for the bulk feed $E(\mathbf{x}) = a_0 + a_1\delta(\mathbf{x}-\boldsymbol{\xi})$ with $a_0 = a_1 = 1$, and no boundary feed $A = 0$. The point $\boldsymbol{\xi}$ of concentration of the "fuel", with $\boldsymbol{\xi} = (0.7, 0)$, is given by the solid dot, while the initial location $\mathbf{x}_1(0)$ is indicated by the square. Since $a_1/a_0 > 0.721$, Fig. 5(a) shows that there is no steady-state $\mathbf{x}_{1e}$ of the ODE dynamics (4.24) with $\mathbf{x}_{1e} \neq \boldsymbol{\xi}$. The spot initially drifts towards the origin, representing its steady-state location in the absence of a concentrated fuel source. However, the attraction towards the source point $\boldsymbol{\xi}$ eventually dominates the dynamics and the spot becomes pinned to $\boldsymbol{\xi}$ in finite time. The dashed curve is the asymptotic result obtained from (4.24) while the hollow circles are the numerical results computed from (1.2) using FlexPDE [7]. Top right panel: the distance from the spot to the source location as a function of time. Finite-time pinning is suggested by the steep gradient near where this distance vanishes. Parameters for both panels are $D = 0.5$, $f = 0.7$, $\varepsilon = 0.01$, $\tau = 0.1$, and $\eta = 0.003$ in (4.18). Bottom left and bottom right panels: Same as the top panels except $a_0 = 1$ and $a_1 = 1/2$. Since $a_1/a_0 < 0.721$, the spot settles into an equilibrium location $(x_e, 0)$ on the positive x-axis between the origin and the source point. The numerics predicts an equilibrium distance $|(x_e, 0) - \boldsymbol{\xi}| \approx 0.516$, near the asymptotically predicted value of $|(x_e, 0) - \boldsymbol{\xi}| \approx 0.503$. That is, from Fig. 5(a), the spot settles near the predicted stable equilibrium of $(x_e, 0) = (0.197, 0)$ as given on the left solution branch of the bifurcation diagram.

In Fig. 6, we illustrate the two possible outcomes of the dynamics of a one-spot pattern under the influence of a localized source $E(\mathbf{x})$ of (4.21) with $a_0 = a_1 = 1$ and $\boldsymbol{\xi} = (0.7, 0)$. Figs. 6(a) and 6(b) show the spot-pinning behavior for a one-spot solution for the bulk feed when a_1/a_0 is above the saddle point of Fig. 5(a). As such, no steady-state $\mathbf{x}_{1e}$ of the ODE dynamics (4.24) with $\mathbf{x}_{1e} \neq \boldsymbol{\xi}$ exists. The results in Fig. 6(b) show that the asymptotic ODE dynamics of (4.24) (solid) compares rather well with the full numerical results (open circles) computed from (1.2) using FlexPDE [7]

until the distance $|\mathbf{x}_1 - \boldsymbol{\xi}|$ becomes small. Figs. 6(c) and 6(d) show the scenario where $a_0 = 1$ and $a_1 = 1/2$. Since a_1/a_0 is below the saddle point of Fig. 5(a), the spot is expected to settle to an equilibrium location of $(x_e, 0)$ with $x_e \approx 0.197$ given by the left branch of Fig. 5(a). This is consistent with the fact that in Fig. 6(d), the distance between the spot and the source point settles to an equilibrium value of approximately 0.503. For the full numerical computation of (1.2), we use a regularized form of the Dirac function given by (4.18). In the ODE, we use the effective strength $\tilde{a}_1$ instead of a_1 for S_1 in (4.24). See Appendix A for the formula for $\tilde{a}_1$, and also for the corresponding result computed without using this correction.

4.2 Case II: Dynamics and quasi-equilibria

Let Ω be the unit disk and consider an N-spot ring pattern, with $N \geq 2$, where the ring of radius r_0 is concentric within the disk. By the same analysis leading to (4.4), we obtain from Proposition 3.2 together with (2.29) and (2.25) that the DAE system for the ring radius consists of the dynamics

$$\frac{dr_0}{d\sigma} = -\gamma(S_c)\left[\frac{r_0}{2\sqrt{D}} + \frac{\pi S_c}{N} p'_\kappa(r_0)\right], \tag{4.26a}$$

coupled to a nonlinear algebraic system for the common spot source strength S_c given by

$$S_c\left(1 + 2\pi\nu\frac{p_\kappa(r_0)}{N}\right) + \nu\chi(S_c) = D^{1/2}\nu\left(\frac{1}{D}v_3(r_0) + v_b\right), \qquad v_3(r_0) = \frac{(1-r_0^2)}{4} + \frac{1}{2\kappa_0}, \tag{4.26b}$$

where $\nu = -1/\log\varepsilon$. Here $p_\kappa(r_0)$ is defined in terms of the Robin Green's matrix $\mathcal{G}_\kappa$ (see (2.23b)) by

$$p_\kappa(r_0) \equiv \mathbf{e}^T\mathcal{G}_\kappa\mathbf{e}\,. \tag{4.26c}$$

This DAE system (4.26) differs from that for Case I, as analyzed in §4.1, in that the common spot source strength now depends on r_0 from (4.26b). For the ring pattern, $p_\kappa(r_0)$ and $p'_\kappa(r_0)$ are calculated numerically using the explicitly-determined Robin Green's function given in (2.26) with spot locations $\mathbf{x}_j = r_0\mathbf{e}_{\theta_j}$, for $j = 1, \ldots, N$ (see (4.1)).

For a particular parameter set, in Fig. 7(a) we show a very favorable comparison between the dynamics of the DAE system (4.26) for a 5-spot ring pattern with that obtained by numerically solving Case II of (1.2) using FlexPDE [7]. We observe that the ring radius eventually tends to a steady-state value consistent with that predicted by the asymptotic theory. In Fig. 7(b), we plot the steady-state radius versus the Robin parameter $\kappa_0 = \kappa/D$. The qualitatively new feature observed here, in comparison with the study of closed systems with Neumann boundary conditions in [3, 13], is that the Robin boundary condition induces a saddle-node bifurcation structure of steady-state solutions for the DAE system (4.26), with two disconnected solution branches in κ_0. The $\mathcal{O}(1)$ time-scale linear stability analysis of this saddle-node structure is studied in §5.2 below. From this analysis, we obtain that the solid (dashed) portion of the curves in Fig. 7(b) are where the ring pattern is linearly stable (unstable) with respect to $\mathcal{O}(1)$ eigenvalues, representing instabilities of the amplitudes of the spots. Notice that the stability transition occurs near the rightmost saddle-node point. As κ_0 decreases below this rightmost saddle-node point, full numerical computations of the PDE (1.2) reveal a loss of the steady state as multiple spots annihilate and disappear (not shown).

Lastly, we consider the slow dynamics of a one-spot pattern, and we show how increasing the Robin constant leads to a new bifurcation behavior for the steady-state location of the spot. For this $N = 1$ case, we have $p_\kappa(r_0) = R_\kappa(r_0)$, so that the DAE system (4.26) becomes

$$\frac{dr_0}{d\sigma} = \gamma(S_c)H_\kappa(r_0)\,; \qquad H_\kappa(r_0) = -\frac{r_0}{2\sqrt{D}} - \pi S_c R'_\kappa(r_0)\,, \tag{4.27a}$$

where S_c satisfies

$$S_c\left(1 + 2\pi\nu R_\kappa(r_0)\right) + \nu\chi(S_c) = D^{1/2}\nu\left(\frac{1}{D}v_3(r_0) + v_b\right), \qquad v_3(r_0) = \frac{(1-r_0^2)}{4} + \frac{1}{2\kappa_0}\,. \tag{4.27b}$$

From (2.26b), we obtain $R'_\kappa(0) = 0$, so that $H_\kappa(0) = 0$. Therefore, $r_0 = 0$ is a steady-state solution of the one-spot DAE dynamics (4.27) for any $\kappa_0 \geq 0$. This shows that there is always a one-spot steady-state solution at the center of

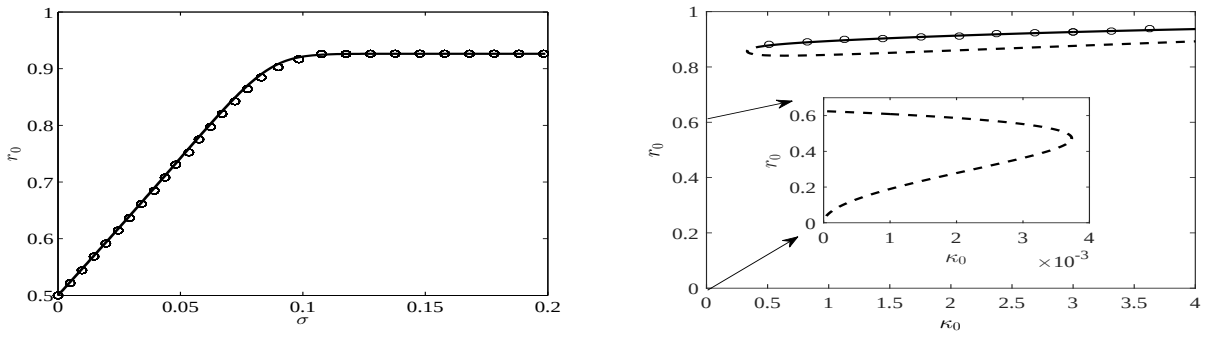

(a) ring radius dynamics for $N = 5$

(b) steady-state ring radius versus κ_0

Figure 7: Left panel: evolution of the ring radius r_0 against slow time $\sigma = \varepsilon^2 t$ when $N = 5$ for the Robin problem Case II. The parameters are $D = 1.4$, $f = 0.7$, $\tau = 0.05$, $\kappa = 4.2$, $v_b = 12$, $\kappa_0 \equiv \kappa/D = 3$, and $\varepsilon = 0.01$. The solid curve is the asymptotic result from the DAE system (4.26) while the open circles are the numerically computed values from the solution of the full PDE (1.2) with Robin boundary conditions using FlexPDE [7]. Right panel: the steady-state ring radius of a 5-spot ring pattern versus κ_0; the other parameters are the same as those in the left panel. The solid (dashed) portion indicates where the pattern is stable (unstable) with respect to $\mathcal{O}(1)$ eigenvalues. Note the existence of two saddle-node points at $\kappa_0 \approx 0.333$ and $\kappa_0 \approx 3.73 \times 10^{-3}$. When κ_0 is between these values, no steady-state ring patterns exist. The $\mathcal{O}(1)$ stability analysis and saddle-node structure are discussed further in §5.2.

the unit disk. We now show the qualitatively new phenomenon that this steady-state location becomes unstable as a solution to the DAE dynamics when κ_0 exceeds some threshold. To analyze this translational instability of the one-spot steady-state solution at the center of the disk, we simply examine the stability of the $r_0 = 0$ steady-state in (4.27). By expanding $R_\kappa(r_0)$, as given in (2.26b), for $r_0 \ll 1$ we readily derive that

$$H_\kappa(r_0) \sim r_0 \left[-\frac{1}{2\sqrt{D}} - S_c \left(\frac{1-\kappa_0}{1+\kappa_0} \right) + \mathcal{O}(r_0^2) \right], \qquad r_0 \ll 1\,. \tag{4.28}$$

This shows that the $r_0 = 0$ steady-state is unstable as a solution to the DAE dynamics (4.27) whenever

$$\frac{1}{2\sqrt{D}} + S_c \left(\frac{1-\kappa_0}{1+\kappa_0} \right) < 0\,. \tag{4.29}$$

Finally, relabeling $\kappa_0 = \kappa/D$, while using $v_3(0) = 1/4 + (2\kappa_0)^{-1}$ and $R_\kappa(0) = (2\pi\kappa_0)^{-1}$, we readily rephrase this stability criterion as follows:

Proposition 4.6 *Consider a one-spot steady-state solution for the Robin problem given by Case II of (1.2) centered at the origin of the unit disk. This solution is unstable to a translational instability of the spot location if and only if*

$$\kappa > D \left[\frac{2S_c\sqrt{D}+1}{2S_c\sqrt{D}-1} \right], \tag{4.30a}$$

where S_c satisfies the nonlinear algebraic equation

$$S_c \left(1 + \frac{\nu}{\kappa} D \right) + \nu\chi(S_c) = D^{1/2}\nu \left(\frac{1}{2\kappa} + \frac{1}{4D} + v_b \right). \tag{4.30b}$$

The inequality (4.30a) is implicitly-defined since S_c depends on κ through (4.30b). In Fig. 8(a), we plot the left-hand (dashed) and right-hand sides of the inequality (4.30a) versus κ for $f = 0.8$ $D = 1$, $\varepsilon = 0.02$, and $v_b = 7$. For this parameter set, Fig. 8(a) shows that a one-spot solution at the origin is stable when $\kappa \lesssim 2.25$ and unstable otherwise.

Next, we validate this theoretical result for the stability threshold of the Robin constant κ. In Fig. 8(b) we plot the slow dynamics of the distance from the origin to the center of the spot for two values of κ on either side of the threshold, as

obtained by numerically solving the DAE dynamics (4.27). From this figure, we observe that when $\kappa = 2$, the spot starting at $(0.05, 0)$ will drift slowly to the origin, whereas when $\kappa = 2.5$ the spot drifts away from the origin to a new nonzero steady-state radius consistent with the asymptotic analysis. As shown in this figure, these results from our asymptotic analysis are confirmed with full numerical simulations of (1.2) using FlexPDE [7].

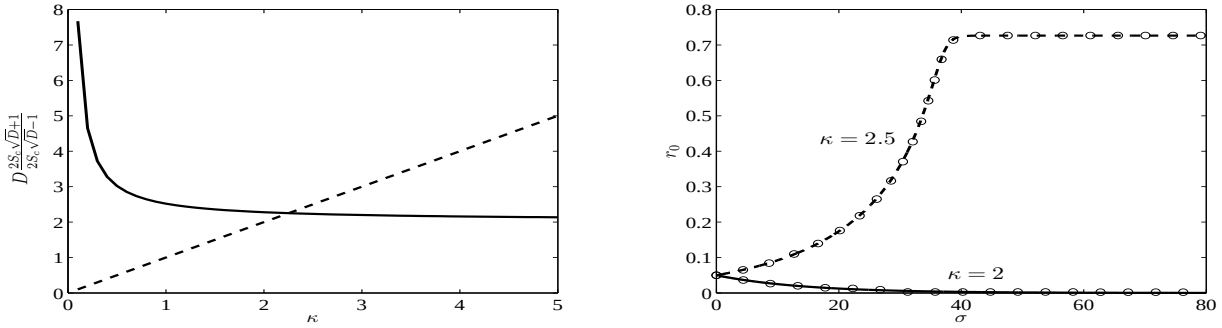

(a) plot of the left- and right-hand sides of (4.30a)

(b) steady-state radius

Figure 8: Left panel: the left-hand (dashed) and right-hand (solid) sides of the inequality (4.30) versus κ. The one-spot solution located at the origin is linear stable (unstable) to translations in the spot location when κ is below (above) the point of intersection ($\kappa \approx 2.25$). Right panel: for a one-spot solution initialized at $(0.05, 0)$, the spot drifts toward the origin when $\kappa = 2$, while it drifts away from the origin to a new nonzero steady-state value when $\kappa = 2.5$. The curves are from the DAE dynamics (4.27), while the open circles are from a numerical solution of the full PDE (1.2). Parameters are $f = 0.8$, $D = 1$, $\varepsilon = 0.02$, $v_b = 7$, and $\tau = 0.05$.

Finally, in Fig. 9(a) we exhibit another type of saddle-node bifurcation structure for the existence of a one-spot steady-state solution centered at the origin where we take the boundary feed term v_b of the inhibitor for Case II of (1.2b) as the bifurcation parameter. For fixed D and κ, this plot shows that a solution to the nonlinear constraint (4.30b) exists only when the ambient inhibitor concentration term v_b is sufficiently large. In Fig. 9(b), we solve (1.2) numerically by FlexPDE [7] and track the amplitude of a spot centered at the origin as v_b is decreased adiabatically according to $v_b = \max(7 - \delta t, v_{bf})$ with $0 < \delta \ll 1$. When v_{bf} is set above the saddle-node value (≈ 5.518), the amplitude of the spot settles to a steady-state value (solid) as v_b is held fixed at v_{bf} indefinitely. However, when v_{bf} is set below the saddle-node point (dashed), the amplitude collapses to zero and the spot disappears. We emphasize that the rapid decay in the spot amplitude near $t = 275$ occurs after v_b has been decreased to v_{bf} ($t = 150$). That is, the decay is due to the loss of the solution past the saddle-node point, and not to an adiabatic tuning of parameters. This qualitatively new saddle-node bifurcation structure will be described in more detail for any $N \geq 1$ in §5.2.

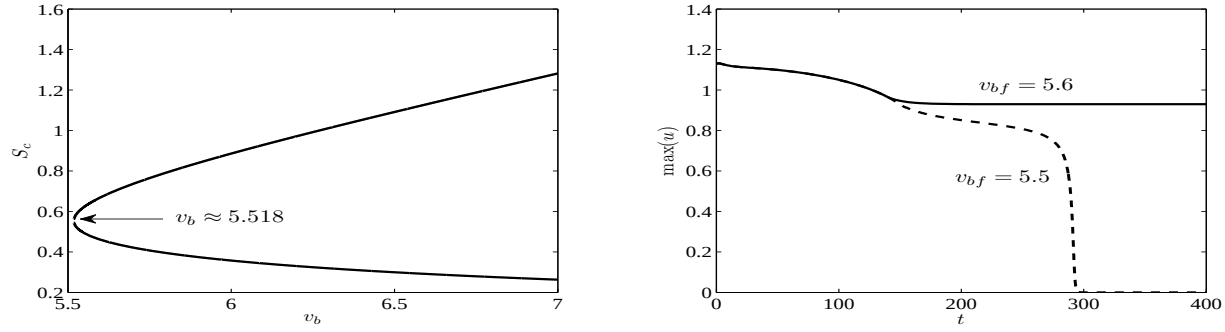

(a) saddle-node behavior in v_b for $N = 1$

(b) $\max(u)$ versus t

Figure 9: Left panel: bifurcation diagram for the nonlinear algebraic constraint (4.30b) exhibiting a saddle-node point at $v_b \approx 5.518$. Right panel: time-evolution of the amplitude of a spot centered at the origin as v_b is slowly decreased according to $v_b = \max(7 - 0.01t, v_{bf})$. When v_{bf} is set above 5.518, the amplitude settles to a steady state value. When $v_{bf} < 5.518$, the amplitude undergoes a rapid decay and the spot disappears. Note that with $v_{bf} = 5.5$, we have set $v_b = 5.5$ for all $t > 150$. Therefore, the rapid decay in amplitude near $t = 275$ occurs while all parameters are held fixed. The parameters are $f = 0.8$, $D = 1$, $\kappa = 2$, and $\varepsilon = 0.02$.

5 Linear stability analysis of quasi-equilibrium patterns

In this section, we analyze the linear stability on an $\mathcal{O}(1)$ time-scale of the N-spot quasi-equilibrium patterns of §2. For Case I with $E = E(\mathbf{x})$, and for Case II with the Robin condition, we will consider three types of instability. The first type, referred to as a peanut-splitting instability (see e.g., [3, 13, 20, 25]), occurs when the strength S_j of the j-th spot exceeds a certain threshold $\Sigma_2(f)$. It is associated with a zero-eigenvalue for a locally non-radially symmetric eigenfunction near the j-th spot. Our numerical computations show that this linear instability triggers a nonlinear spot self-replication event in which the j-th spot splits into two. This instability is a local instability in the sense that the local eigenvalue problems near each spot are uncoupled, except with regards to determining the j-th spot strength, S_j, from the nonlinear algebraic system. The other two types of instabilities are spot amplitude instabilities associated with locally radially symmetric perturbations near the spots. A competition instability occurs as the result of a zero-eigenvalue crossing, which triggers a nonlinear process through which one or more spots are annihilated. The oscillatory instability, which occurs through a Hopf bifurcation when a complex conjugate pair of eigenvalues crosses the imaginary axis, leads to oscillations in the amplitudes of the spots. In contrast to the local peanut-splitting instability, the analysis of both types of amplitude instabilities is more intricate as one must analyze a globally coupled eigenvalue problem (GCEP). This linear stability analysis, which incorporates our three possible sources of heterogeneity consisting of boundary feed, non-uniform bulk feed, and an inhomogeneous Robin condition, is an extension of that given in [20] for one and two-spot patterns on the surface of the sphere with a spatially uniform bulk feed $E \equiv 1$.

5.1 Case I: Constant boundary feed with $E = E(\mathbf{x})$

We consider the linear stability of the N-spot quasi-equilibrium solution for Case I of (1.2) with $E = E(\mathbf{x})$. We perturb the quasi-equilibrium solution according to

$$u = u_e + e^{\lambda t}\phi\,, \qquad v = v_e + e^{\lambda t}\eta\,, \qquad |\phi|,\ |\eta| \ll 1\,, \tag{5.1}$$

where u_e and v_e are given by (2.14) and (2.15), respectively. The linearized system for ϕ and η is then

$$\varepsilon^2\Delta\phi - \phi + 2fu_ev_e\phi + fu_e^2\eta = \lambda\phi\,, \quad \mathbf{x}\in\Omega\,, \qquad \partial_n\phi = 0\,, \quad \mathbf{x}\in\partial\Omega\,, \tag{5.2a}$$

$$D\Delta\eta + \frac{1}{\varepsilon^2}\left(\phi - 2u_ev_e\phi - u_e^2\eta\right) = \tau\lambda\eta\,, \quad \mathbf{x}\in\Omega\,, \qquad \partial_n\eta = 0\,, \quad \mathbf{x}\in\partial\Omega\,. \tag{5.2b}$$

In the inner region near the center of the j-th spot at $\mathbf{x}_j$, where $u_e(\rho)\sim D^{1/2}u_j$ and $v_e(\rho)\sim D^{-1/2}v_j$, we let $\mathbf{y} = \varepsilon^{-1}(\mathbf{x}-\mathbf{x}_j)$ and $\phi(\mathbf{x})\to\Phi_j(\mathbf{y})$ and $\eta(\mathbf{x})\to D^{-1}N_j(\mathbf{y})$ to obtain, to leading order, the inner linearized problem

$$\Delta_{\mathbf{y}}\Phi_j - \Phi_j + 2fu_jv_j\Phi_j + fu_j^2N_j = \lambda\Phi_j\,, \qquad \Phi_j\to 0 \quad \text{as} \quad |\mathbf{y}|\to\infty\,, \tag{5.3a}$$

$$\Delta_{\mathbf{y}}N_j + \Phi_j - 2u_jv_j\Phi_j - u_j^2N_j = 0\,, \tag{5.3b}$$

where we have assumed that $\tau\lambda/D \ll \mathcal{O}(\varepsilon^{-2})$. Here u_j and v_j are solutions to the radially symmetric core problem (2.1). As discussed below, the appropriate far-field behavior for N_j will depend on the nature of the perturbation. We seek a separation of variables solution of the form

$$\Phi_j = \hat{\Phi}_j(\rho)e^{im\theta}\,, \quad N_j = \hat{N}_j(\rho)e^{im\theta}\,, \qquad \mathbf{y} = \rho(\cos(\theta),\sin(\theta))^T\,, \quad \rho = |\mathbf{y}|\,, \tag{5.4}$$

which leads to the eigenvalue problem

$$\mathcal{L}_m\hat{\Phi}_j - (1+\lambda)\hat{\Phi}_j + 2fu_jv_j\hat{\Phi}_j + fu_j^2\hat{N}_j = 0\,, \qquad \hat{\Phi}_j\to 0 \quad \text{as} \quad |\mathbf{y}|\to 0\,, \tag{5.5a}$$

$$\mathcal{L}_m\hat{N}_j + \hat{\Phi}_j - 2u_jv_j\hat{\Phi}_j - u_j^2\hat{N}_j = 0\,, \qquad \text{where} \quad \mathcal{L}_m v \equiv v_{\rho\rho} + \frac{1}{\rho}v_\rho - \frac{m^2}{\rho^2}v\,. \tag{5.5b}$$

We first consider non-radially symmetric perturbations near the spot, for which $m > 0$. Then, due to the $m^2\hat{N}_j/\rho^2$ term in (5.5b), we may impose the far-field decay condition

$$\hat{N}_j\to 0 \quad \text{as} \quad \rho\to\infty\,. \tag{5.5c}$$

Alternatively, for $m = 0$, where the perturbation is radially symmetric near the spot, we must allow $\hat{N}_j$ to grow logarithmically as $\rho \to \infty$. This case, which leads to a global coupling between the spots, is treated separately below. We also remark that the $m = 1$ mode corresponds to the translation mode $(\hat{\Phi}_j, \hat{N}_j) = (u_j', v_j')$ associated with $\lambda = 0$. This can be seen by differentiating (2.1) with respect to y_1 or y_2, and then observing that $(\Phi_j, N_j) = (u_j', v_j')e^{i\theta}$ is a solution of (5.3) when $\lambda = 0$. As a result we only need consider $m = 0, 2, 3, \ldots$.

The relationship of the eigenvalue $\lambda_{\max}$ in (5.5) with the largest real part versus S_j for $m = 2, 3, \ldots$ has been calculated numerically in [20] (see Fig. 4 of [20]), where the dependence of $\lambda_{\max}$ on S_j is through the solution u_j and v_j to the core problem (2.1). Similar to the analogous result for the Schnakenberg model in [13], for each $m = 2, 3, \ldots$, $\lambda_{\max}$ is real and negative (positive) when $S_j < \Sigma_m(f)$ ($S_j > \Sigma_m(f)$). Further, numerical computations on (5.5) show that there exists an ordering principle $\Sigma_2(f) < \Sigma_3(f) < \Sigma_4(f) < \ldots$ (see [20]). Thus, the $m = 2$ mode, called the peanut-splitting mode, is the first to lose stability as S_j is increased. Numerical values of $\Sigma_2(f)$ for some f are shown in Fig. 2.

When Ω is the unit disk with $E(\mathbf{x}) = E(r)$, and when the spots are equally-spaced on a concentric ring, we have that $S_j = S_c$ for $j = 1, \ldots, N$, where S_c is given in terms of the boundary feed A and average bulk feed by (2.17). Qualitatively, we conclude that a spot self-replication process can be triggered when more inhibitor "fuel" is fed into the system, either through the bulk or from the domain boundary, so as to ensure that S_c exceeds the peanut-splitting threshold $\Sigma_2(f)$. Equivalently, for fixed feed rates A and $E(r)$, (2.17) shows that the spots will undergo a peanut-splitting instability when the inhibitor diffusivity D is decreased below a spot-splitting threshold $D_{\rm split}$, defined by

$$D_{\rm split} \equiv \frac{\left[A + \int_0^1 rE(r)\,dr\right]^2}{N^2\Sigma_2^2(f)}\,. \tag{5.6}$$

This result shows that the spot-splitting criterion depends on average, rather than pointwise, values of the bulk feed E.

Next, we consider radially symmetric perturbations where $m = 0$. Since (5.3) is linear and homogeneous, we write

$$\Phi_j = c_j\tilde{\Phi}_j(\rho)\,, \qquad N_j = c_j\tilde{N}_j(\rho)\,, \tag{5.7a}$$

to obtain the radially symmetric problem

$$\Delta_\rho\tilde{\Phi}_j - \tilde{\Phi}_j + 2fu_jv_j\tilde{\Phi}_j + fu_j^2\tilde{N}_j = \lambda\tilde{\Phi}_j\,, \qquad \tilde{\Phi}_j \to 0 \quad \text{as} \quad \rho \to \infty\,, \tag{5.7b}$$

$$\Delta_\rho\tilde{N}_j + \tilde{\Phi}_j - 2u_jv_j\tilde{\Phi}_j - u_j^2\tilde{N}_j = 0\,, \qquad \tilde{N}_j \sim \log\rho + \tilde{B}_j \quad \text{as} \quad \rho \to \infty\,. \tag{5.7c}$$

We make several remarks. First, in contrast to the $m \geq 2$ case, $\tilde{N}_j$ does not decay to zero at infinity. As a result, all the inner eigenvalue problems will be coupled through the outer solution η in (5.2b). Second, the $\log\rho$ term in (5.7c) is a normalization condition and uniquely fixes $\tilde{B}_j = \tilde{B}_j(S_c, \lambda)$, which must be computed numerically. Third, when $\lambda = 0$ in (5.7b), $\tilde{B}_j$ is given by $\tilde{B}_j = \chi'(S_j)$, which can be seen from differentiating the core problem (2.1) with respect to S_j and comparing with (5.7b).

To derive the outer problem for η in (5.2b), we use the same procedure as that employed in obtaining (2.3a) from (1.2a). Then, upon using the $(\phi, \eta) \sim (\tilde{\Phi}, \tilde{N}_j/D)$, we obtain the outer problem

$$\Delta\eta - \frac{\tau\lambda}{D}\eta = \frac{2\pi}{D}\sum_{j=1}^N c_j\delta(\mathbf{x} - \mathbf{x}_j)\,, \quad \mathbf{x} \in \Omega\,, \qquad \partial_n\eta = 0\,, \quad \mathbf{x} \in \partial\Omega\,. \tag{5.8a}$$

To obtain the matching condition for η from the far-field condition of N_j in (5.7c), we recall that $\eta \sim N_j/D$, so that

$$\eta \sim \frac{c_j}{D}\left[\log|\mathbf{x} - \mathbf{x}_j| + \frac{1}{\nu} + \tilde{B}_j\right] \quad \text{as} \quad \mathbf{x} \to \mathbf{x}_j\,, \tag{5.8b}$$

where $\nu \equiv -1/\log\varepsilon$. We write the solution to (5.8) as

$$\eta = -\frac{2\pi}{D}\sum_{i=1}^N c_iG_\lambda(\mathbf{x}; \mathbf{x}_i)\,, \tag{5.9}$$

where the eigenvalue-dependent Green's function $G_\lambda(\mathbf{x};\mathbf{x}_0)$ satisfies

$$\begin{aligned} \Delta G_\lambda - \frac{\tau\lambda}{D} G_\lambda = -\delta(\mathbf{x}-\mathbf{x}_0)\,, \quad \mathbf{x}\in\Omega\,, \qquad \partial_n G_\lambda = 0\,, \quad \mathbf{x}\in\partial\Omega\,; \\ G_\lambda \sim -\frac{1}{2\pi}\log|\mathbf{x}-\mathbf{x}_0| + R_{\lambda 0} + \mathcal{O}(1) \quad \text{as} \quad \mathbf{x}\to\mathbf{x}_0\,. \end{aligned} \tag{5.10}$$

By letting $\mathbf{x}\to\mathbf{x}_j$ in (5.9), and asymptotically matching the resulting expression to (5.8b), we obtain that

$$-2\pi\left(c_j R_{\lambda j} + \sum_{i\neq j}^{N} c_i G_{\lambda ji}\right) = c_j\left(\frac{1}{\nu} + \tilde{B}_j\right)\,; \qquad j=1,\dots,N\,, \tag{5.11}$$

where we have defined $G_{\lambda ji}\equiv G_\lambda(\mathbf{x}_j;\mathbf{x}_i)$. By writing this system in matrix form, we conclude that the discrete eigenvalues λ and corresponding eigenmodes $\mathbf{c}=(c_1,\dots,c_N)^T$ of the eigenvalue problem (5.7) satisfy the transcendental equation

$$\det\mathcal{M}(\lambda)=0\,, \qquad \mathcal{M}\mathbf{c}=\mathbf{0}\,; \qquad \mathcal{M}(\lambda)\equiv\mathcal{I}+2\pi\nu\mathcal{G}_\lambda+\nu\tilde{\mathcal{B}}\,. \tag{5.12a}$$

Here the symmetric Green's matrix $\mathcal{G}_\lambda$ and the diagonal matrix $\tilde{\mathcal{B}}$ are defined by

$$(\mathcal{G}_\lambda)_{ij}\equiv\begin{cases} R_{\lambda j} & i=j \\ G_\lambda(\mathbf{x}_i;\mathbf{x}_j) & i\neq j \end{cases}\,, \qquad (\tilde{\mathcal{B}})_{ij}\equiv\begin{cases}\tilde{B}_j & i=j\\ 0 & i\neq j\end{cases}\,, \qquad i,j=1,\dots,N\,. \tag{5.12b}$$

We refer to (5.12) as the globally coupled eigenvalue problem (GCEP). We will analyze (5.12) in the radially symmetric scenario where Ω is the unit disk, $E=E(r)$, and where $N\geq 2$ spots are equally-spaced on a concentric ring. In this case, the spots have the common strength S_c, given in (2.17), so that $\tilde{\mathcal{B}}$ in (5.12) is a multiple of the identity, i.e. $\tilde{\mathcal{B}}=\tilde{B}(S_c,\lambda)\mathcal{I}$.

Since the problem for G_λ is ill-posed when $\lambda=0$, to analyze instabilities associated with a zero-eigenvalue crossing, we must expand G_λ for small λ as

$$G_\lambda \sim \frac{D}{|\Omega|\tau\lambda} + G(\mathbf{x};\mathbf{x}_0) + \mathcal{O}(\tau\lambda)\,, \tag{5.13}$$

where $G(\mathbf{x};\mathbf{x}_0)$ is the Neumann Green's function of (2.6). Then, the Green's matrix $\mathcal{G}_\lambda$ in (5.12b) becomes

$$\mathcal{G}_\lambda \sim \frac{DN}{|\Omega|\tau\lambda}\mathcal{E} + \mathcal{G} + \mathcal{O}(\tau\lambda)\,, \tag{5.14}$$

for $|\lambda|\ll 1$, where $\mathcal{E}$ and the Neumann Green's matrix $\mathcal{G}$ are defined in (2.13). Substituting (5.14) into (5.12a), we get

$$\left(\mathcal{E}+\frac{2\pi\nu\tau\lambda}{\mu}\mathcal{G}\right)\mathbf{c} = -\frac{\tau\lambda}{\mu}\left[1+\nu\tilde{B}(S_c;\lambda)\right]\mathbf{c}\,; \qquad \text{where} \qquad \mu\equiv\frac{2\pi\nu DN}{|\Omega|}\,. \tag{5.15}$$

For a ring pattern of $N\geq 2$ spots, the Green's matrix $\mathcal{G}$ is cyclic symmetric. As a result, $\mathcal{G}$ shares the same eigenspace with $\mathcal{E}$, and

$$\mathcal{G}\mathbf{e}=\sigma_1\mathbf{e}\,, \quad \sigma_1 = R(\mathbf{x}_1)+\sum_{j\neq 1}^{N} G(\mathbf{x}_1;\mathbf{x}_j)\,; \qquad \mathcal{G}\mathbf{q}_j=\sigma_j\mathbf{q}_j\,, \quad \mathbf{q}_j^T\mathbf{e}=0\,, \quad j=2,\dots,N\,. \tag{5.16}$$

As such, there are two classes of admissible perturbations corresponding to zero-eigenvalue crossings. The first type is the synchronous perturbation $\mathbf{c}=\mathbf{e}$ in (5.15), which leads to the following expression for λ with $|\lambda|\ll 1$:

$$1+\frac{2\pi\nu\tau\lambda}{\mu}\sigma_1 = -\frac{\tau\lambda}{\mu}\left[1+\nu\tilde{B}(S_c,\lambda)\right]\,. \tag{5.17}$$

Recalling that $\tilde{B}(S_c,\lambda)=\chi'(S_c)+\mathcal{O}(\lambda)$ as $\lambda\to 0$, (5.17) shows that there is no zero-eigenvalue crossing for the synchronous mode. Alternatively, let $N\geq 2$ and consider the asynchronous modes $\mathbf{c}=\mathbf{q}_j$, for $j=2,\dots,N$. Then, S_c satisfies

$$\mathbf{q}_j\left[1+2\pi\nu\sigma_j+\nu\chi'(S_c)\right]+\mathcal{O}(\lambda)=0\,, \qquad j=2,\dots,N\,. \tag{5.18}$$

Letting $\lambda \to 0$, we conclude that there exists a zero-eigenvalue crossing for these modes whenever S_c satisfies

$$\chi'(S_c) = -\frac{1}{\nu} - 2\pi\sigma_j\,, \qquad j = 2, \ldots, N\,, \tag{5.19}$$

where σ_j and $\chi(S_c)$ are defined in (5.16) and (2.1), respectively. By using (2.17) for the common spot strength S_c, (5.19) is a nonlinear algebraic equation for the value D_j of the inhibitor diffusivity D at which a zero-eigenvalue crossing occurs. This linear instability threshold is referred to as a competition instability, since with $\mathbf{q}_j^T\mathbf{e} = 0$ for $j = 2, \ldots, N$, it preserves the sum of the amplitudes of the spots.

We now derive a two-term expansion, $D_{j\varepsilon}$, for the thresholds D_j. To do so, we use the small S asymptotics for the constant $\chi(S)$ in the far-field conditions of the core problem (2.1) (see §4.1 of [20])

$$\chi(S_c) \sim \frac{1}{S_c}\hat{\chi}_0 + S_c\hat{\chi}_1 + \ldots\,, \quad \text{as} \quad S_c \to 0\,, \tag{5.20a}$$

where $\hat{\chi}_0$ is an $\mathcal{O}(1)$ constant, defined in terms of the unique ground-state solution $w(\rho) > 0$ by

$$\hat{\chi}_0 \equiv \frac{b(1-f)}{f^2}\,; \qquad b \equiv \int_0^\infty \rho w^2\,d\rho\,; \qquad \Delta_\rho w - w + w^2 = 0\,, \quad w'(0) = 0\,, \quad w \to 0 \quad \text{as} \quad \rho \to 0\,, \tag{5.20b}$$

where $\Delta_\rho \equiv \partial_{\rho\rho} + \rho^{-1}\partial_\rho$. In addition, the next term $\hat{\chi}_1$ is given by

$$\hat{\chi}_1 = \frac{1}{b^2(1-f)}\int_0^\infty \rho u_{1pI}\,d\rho - \frac{1}{b^2}\int_0^\infty \rho u_{1pII}\,d\rho\,, \tag{5.20c}$$

where $u_{1pI}(\rho)$ and $u_{1pII}(\rho)$ are defined uniquely, in terms of $L_0 \equiv \Delta_\rho - 1 + 2w$, by the linear BVPs

$$\begin{gathered} L_0 u_{1pI} = w^3\,, \qquad L_0 u_{1pII} = w^2 v_{1Q}\,, \qquad u_{1pI}\,,\ u_{1pII} \to 0 \quad \text{as} \quad \rho \to \infty\,, \\ \Delta_\rho v_{1Q} = w\,, \qquad v_{1Q} \sim b\log\rho + \mathcal{O}(1) \quad \text{as} \quad \rho \to \infty\,. \end{gathered} \tag{5.20d}$$

By using (5.20a) in (5.19), along with (2.17) for S_c, we obtain the following two-term expansion $D_{j\varepsilon}$ for the critical values D_j, for $j = 2, \ldots, N$, of the inhibitor diffusivity at which a competition instability occurs due to a $\lambda = 0$ crossing:

$$D_{j\varepsilon} = \frac{f^2}{b(1-f)N^2\nu}\left[A + \int_0^1 rE(r)\,dr\right]^2\left[1 + \nu\left(\hat{\chi}_1 + 2\pi\sigma_j\right)\right] + \mathcal{O}(\nu)\,. \tag{5.21}$$

Numerical computations on (5.15) show that the zero-eigenvalue crossings are from the left- to the right-half of the spectral plane as D is increased past D_j. Together with the spot self-replication threshold (5.6), we conclude that the ring pattern of $N \geq 2$ spots in the unit disk is linearly stable on an $\mathcal{O}(1)$ time-scale when τ is sufficiently small and D satisfies

$$D_{\rm split} < D < D_{\rm comp}\,; \qquad D_{\rm comp} \equiv \min_{2\leq j\leq N} D_j\,, \qquad \text{with} \quad D_j \sim D_{j\varepsilon}\,, \tag{5.22}$$

where the two-term expansion $D_{j\varepsilon}$ is defined in (5.21). We remark that since $D_{\rm split} \sim \mathcal{O}(1)$ and $D_{\rm comp} \sim \mathcal{O}(\nu^{-1})$, the interval of stability when τ is small is asymptotically large.

In the analysis above, we have assumed that τ is sufficiently small so that the GCEP (5.7) has no Hopf bifurcations. To analyze the linear stability of a ring pattern of spots to eigenvalue crossings through the positive imaginary axis, we return to the GCEP (5.12). We recall that for a ring pattern, $S_j = S_c$ for $j = 1, \ldots, N$ and $\tilde{\mathcal{B}} = \tilde{B}(S_c, \lambda)\mathcal{I}$. Therefore, upon using the cyclic matrix structure of $\mathcal{G}_\lambda$, we can use the criterion (5.12) to show that the matrix $\mathcal{M}(\lambda) \equiv \mathcal{I} + 2\pi\nu\mathcal{G}_\lambda + \nu\tilde{\mathcal{B}}$ is singular when λ is a root of one of the transcendental equations $\mathcal{F}_j(\lambda) = 0$, defined by

$$\mathcal{F}_j(\lambda) \equiv \omega_{\lambda,j} + \frac{1}{2\pi\nu}\left[1 + \nu\tilde{B}(S_c;\lambda)\right]\,, \qquad j = 1, \ldots, N\,. \tag{5.23}$$

Here, $\omega_{\lambda,j}$, for $j = 1, \ldots, N$, are the eigenvalues of the eigenvalue-dependent Green's matrix $\mathcal{G}_\lambda$ corresponding to eigenvectors $\mathbf{v}_j$, and $\tilde{B}(S_c, \lambda) = \tilde{B}_j$ is computed from (5.7b) and (5.7c) in terms of the solution u_j and v_j to the core problem

(2.1) with $S_j = S_c$. Since $\mathcal{G}_\lambda$ is cyclic symmetric, its matrix spectrum can be expressed in terms of the first row of $\mathcal{G}_\lambda$ (see §6 of [8]), which we label as

$$a_{\lambda,1} = R_\lambda(\mathbf{x}_1)\,, \qquad a_{\lambda,j} = G_\lambda(\mathbf{x}_1;\mathbf{x}_j)\,, \quad j = 2,\dots,N\,. \tag{5.24a}$$

We obtain that the synchronous eigenpair of $\mathcal{G}_\lambda$, labelled by $\omega_{\lambda,1}$ and $\mathbf{v}_1 = (1,\dots,1)^T$, and the remaining $N-1$ eigenvalues $\omega_{\lambda,j}$, $j = 2,\dots,N-1$, corresponding to the asynchronous modes orthogonal to $\mathbf{v}_1$, are

$$\omega_{\lambda,1} = \sum_{n=1}^{N} a_{\lambda,n}\,; \qquad \omega_{\lambda,j} = \sum_{n=0}^{N-1} \cos\left(\frac{2\pi(j-1)\,n}{N}\right) a_{\lambda,n+1}\,, \qquad j = 2,\dots,N\,. \tag{5.24b}$$

Since $\mathcal{G}_\lambda$ is symmetric, we observe that mode degeneracy occurs owing to the fact that $\omega_{\lambda,j} = \omega_{\lambda,N+2-j}$ for $j = 2,\dots,\lceil N/2\rceil$, where the ceiling function $\lceil x\rceil$ is defined as the smallest integer not less than x. When N is even, we notice that there is an eigenvalue of multiplicity one given by $\omega_{\lambda,\frac{N}{2}+1} = \sum_{n=0}^{N-1}(-1)^n a_{\lambda,n+1}$. The corresponding eigenvectors for $j = 2,\dots,\lceil N/2\rceil$ can be written as

$$\begin{aligned}
\mathbf{v}_j &= \left(1, \cos\left(\frac{2\pi(j-1)}{N}\right), \dots, \cos\left(\frac{2\pi(j-1)(N-1)}{N}\right)\right)^T\,,\\
\mathbf{v}_{N+2-j} &= \left(0, \sin\left(\frac{2\pi(j-1)}{N}\right), \dots, \sin\left(\frac{2\pi(j-1)(N-1)}{N}\right)\right)^T\,.
\end{aligned} \tag{5.24c}$$

Finally, when N is even, there is an additional eigenvector given by $\mathbf{v}_{\frac{N}{2}+1} = (1,-1,\dots,-1)^T$.

For the unit disk, the Green's function $G_\lambda(\mathbf{x};\mathbf{x}_0)$ satisfying (5.10) can be written as an infinite sum involving the modified Bessel functions of the first and second kind $I_n(z)$ and $K_n(z)$, respectively, in the form

$$G_\lambda(\mathbf{x};\mathbf{x}_0) = \frac{1}{2\pi}K_0\left(\theta_\lambda|\mathbf{x}-\mathbf{x}_0|\right) - \frac{1}{2\pi}\sum_{n=0}^{\infty}\sigma_n\cos\left(n(\psi-\psi_0)\right)\frac{K_n'(\theta_\lambda)}{I_n'(\theta_\lambda)}I_n\left(\theta_\lambda r\right)I_n\left(\theta_\lambda r_0\right)\,; \quad \sigma_0 = 1\,, \quad \sigma_n = 2\,,\ n \geq 1\,, \tag{5.25a}$$

where $\mathbf{x} = r(\cos\psi,\sin\psi)^T$, $\mathbf{x}_0 = r_0(\cos\psi_0,\sin\psi_0)^T$, and θ_λ is the principal branch of $\theta_\lambda \equiv \sqrt{\tau\lambda/D}$. The corresponding regular part of G_λ, where $\gamma_e = 0.57721\dots$ is Euler's constant, is

$$R_\lambda(\mathbf{x}_0) = \frac{1}{2\pi}\left[\log 2 - \gamma_e + \frac{1}{2}\log\left(D/\tau\right) - \frac{1}{2}\log\lambda\right] - \frac{1}{2\pi}\sum_{n=0}^{\infty}\sigma_n\frac{K_n'(\theta_\lambda)}{I_n'(\theta_\lambda)}\left[I_n\left(\theta_\lambda r_0\right)\right]^2\,. \tag{5.25b}$$

In this way, we can use (5.25) to calculate the eigenvalues $\omega_{\lambda,j}$ in (5.24b) for $j = 1,\dots,N$. We observe that $\omega_{\lambda,j}$ depends only on the ratio $\lambda\tau/D$, N, and the ring radius r_0. To calculate the threshold $\tau_{\rm H}$ at which a pair of eigenvalues $\pm i\lambda_I$ with $\lambda_I > 0$ first crosses the imaginary axis as τ is increased, we fix D on the range (5.22) for which the spot pattern is linearly stable to self-replication and competition instabilities, and numerically solve the system

$$\mathrm{Re}(\mathcal{F}_j(i\lambda_I)) = 0\,, \qquad \mathrm{Im}(\mathcal{F}_j(i\lambda_I)) = 0\,, \qquad j = 1,\dots,N\,, \tag{5.26}$$

for $\lambda_{IHj} > 0$ and τ_{Hj} using Netwon's method. The threshold for the synchronous mode corresponds to τ_{H1} while the thresholds for the asynchronous modes correspond to τ_{Hj}, for $j = 2,\dots,N$. Therefore, it follows that if D satisfies (5.22), the N-spot ring pattern with $N \geq 2$ is linearly stable to $\mathcal{O}(1)$ time-scale oscillatory instabilities when

$$\tau < \tau_{\rm H} \equiv \min_{1\leq j\leq N}\tau_{Hj}\,. \tag{5.27}$$

Numerical solutions for the roots of $\mathcal{F}_j = 0$ in (5.23) show that the eigenvalue crossing is from the left- to the right-half of the spectral plane as τ is increased past τ_{Hj}.

As an illustration of our stability theory, in Fig. 10 and Fig. 11 we plot the Hopf thresholds τ_{Hj} and the corresponding Hopf frequencies λ_{IHj} for a quasi-equilibrium ring pattern of $N = 2$ and $N = 4$ spots, respectively, inside the unit disk. In our computations, we chose the ring radius $r_0 = 0.5$, the Brusselator parameters $\varepsilon = 0.02$ and $f = 0.7$, and we fixed the boundary feed at $A = 2$. We have assumed the spatially uniform bulk feed $E \equiv 1$. As a result, the common spot strength

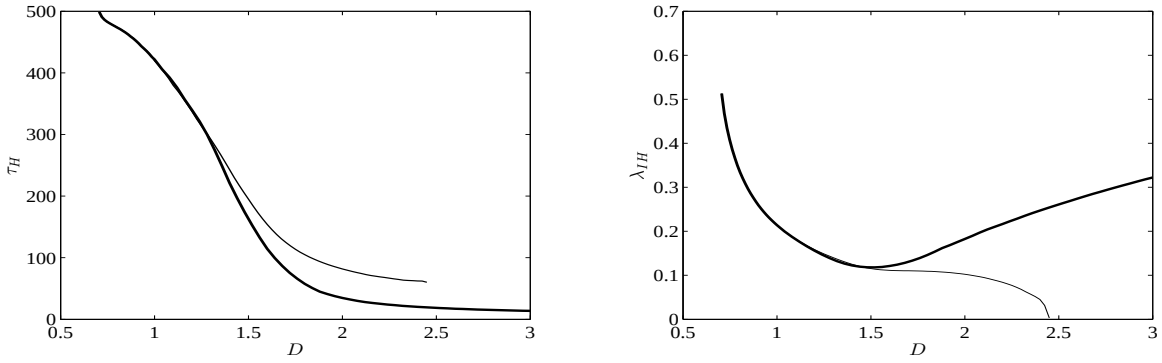

(a) $\tau_{\rm H}$ versus D (b) λ_{IH} versus D

Figure 10: Hopf bifurcation thresholds τ_{Hj} (left panel) and frequency λ_{IHj} (right panel), computed numerically from (5.26), for a quasi-equilibrium pattern of $N = 2$ spots equidistantly spaced on a ring of radius $r_0 = 0.5$ in the unit disk. The Brusselator parameters are $\varepsilon = 0.02$ and $f = 0.7$, the boundary feed is $A = 2$, and we take the spatially uniform bulk feed $E \equiv 1$. Left panel: synchronous threshold is τ_{H1} (heavy solid curve), while the competition threshold τ_{H2} (solid curve) terminates at $D = D_2 \approx 2.4486$. Right panel: λ_{IH1} (heavy solid curve) and λ_{IH2} (solid curve). Notice that $\lambda_{IH2} \to 0^+$ as $D \to D_2^-$.

from (2.17) with $A = 2$, $|\Omega| = \pi$, and $|\partial\Omega| = 2\pi$, yields $S_c = (2A+1)/(2\sqrt{D}N)$. The spot self-replication threshold is $S_c = \Sigma_2(0.7) \approx 3.23$ (see Fig. 2), so that from (5.6) we calculate $D_{\rm split} \approx 0.1498$ for $N = 2$ and $D_{\rm split} \approx 0.03744$ for $N = 4$. We observe from the left panels of Fig. 10 and Fig. 11 that, for most values of D, it is the synchronous mode $j = 1$ which sets the Hopf bifurcation threshold in (5.27). In the left panel of Fig. 11 we observe that there are only two distinct, rather than three, values of τ_{Hj} for the competition modes $j = 2, \ldots, 4$, owing to the mode degeneracy of the matrix spectra of $\mathcal{G}_\lambda$ as was discussed above. By comparing these plots with those in the right panels of Fig. 10 and Fig. 11, we observe that the curves τ_{Hj} versus D for the competition modes $j = 2, \ldots, 4$ terminate at the competition threshold D_j of D for which $\lambda_{IHj} = 0$. By solving (5.19) numerically, we find for $N = 2$ that $D_2 = 2.4486$, so that the interval in (5.22) yields $0.1498 < D < 2.4486$. For the case $N = 4$, we solve (5.19) to get $D_2 = D_4 \approx 0.6121$ and $D_3 \approx 0.4484$, so that the interval in (5.22) yields $0.03744 < D < 0.4484$. However, for $D > D_{\rm comp}$, the pattern is always unstable for any $\tau \geq 0$ as a result of a positive real eigenvalue. For this range of D, when τ exceeds the threshold τ_{H1} for the synchronous mode, further complex conjugate unstable eigenvalues enter the unstable half-plane $\mathrm{Re}(\lambda) > 0$.

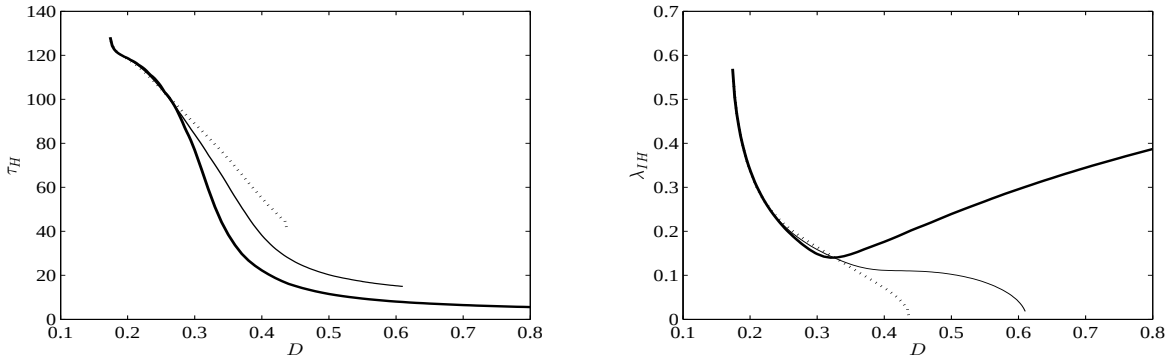

(a) $\tau_{\rm H}$ versus D (b) λ_{IH} versus D

Figure 11: Hopf bifurcation thresholds τ_{Hj} (left panel) and frequency λ_{IHj} (right panel), computed numerically from (5.26), for a quasi-equilibrium pattern of $N = 4$ spots equidistantly spaced on a ring of radius $r_0 = 0.5$ in the unit disk. The Brusselator and feed parameters are the same as in the caption of Fig. 10. Left panel: synchronous threshold is τ_{H1} (heavy solid curve). The competition thresholds $\tau_{H2} = \tau_{H4}$ (solid curve) and τ_{H3} (dotted curve) terminate at $D = D_2 \approx 0.6121$ and $D = D_3 \approx 0.4484$, respectively. Right panel: λ_{IH1} (heavy solid curve) and λ_{IH2} (solid curve) and λ_{IH3} (dotted curve). We observe that $\lambda_{IH2} \to 0^+$ and $\lambda_{IH3} \to 0^+$ as $D \to D_2^-$ and $D \to D_3^-$.

Finally, we validate our theoretical stability predictions for the parameter values chosen in Fig. 10 for the two-spot ring pattern. In Fig. 12 we show FlexPDE [7] generated numerical solutions for the amplitudes of the two spots versus time for two values of D, and for values of τ either slightly below or slightly above our theoretically predicted Hopf bifurcation thresholds (see the caption of Fig. 12 for details). In our full numerical simulations of the Brusselator (1.2a)-(1.2b), we took as an initial condition a two-spot quasi-equilibrium ring pattern, with a slight initial perturbation of the spot amplitudes. These numerical results confirm our predictions of the Hopf bifurcation thresholds, and show that, depending on the value of D, either synchronous or asynchronous unstable small-scale oscillations can emerge when t is small. However, in either case, in the middle and right panel of Fig. 12, these oscillations are shown to trigger a nonlinear event leading to the annihilation of one of the two spots.

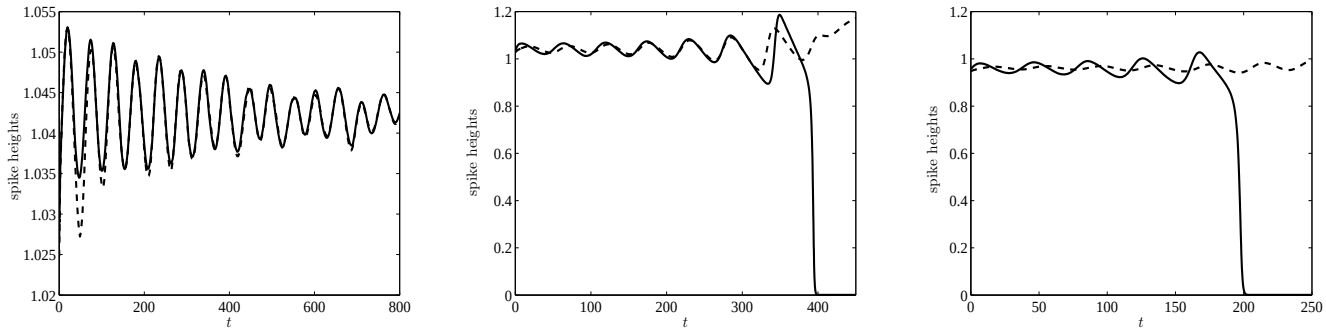

(a) $D = 1.5$, $\tau = 150$ (b) $D = 1.5$, $\tau = 170$ (c) $D = 1.1$, $\tau = 382$

Figure 12: Spot amplitudes versus time, computed from FlexPDE [7], for the two-spot quasi-equilibrium ring pattern of Fig. 10. Left panel: $D = 1.5$ and $\tau = 150$. Decaying oscillations occur since $\tau < \tau_{H1} \approx 163.2$ and $\tau < \tau_{H2} \approx 194.9$, as obtained from the left panel of Fig. 10. Middle panel: $D = 1.5$ and $\tau = 170$, so that $\tau_{H1} < \tau < \tau_{H2}$. Unstable small-scale oscillations become synchronized initially, triggering a nonlinear event leading to spot annihilation. Right panel: $D = 1.1$ and $\tau = 382$. The data from the left panel of Fig. 10 yields $\tau_{H2} \approx 379.6$ and $\tau_{H1} \approx 384.3$. Since $\tau_{H2} < \tau < \tau_{H1}$, unstable small-scale asynchronous oscillations occur, before a spot is ultimately annihilated.

5.2 Case II: Robin boundary condition with constant E

For Case II, with Robin boundary conditions, the analysis of the splitting instability proceeds as in the Neumann case above. That is, the j-th spot with strength S_j will lose stability to a peanut-splitting mode when $S_j > \Sigma_2(f)$, which numerically is found to lead to a nonlinear self-replication event. The splitting threshold $\Sigma_2(f)$ is the same as that for the Neumann case, but the strength S_j is now given by the solution of the nonlinear algebraic equation (2.23). In Fig. 13 we illustrate an intrinsically triggered splitting instability as a two-spot ring solution evolves toward its steady-state radius. This dynamic triggering is possible in the Robin case because the common spot strength S_c in (2.29) depends on the ring radius r_0 through the function $v_3(r)$ in (2.25). In Fig. 13(a), where $f = 0.7$, we plot r_0 versus slow time σ (heavy curve, left axis) according to the DAE (2.29) and (4.26). On the right axis, we plot the corresponding evolution of S_c (light curve). The dashed segments indicate the time past which $S_c > \Sigma_2(0.7) \approx 3.23$, which occurs when $r_0 \approx 0.582$. Starting with $r_0 = 0.4$ (Fig. 13(b)), a simultaneous splitting event is initiated in both spots as r_0 increases past this critical radius (Fig. 13(c)). The direction of splitting is found to be orthogonal to the direction of motion of each particular spot (see [13] for an analysis of this for a closed system). After the spots split, the resulting four-spot ring pattern evolves to its stationary state (Fig. 13(d)). Note that in Fig. 13(a), the numerically computed ring radius (open circles) agrees well with the asymptotic curve until the splitting event is initiated, and the divergence between asymptotics and numerics begins only when the pattern is predicted to lose stability. A similar intrinsic triggering is not possible for a ring pattern for Case I since the common spot strength (2.17) for Case I is independent of the ring radius. For Case I we showed that the triggering of spot self-replication can be achieved by increasing either the boundary flux or the bulk feed.

The derivation of the GCEP characterizing the linear stability to radially symmetric perturbations is also similar. By introducing the perturbation (5.1) and (5.7a), we get the same inner problem (5.7). In the outer region, we obtain (5.8a)

for η, but where the Robin condition $\partial_n \eta + \kappa_0 \eta = 0$ on $\partial\Omega$ must hold. In this way, the solution for η is

$$\eta = -\frac{2\pi}{D} \sum_{i=1}^{N} c_i G_{\kappa\lambda}(\mathbf{x}; \mathbf{x}_i)\,, \tag{5.28}$$

where $G_{\kappa\lambda}(\mathbf{x}; \mathbf{x}_0)$ is the eigenvalue-dependent Robin Green's function satisfying

$$\begin{gathered} \Delta G_{\kappa\lambda} - \frac{\tau\lambda}{D} G_{\kappa\lambda} = -\delta(\mathbf{x} - \mathbf{x}_0)\,, \quad \mathbf{x} \in \Omega\,, \qquad \partial_n G_{\kappa\lambda} + \kappa_0 G_{\kappa\lambda} = 0\,, \quad \mathbf{x} \in \partial\Omega\,; \\ G_{\kappa\lambda} \sim -\frac{1}{2\pi} \log|\mathbf{x} - \mathbf{x}_0| + R_{\kappa\lambda 0} + \mathcal{O}(1) \quad \text{as} \quad \mathbf{x} \to \mathbf{x}_0\,. \end{gathered} \tag{5.29}$$

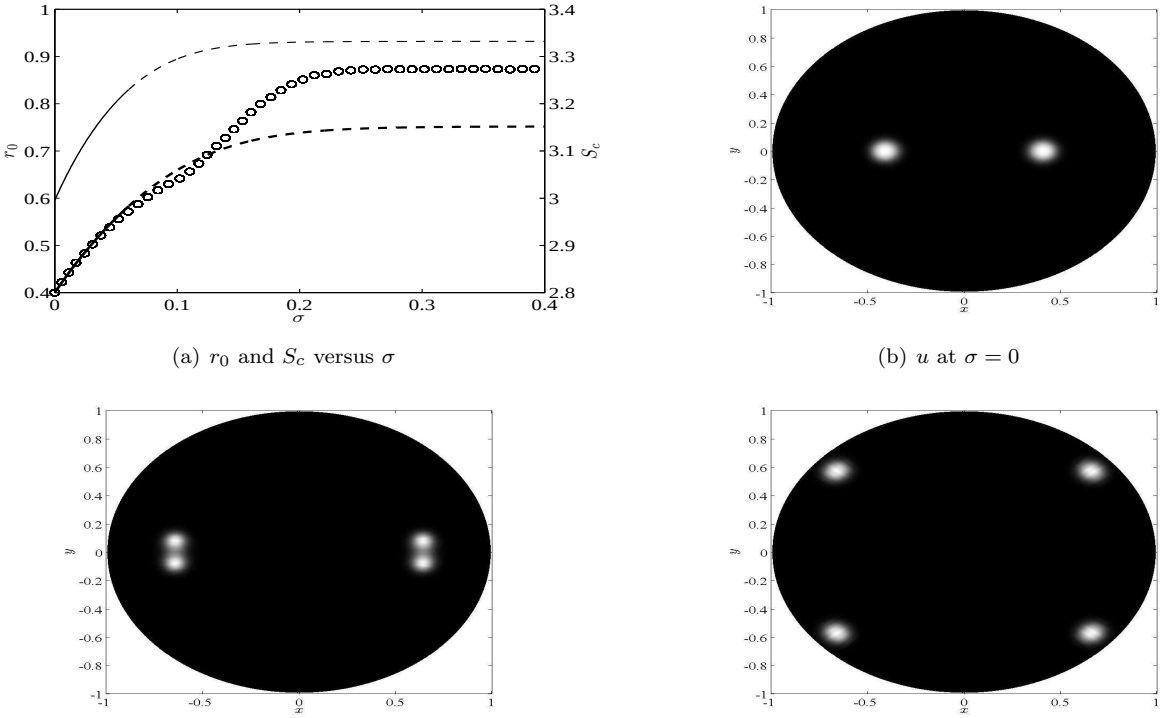

(a) r_0 and S_c versus σ

(b) u at $\sigma = 0$

(c) u at $\sigma \approx 0.105$

(d) u at $\sigma \approx 0.4$

Figure 13: Top left panel: plot of the asymptotically computed ring radius r_0 (heavy curve, left axis) and common spot strength S_c (light curve, right axis) for a two-spot ring pattern. The solid (dashed) segments of both curves indicate when the pattern is linearly stable (unstable) to a peanut-splitting instability. The open circles are numerical values of the ring radius obtained from the solution of the full PDE (1.2). Agreement is observed to cease when the pattern is predicted to become unstable. Top right panel: two spots placed symmetrically at $(\pm 0.4, 0)$. Light (dark) regions indicate large (small) values of u. Bottom left panel: plot of u near completion of the self-replication process. Notice that the locations of the two spots have evolved to near $(\pm 0.6, 0)$, close to the asymptotically predicted stability threshold of $(\pm 0.582, 0)$. Bottom right panel: well after the splitting event, the resulting four-spot ring pattern evolves to its steady-state solution. The parameters are $f = 0.7$, $D = 2.4$, $\tau = 0.05$, $\kappa = 7.3$, and $v_b = 9.3$.

Repeating the analysis leading to (5.12), we obtain that the eigenvalues λ and eigenmodes $\mathbf{c} = (c_1, \ldots, c_N)^T$ corresponding to radially symmetric perturbations satisfy

$$\det \mathcal{M}_\kappa(\lambda) = 0\,, \qquad \mathcal{M}_\kappa \mathbf{c} = \mathbf{0}\,; \qquad M_\kappa(\lambda) \equiv \mathcal{I} + 2\pi\nu \mathcal{G}_{\kappa\lambda} + \nu\tilde{\mathcal{B}}\,, \tag{5.30a}$$

where $\tilde{\mathcal{B}}$ is defined in (5.12b) and the entries of the Green's matrix $\mathcal{G}_{\kappa\lambda}$ are given by

$$(\mathcal{G}_{\kappa\lambda})_{ij} \equiv \begin{cases} R_{\kappa\lambda j} & i = j \\ G_{\kappa\lambda}(\mathbf{x}_i; \mathbf{x}_j) & i \neq j \end{cases}. \tag{5.30b}$$

For a ring pattern of spots, we have that $\tilde{\mathcal{B}} = \tilde{B}(S_c, \lambda)\mathcal{I}$, where the common spot strength S_c satisfies (2.29). Moreover, the condition $\det \mathcal{M}_\kappa(\lambda) = 0$ reduces to the transcendental equations $\mathcal{F}_{\kappa j}(\lambda) = 0$, for $j = 1, \ldots, N$, where

$$\mathcal{F}_{\kappa j}(\lambda) \equiv \omega_{\kappa\lambda j} + \frac{1}{2\pi\nu}\left[1 + \nu\tilde{B}(S_c;\lambda)\right]. \tag{5.31}$$

Here, $\omega_{\kappa\lambda j}$ for $j = 1, \ldots, N$ are the eigenvalues of the cyclic symmetric Green's matrix $\mathcal{G}_{\kappa\lambda}$, which have analogous explicit expressions as in (5.24b). In addition, as in (2.26a), $G_{\kappa\lambda}$ can be computed in terms of an infinite series as

$$G_{\kappa\lambda}(\mathbf{x};\mathbf{x}_0) = \frac{1}{2\pi}K_0(\theta_\lambda|\mathbf{x}-\mathbf{x}_0|) + \frac{1}{2\pi}\left(c_0 I_0(\theta_\lambda r) + \sum_{n=1}^{\infty} c_n I_n(\theta_\lambda r)\cos(n(\psi-\psi_0))\right); \qquad \theta_\lambda \equiv \sqrt{\frac{\tau\lambda}{D}}, \tag{5.32a}$$

where $\mathbf{x} = r(\cos\psi, \sin\psi)^T$, $\mathbf{x}_0 = r_0(\cos\psi_0, \sin\psi_0)^T$, $I_n(z)$ and $K_n(z)$ are modified Bessel functions of the first and second kind, and the principal branch for θ_λ is specified. In (5.32a), the coefficients c_0 and c_n are given by

$$\begin{aligned} c_0 &= \frac{\theta_\lambda K_1(\theta_\lambda)I_0(\theta_\lambda r_0) - \kappa_0 K_0(\theta_\lambda)I_0(\theta_\lambda r_0)}{\theta_\lambda I_1(\theta_\lambda) + \kappa_0 I_0(\theta_\lambda)}, \\ c_n &= \frac{2\theta_\lambda I_n(\theta_\lambda r_0)\left[K_{n+1}(\theta_\lambda) - \frac{n}{\theta_\lambda}K_n(\theta_\lambda)\right] - 2\kappa_0 K_n(\theta_\lambda)I_n(\theta_\lambda r_0)}{\theta_\lambda\left[I_{n+1}(\theta_\lambda) + \frac{n}{\theta_\lambda}I_n(\theta_\lambda)\right] + \kappa_0 I_n(\theta_\lambda)}, \qquad n = 1, 2, \ldots. \end{aligned} \tag{5.32b}$$

We remark that, in contrast to the Neumann case, $\mathcal{G}_{\kappa\lambda}$ is defined at $\lambda = 0$. As such, (5.31) can be used to study the Hopf bifurcation as well as the zero-eigenvalue crossings associated with the competition instability.

The Hopf threshold can be calculated as in (5.26)-(5.27) with $\mathcal{F}_j$ replaced by $\mathcal{F}_{\kappa j}$. To calculate the competition threshold, we note that when $\lambda = 0$ we have $G_{\kappa\lambda} \to G_\kappa$ and $\tilde{B}(S_c; 0) = \chi'(S_c)$. In this way, and in terms of the eigenvalues $\sigma_{\kappa,j}$ of the Robin Green's matrix $\mathcal{G}_\kappa$, it follows that zero-eigenvalue crossings occur whenever

$$\sigma_{\kappa,j} + \frac{1}{2\pi\nu} + \frac{1}{2\pi}\chi'(S_c) = 0, \qquad j = 1, \ldots, N. \tag{5.33}$$

5.2.1 Leading-order theory for spots: existence and stability with a Robin condition

To all orders in ν, the existence threshold for a ring pattern and the corresponding linear stability threshold can be calculated from (2.29) and (5.33). However, to more readily illustrate the novel solution behavior, we will determine leading-order-in-ν approximations of both the stability threshold and the existence threshold from (2.29) and (5.33). We will assume below that $\tau \ll 1$ so that we need only consider peanut-splitting instabilities or competition instabilities from zero-eigenvalue crossings. We will examine three distinguished scaling regimes where different solution behavior occurs.

The first scaling regime $D \sim \mathcal{O}(\nu^{-1})$ and $\kappa \sim \mathcal{O}(\nu^{-1})$, so that $\kappa_0 \equiv \kappa/D \sim \mathcal{O}(1)$, is where a competition instability can occur. In this regime, assuming $S_c \ll 1$ and using (5.20a) in (2.29), we must have $S_c \sim \mathcal{O}(\nu^{1/2})$ so that

$$D = D_0/\nu, \qquad S_c = S_{c0}\nu^{1/2}, \qquad \kappa \sim \mathcal{O}(1/\nu). \tag{5.34}$$

Upon substituting (5.34) in (2.29), and together with the leading-order small S_c asymptotics for $\chi(S_c)$ in (5.20a), we obtain that $S_{c0} + \hat{\chi}_0/S_{c0} \sim D_0 v_b$, which yields

$$S_{c0} = \frac{D_0 v_b \pm \sqrt{D_0^2 v_b^2 - 4\hat{\chi}_0}}{2}, \qquad \text{provided that} \qquad D_0 > \frac{2\sqrt{\hat{\chi}_0}}{v_b}, \tag{5.35}$$

where $\hat{\chi}_0$ is defined in (5.20b). From (5.35), we observe that there exists a saddle-node bifurcation point for the quasi-equilibrium ring pattern. That is, to leading order in ν in the scaling regime (5.34), the ring pattern does not exist when

$$D < D_E^{(1)} \equiv \frac{D_{0E}^{(1)}}{\nu}, \qquad \text{where} \qquad D_{0E}^{(1)} \equiv \frac{2\sqrt{b(1-f)}}{f v_b}, \tag{5.36}$$

and b is defined in (5.20b). We observe that this leading-order existence threshold is independent of N and the ring radius. For a fixed D_0, this saddle-node behavior and non-existence of a ring pattern as the external concentration v_b in

(1.2b) decreases below a threshold is qualitatively similar to that computed in Fig. 9(a) for a one-spot pattern from the nonlinear constraint (2.29).

Next, for the parameter regime (5.34), we examine the leading-order stability thresholds corresponding to zero-eigenvalue crossings. Using $\chi(S_c) \sim \hat{\chi}_0/S_c$ for $S_c \ll 1$, we obtain that (5.33) reduces to

$$\sigma_{\kappa,j} + \frac{1}{2\pi\nu} + \frac{1}{2\pi}\left(-\frac{\hat{\chi}_0}{S_c^2} + \dots\right) = 0\,. \tag{5.37}$$

Since $S_c = S_{c0}\nu^{1/2}$, we match the $\mathcal{O}(\nu^{-1})$ terms in (5.37) to conclude that the zero-eigenvalue crossings occur when $S_{c0} = \sqrt{\hat{\chi}_0}$. Setting $S_{c0} = \sqrt{\hat{\chi}_0}$ in (5.35), it follows that, to leading order in ν, the exchange of stability occurs at the existence threshold. That is, to leading order in ν, the synchronous mode $j = 1$ and all asynchronous modes $j = 2, \dots, N$ cross the origin of the spectral plane simultaneously as S_{c0} is varied across past the saddle-node point $\sqrt{\hat{\chi}_0}$. We remark that since $\sigma_{\kappa,j} \sim \mathcal{O}(1)$ in (5.37), the stability threshold is, to leading order in ν, independent of κ_0, N, and the ring radius. Also, since $S_c \sim \mathcal{O}(\nu^{1/2}) < \Sigma_2(f)$, no peanut-splitting instabilities are possible in the scaling regime of (5.34).

The second distinguished scaling regime is

$$D = D_0\nu\,, \qquad S_c = S_{c0}\nu^{1/2}\,, \qquad \kappa \sim \mathcal{O}(\nu)\,, \tag{5.38}$$

so that $\kappa_0 = \kappa/D = \mathcal{O}(1)$. We substitute $\chi(S_c) \sim \hat{\chi}_0/S_c$ for $S_c \ll 1$ into (2.29) to obtain to leading order in ν that $S_{c0} + \hat{\chi}_0/S_{c0} = v_3(r_0)/\sqrt{D_0}$, where $v_3(r_0)$ is given in (2.25). This yields that

$$S_{c0} = \frac{v_3(r_0)}{2\sqrt{D_0}} \pm \sqrt{\frac{[v_3(r_0)]^2}{4D_0} - \hat{\chi}_0}\,, \qquad \text{provided that} \qquad D_0 < \frac{[v_3(r_0)]^2}{4\hat{\chi}_0}\,. \tag{5.39}$$

Upon using (2.25) for $v_3(r_0)$ and (5.20b) for $\hat{\chi}_0$, we obtain in the scaling regime (5.38) that there is no ring pattern of radius r_0 when

$$D > D_E^{(2)} \equiv \nu D_{0E}^{(2)}\,, \qquad \text{where} \qquad D_{0E}^{(2)} \equiv \frac{f^2}{4b(1-f)}\left[\frac{(1-r_0^2)}{4} + \frac{1}{2\kappa_0}\right]^2\,. \tag{5.40}$$

Furthermore, it is readily seen that, to leading order in ν, all zero-eigenvalue crossings of the GCEP in this scaling regime again occur at the saddle-node point $\nu D_{0E}^{(2)}$.

Moreover, when $\kappa_0 = \mathcal{O}(1)$, we readily observe that, to leading-order in ν, the nonlinear constraint (2.29) has no solution when $D = \mathcal{O}(1)$. With this observation, and from our leading-order-in-ν theory, it follows that when $\kappa_0 = \mathcal{O}(1)$ there is no quasi-equilibrium solution when D lies in the asymptotically wide interval

$$D_E^{(2)} < D < D_E^{(1)}\,, \tag{5.41}$$

where the saddle-node bifurcation points $D_E^{(1)}$ and $D_E^{(2)}$ are defined in (5.36) and (5.40), respectively. In Fig. 14(a), we show a typical bifurcation diagram for the solution of (2.29) as a function of D, while fixing the ratio $\kappa_0 = \kappa/D$ at an $\mathcal{O}(1)$ value. In this figure the solid curves represent solutions that are linearly stable on an $\mathcal{O}(1)$ time-scale when $\tau \ll 1$. The dotted portions represent solutions unstable to peanut-splitting, whereas the dashed portions represent solutions unstable to competition instabilities. As predicted theoretically, no solution exists in a certain wide interval of D. To generate our result for competition instabilities, we numerically computed the root of (5.31) with the largest real part. In computing the eigenvalues $\omega_{\kappa\lambda j}$ of $\mathcal{G}_{\kappa\lambda}$ in (5.30b), we have used $\tau = 0.007$ in (5.29). In Figs. 14(b) and 14(c), we illustrate how the upper ($D_E^{(1)}$) and lower ($D_E^{(2)}$) existence thresholds vary as a function of $\nu \ll 1$. When ν is sufficiently small, we observe excellent agreement between the numerical (open circles) and asymptotically predicted values (solid) given in (5.36) and (5.40). In Fig. 14(d) we plot the maximum eigenvalue at the right saddle-node point $D = D_E^{(1)}$, as computed from (5.31). Our computations show that $\max(\lambda) \to 0$ as $\nu \to 0$, confirming the leading-order asymptotic theory that the the exchange of stability does indeed occur for $\nu \ll 1$ at the saddle-node point.

The last scaling regime of (2.29) is where $\kappa_0 \sim \mathcal{O}(\nu) \ll 1$ with $D = \mathcal{O}(1)$, so that $\kappa = D\kappa_0 \sim \mathcal{O}(\nu)$. This regime is asymptotically close to the pure Neumann case where $\partial_n v = 0$ on $\partial\Omega$. For a ring pattern in this scaling regime, we let $\kappa_0 = \nu\kappa_{00}$, and obtain from (2.25) that $v_3(r_0) \sim \nu^{-1}/(2\kappa_{00}) + \mathcal{O}(1)$. Moreover, upon using (B.7) for the Robin Green's

matrix when $\kappa_0 \ll 1$, we obtain that $\sigma_{\kappa,1} \sim N/(\kappa_0|\partial\Omega|)$ for $\kappa_0 \ll 1$. Upon substituting these results into (2.29), and using $|\partial\Omega| = 2\pi$, we obtain to leading order in ν that $S_c = \mathcal{O}(1)$ satisfies $S_c\,(1 + N/\kappa_{00}) \sim \left[2\kappa_{00}\sqrt{D}\right]^{-1}$, which yields that

$$S_c \sim \frac{1}{2\sqrt{D}\,(\kappa_{00} + N)}\,. \tag{5.42}$$

As expected, in this scaling regime, we recover the Neumann result (2.17) with $A = 0$ when we set $\kappa_{00} = 0$ in (5.42). The only $\mathcal{O}(1)$ instability in this regime is the self-replication instability that is triggered when S_c exceeds $\Sigma_2(f)$.

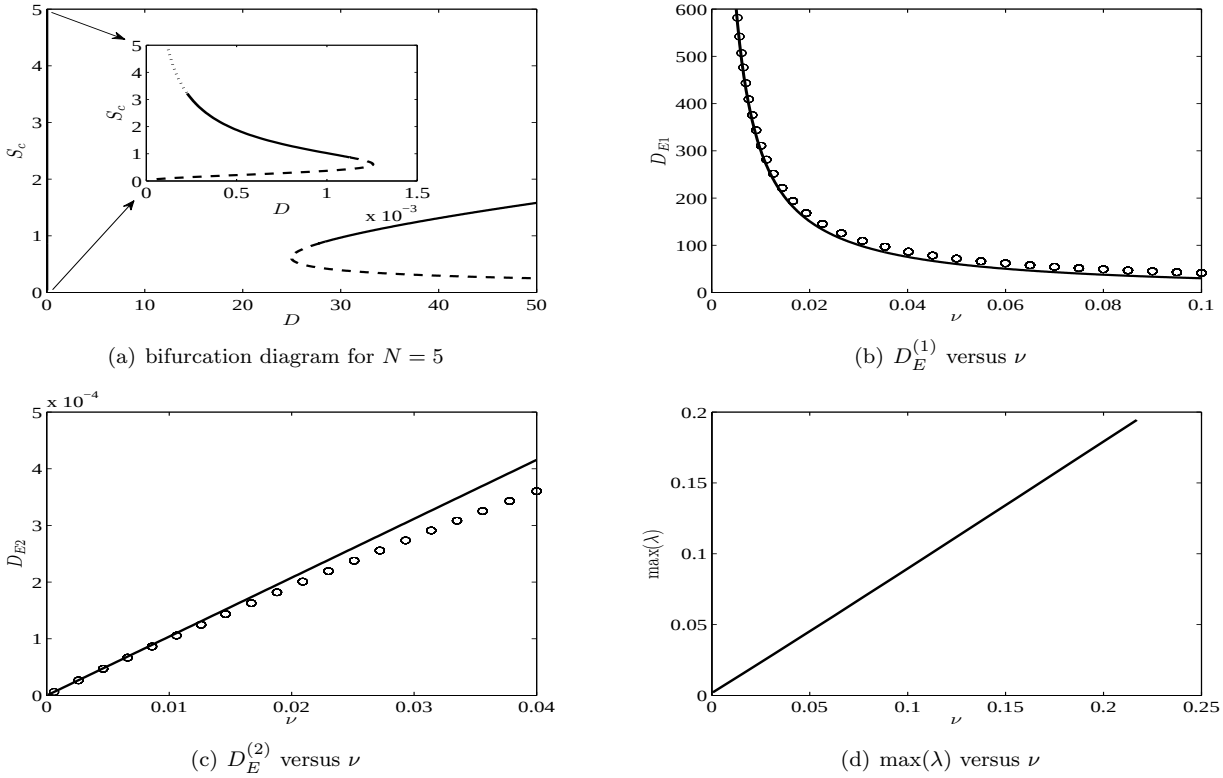

(a) bifurcation diagram for $N = 5$

(b) $D_E^{(1)}$ versus ν

(c) $D_E^{(2)}$ versus ν

(d) max(λ) versus ν

Figure 14: Top left panel: numerical solution of the common spot strength S_c (2.29) versus D for a ring pattern with $f = 0.7$, $r_0 = 0.5$, $\kappa_0 = 3$, $v_b = 2$, $\varepsilon = 0.01$, and $N = 5$. The solid portions of the curves represent solutions linearly stable on an $\mathcal{O}(1)$ time-scale, while the dotted and dashed portions represent solutions unstable to peanut-splitting and competition instabilities, respectively. The inset is a blow-up of the interval $0 < D < 1.5 \times 10^{-3}$. No solution exists in the interval $D \in (1.255 \times 10^{-3}, 24.984)$. Top right panel: the upper existence threshold $D = D_E^{(1)}$ versus ν as computed numerically (open circles) and given asymptotically (solid) by (5.36). Bottom left panel: the same comparison for the lower existence threshold $D = D_E^{(2)}$, where the asymptotic result is given in (5.40). In both top right and bottom left panels, the agreement improves when ν is small. Bottom right panel: plot of the maximum eigenvalue at the right saddle-node point as computed from (5.31) versus ν. As $\nu \to 0$, the saddle-node point is where the competition instability occurs.

6 Discussion

We have analyzed the effect of either a flux-type or Robin-type boundary condition, as given in (1.2b), on the existence, linear stability, and slow dynamics of 2-D localized spot patterns for the singularly perturbed Brusselator model (1.2a). Previous analyses of localized spot patterns (cf. [3, 13, 20, 22, 28–32, 36]) have focused on "closed" systems, whereby homogeneous Neumann conditions are imposed on the domain boundary. In our analysis we also considered the effect of a spatially inhomogeneous feed $E = E(\mathbf{x})$ in (1.2a). Although our analysis pertains to arbitrary spot configurations in general bounded 2-D domains, for analytical tractability we have only illustrated our theory for the case of one-spot or

ring-type patterns of spots within the unit disk. For these patterns, and under Case I flux-type boundary conditions, we studied spot-pinning behavior induced by the boundary flux and a spatially variable bulk feed $E(\mathbf{x})$. The main feature associated with the Case II Robin condition is that a one-spot solution centered at the origin of the disk can become unstable as the Robin constant increases, leading to a new steady-state location nearer to the domain boundary. Moreover, quasi-equilibrium ring patterns with $N \geq 2$ can exhibit saddle-node bifurcation behavior in terms of either the inhibitor diffusivity D (see Fig. 14), the Robin constant κ_0 in (1.2b) (see Fig. 7), or the ambient background concentration v_b in (1.2b) (see Fig. 9). Our asymptotic results for the existence, linear stability, and slow dynamics of spots have been favorably compared with full numerical simulations of the Brusselator model (1.2a) with (1.2b) using FlexPDE [7].

As a continuation of this study it would be interesting to extend the implementation of our asymptotic theory to arbitrary 2-D domains, with either a flux-type or Robin condition on the domain boundary, and to allow for an arbitrary spatial dependence of the bulk feed $E = E(\mathbf{x})$. To accomplish this, one would need to develop fast multipole methods, analogous to those in [9], to calculate either the Neumann or Robin Green's function, and their regular parts, in arbitrary 2-D domains. This combined analytic-numerical approach would allow for a more general investigation of the role of the boundary conditions and the bulk feed on both spot-pinning behavior and the bifurcation behavior of steady-state spot patterns. It would also be interesting to analyze spot patterns with standard no-flux conditions on the outer boundary, but allow for singular perturbations of the domain shape, which can model either defects or obstacles in the domain. An example of such a perturbation would be to introduce a small hole in the domain of radius $\mu = \mathcal{O}(\varepsilon) \ll 1$, while imposing a homogeneous Dirichlet condition for both the activator and inhibitor on the boundary of the hole. With such a perturbation, material can leak out of the domain, and we expect that bifurcation properties of quasi-equilibrium spot patterns for the Brusselator will exhibit a novel saddle-node structure.

Finally, although we considered two classes of open systems only in the context of the 2-D Brusselator model, a very similar hybrid asymptotic-numerical approach can be used to study the effect of open systems on spot patterns for other well-known singularly perturbed RD systems, such as the Gierer-Meinhardt, Gray-Scott, and Schnakenberg models.

A Derivation of the effective strength of the localized source

In this appendix, we give the brief derivation for the $\mathcal{O}(\varepsilon^2\eta^{-1})$ correction term to $\tilde{a}_1$ in (4.19) that is needed as a result of using a regularized Delta function F to model the concentrated bulk feed in the full numerical computations. Using (4.18) for $E_\eta(\mathbf{x})$ in (1.2a), we have that $u \sim \varepsilon^2(a_0 + a_1 F)$ in the outer region. Then, by using this outer approximation for u in the $\varepsilon^{-2}(u - vu^2)$ term in the equation of (1.2a) for the inhibitor v, we calculate

$$\varepsilon^{-2}(u - vu^2) \sim a_0 - \varepsilon^2 a_0^2 v + \left(a_1 - 2\varepsilon^2 a_0 a_1 v\right) F - \varepsilon^2 a_1^2 v F^2 \,. \tag{A.1}$$

We then approximate the localized terms proportional to F and F^2 as weighted delta sources concentrated at $\mathbf{x} = \boldsymbol{\xi}$. Since $\int_\Omega F \, d\mathbf{x} = 1$ while $\int_\Omega F^2 \, d\mathbf{x} = (2\pi\eta)^{-1}$, it follows from (A.1) that for $\eta \ll 1$,

$$\varepsilon^{-2}(u - vu^2) \sim a_0 + \left(a_1 - \frac{a_1^2\varepsilon^2}{2\pi\eta} v(\boldsymbol{\xi}, \sigma)\right) \delta(\mathbf{x} - \boldsymbol{\xi}) + \mathcal{O}(\varepsilon^2) \,. \tag{A.2}$$

Therefore, we define the effective strength $\tilde{a}_1$ of the delta source as

$$\tilde{a}_1 \equiv a_1 - \frac{\varepsilon^2 a_1^2}{2\pi\eta} v(\boldsymbol{\xi}, \sigma) \,. \tag{A.3}$$

For the asymptotic theory to hold, we require $0 < \varepsilon^2/\eta \ll 1$. The quantity $v(\boldsymbol{\xi}, \sigma)$ in (A.3) must be obtained from the numerical solution of (1.2a) with E given by (4.18). In Fig. 15, we give the comparison between asymptotic and numerical results for the distance between the spot and the point of concentration of the fuel when a_1 is used instead of the effective strength $\tilde{a_1}$ in the expression for S_1 in the ODE dynamics (4.22). With this modification, we observe a poorer agreement between the asymptotic theory and full numerical results for slow spot dynamics than that shown in Fig. 6(b).

B Case II Quasi-equilibria and slow dynamics: Small κ_0 asymptotics

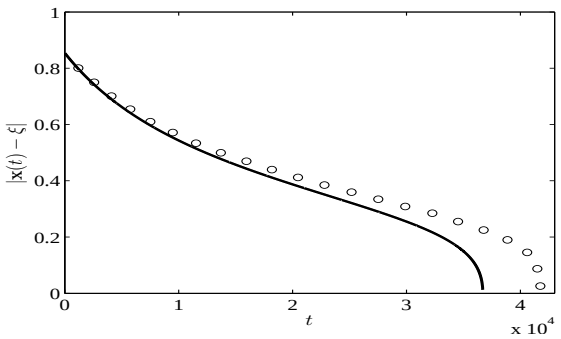

Figure 15: The same comparison as that given in Fig. 6(b), except for S_1 in (4.22), we use a_1 instead of $\tilde{a_1}$ given in (A.3). The agreement between the asymptotic and full numerical results is poorer than that shown in Fig. 6(b) for which the effective strength was used.

We show that the $\kappa_0 \to 0$ limit of the DAE system (2.23) with (3.10) for the spot strengths and locations reduces to the results of the closed system, corresponding to Case I with $A = 0$ and $E \equiv 1$. To do so, we first approximate the Robin Green's function G_κ in (2.19) for $\kappa_0 \to 0$. Applying the divergence theorem to (2.19), we obtain the identity $\int_{\partial\Omega} G_\kappa(\mathbf{x};\mathbf{x}_0)\, d\mathbf{x} = \kappa_0^{-1}$, which suggests that $G_\kappa \sim \kappa_0^{-1} G_0 + G^\star + \cdots$. The leading-order problem yields that G_0 is constant, and so the integral identity above yields $G_0 \equiv |\partial\Omega|^{-1}$. At the next order, we find that $G^\star$ satisfies

$$\Delta G^\star = -\delta(\mathbf{x}-\mathbf{x}_0)\,, \quad \mathbf{x}\in\Omega\,; \qquad \partial_n G^\star = -\frac{1}{|\partial\Omega|}\,, \quad \mathbf{x}\in\partial\Omega\,; \qquad \int_{\partial\Omega} G^\star\, d\mathbf{x} = 0\,. \tag{B.1}$$

We then decompose $G^\star(\mathbf{x};\mathbf{x}_0) = -\hat{G}(\mathbf{x}) + G_N(\mathbf{x};\mathbf{x}_0)$, where $G_N(\mathbf{x};\mathbf{x}_0)$ is a Neumann Green's function, but with a non-standard integral constraint, defined by

$$\begin{aligned} &\Delta G_N = \frac{1}{|\Omega|} - \delta(\mathbf{x}-\mathbf{x}_0)\,, \quad \mathbf{x}\in\Omega\,, \qquad \partial_n G_N = 0\,, \quad \mathbf{x}\in\partial\Omega\,; \\ &\int_{\partial\Omega} G_N\, d\mathbf{x} = 0\,, \qquad G_N \sim -\frac{1}{2\pi}\log|\mathbf{x}-\mathbf{x}_0| + R_{N0} + \mathcal{O}(1) \quad \text{as} \quad \mathbf{x}\to\mathbf{x}_0\,, \end{aligned} \tag{B.2}$$

and where $\hat{G}(\mathbf{x})$ is the unique solution to

$$\Delta\hat{G} = \frac{1}{|\Omega|}\,, \quad \mathbf{x}\in\Omega\,; \qquad \partial_n\hat{G} = \frac{1}{|\partial\Omega|}\,, \quad \mathbf{x}\in\partial\Omega\,; \qquad \int_{\partial\Omega}\hat{G}\, d\mathbf{x} = 0\,. \tag{B.3}$$

As we now show, G_N is related to the traditional Neumann Green's function G of (2.6) by

$$G_N(\mathbf{x};\mathbf{x}_0) = G(\mathbf{x};\mathbf{x}_0) + c\,, \tag{B.4}$$

where c is a constant, which is independent of $\mathbf{x}_0$. To establish this result, we first need the following simple lemma:

Lemma B.1 *For $\mathbf{x}_0\in\Omega$, let $G_N(\mathbf{x};\mathbf{x}_0)$ satisfy (B.2). Then, $\int_\Omega G_N(\mathbf{x};\mathbf{x}_0)\, d\mathbf{x}$ is a constant, independent of $\mathbf{x}_0$.*

Proof: Let $\boldsymbol{\xi}\in\Omega$. We use Green's identity to calculate $0 = \int_\Omega G_N(\mathbf{x};\mathbf{x}_0)\left[\Delta G_N(\mathbf{x};\boldsymbol{\xi}) - \frac{1}{|\Omega|} + \delta(\mathbf{x}-\boldsymbol{\xi})\right] d\mathbf{x}$, which yields

$$G_N(\boldsymbol{\xi};\mathbf{x}_0) - \frac{1}{|\Omega|}\int_\Omega G_N(\mathbf{x};\mathbf{x}_0)\, d\mathbf{x} = -\int_\Omega \nabla\cdot\left[G_N(\mathbf{x};\mathbf{x}_0)\nabla G_N(\mathbf{x};\boldsymbol{\xi})\right] d\mathbf{x} + \int_\Omega \nabla G_N(\mathbf{x};\boldsymbol{\xi})\cdot\nabla G_N(\mathbf{x};\mathbf{x}_0)\, d\mathbf{x}\,.$$

By using the divergence theorem, together with the condition $\partial_n G_N = 0$ on $\partial\Omega$, we obtain

$$\frac{1}{|\Omega|}\int_\Omega G_N(\mathbf{x};\mathbf{x}_0)\, d\mathbf{x} = G_N(\boldsymbol{\xi};\mathbf{x}_0) - \int_\Omega \nabla G_N(\mathbf{x};\boldsymbol{\xi})\cdot\nabla G_N(\mathbf{x};\mathbf{x}_0)\, d\mathbf{x}\,. \tag{B.5}$$

Since the right-hand side of (B.5) is symmetric in $\boldsymbol{\xi}$ and $\mathbf{x}_0$, owing to the Green's reciprocity condition $G_N(\boldsymbol{\xi};\mathbf{x}_0) = G_N(\mathbf{x}_0;\boldsymbol{\xi})$, we conclude that $\int_\Omega G_N(\mathbf{x};\mathbf{x}_0)\,d\mathbf{x} = \int_\Omega G_N(\mathbf{x};\boldsymbol{\xi})\,d\mathbf{x}$, and so $\int_\Omega G_N(\mathbf{x};\mathbf{x}_0)\,d\mathbf{x}$ is independent of $\mathbf{x}_0$. ■

To complete the justification of (B.4), we suppose that the non-standard normalization condition $\int_{\partial\Omega} G_N(\mathbf{x};\mathbf{x}_0)\,d\mathbf{x} = 0$ holds. Let $G(\mathbf{x};\mathbf{x}_0)$ be the usual Neumann Green's function, satisfying (2.6), for which $\int_\Omega G(\mathbf{x};\mathbf{x}_0)\,d\mathbf{x} = 0$. Then, it is clear that $G_N(\mathbf{x};\mathbf{x}_0) = G(\mathbf{x};\mathbf{x}_0) + c$ where c is a constant. By choosing $c = |\Omega|^{-1}\int_\Omega G_N(\mathbf{x};\mathbf{x}_0)\,d\mathbf{x}$, we have $\int_\Omega G(\mathbf{x};\mathbf{x}_0)\,d\mathbf{x} = 0$. Lemma B.1, however, ensures that c is independent of $\mathbf{x}_0$. This justifies (B.4).

With (B.4), we obtain the following two-term expansion for $G_\kappa(\mathbf{x};\mathbf{x}_0)$:

$$G_\kappa(\mathbf{x};\mathbf{x}_0) \sim \frac{1}{\kappa_0|\partial\Omega|} - \hat{G}(\mathbf{x}) + G(\mathbf{x};\mathbf{x}_0) + c + \mathcal{o}(1) \quad \text{as} \quad \kappa_0 \to 0\,, \tag{B.6}$$

where c is a constant independent of $\mathbf{x}_0$. A similar expansion can be written for the regular part R_κ of G_κ. In this way, we obtain that the Robin Green's matrix $\mathcal{G}_\kappa$ in the limit $\kappa_0 \to 0$ satisfies

$$\mathcal{G}_\kappa = \left(\frac{1}{\kappa_0|\partial\Omega|} + c\right)\mathbf{e}\mathbf{e}^T + \mathcal{G} - \hat{\mathcal{G}} + \mathcal{o}(1) \quad \text{as} \quad \kappa_0 \to 0\,; \qquad \hat{\mathcal{G}} \equiv \hat{\mathbf{G}}\mathbf{e}^T\,, \tag{B.7}$$

where $\hat{\mathbf{G}} \equiv \left(\hat{G}(\mathbf{x}_1),\ldots,\hat{G}(\mathbf{x}_N)\right)^T$, $\mathbf{e}^T = (1,\ldots,1)$, and $\mathcal{G}$ is the usual Neumann Green's matrix. By a similar procedure, we calculate that the limiting behavior for $v_3(\mathbf{x})$ in (2.21) as $\kappa_0 \to 0$ is

$$v_3(\mathbf{x}) \sim \frac{|\Omega|}{|\partial\Omega|\kappa_0} - |\Omega|\hat{G}(\mathbf{x}) + \mathcal{o}(1) \quad \text{as} \quad \kappa_0 \to 0\,. \tag{B.8}$$

Next, we substitute (B.7) and (B.8) into the nonlinear algebraic system (2.23) for the spot strengths to get

$$\mathbf{s} + 2\pi\nu\left[\left(\frac{1}{\kappa_0|\partial\Omega|} + c\right)\mathbf{e}\mathbf{e}^T + \mathcal{G} - \hat{\mathcal{G}}\right]\mathbf{s} + \nu\boldsymbol{\chi} = \sqrt{D}\nu\left[\frac{1}{D}\left(\frac{|\Omega|}{|\partial\Omega|\kappa_0}\mathbf{e} - |\Omega|\hat{\mathbf{G}}\right) + v_b\mathbf{e}\right]. \tag{B.9}$$

Assuming that $\mathbf{s} \sim \mathcal{O}(1)$ in (B.9) as $\kappa_0 \to 0$, the leading-order terms of $\mathcal{O}(\kappa_0^{-1})$ in this expression readily yield that

$$\mathbf{e}^T\mathbf{s} = \frac{|\Omega|}{2\pi\sqrt{D}}\,, \tag{B.10}$$

which is equivalent to the solvability condition (2.4) with $A = 0$ and $E \equiv 1$. Next, we use (B.10) to calculate that

$$-2\pi\nu\hat{\mathcal{G}}\mathbf{s} + \frac{\nu}{\sqrt{D}}|\Omega|\hat{\mathbf{G}} = -2\pi\nu\hat{\mathbf{G}}\mathbf{e}^T\mathbf{s} + \frac{\nu}{\sqrt{D}}|\Omega|\hat{\mathbf{G}} = 0\,.$$

Upon using this relation, in combination with (B.10) to calculate $2\pi\nu c\mathbf{e}(\mathbf{e}^T\mathbf{s})$, we readily observe that (B.9) reduces to the following $N+1$ dimensional nonlinear algebraic system for $\mathbf{s}$ and $\bar{v}$:

$$\mathbf{s} + 2\pi\nu\mathcal{G}\mathbf{s} + \nu\boldsymbol{\chi} = D^{1/2}\nu\bar{v}\mathbf{e}\,; \qquad \mathbf{e}^T\mathbf{s} = \frac{|\Omega|}{2\pi\sqrt{D}}\,, \tag{B.11}$$

where $\bar{v} \equiv v_b - c|\Omega|/D$. This limiting nonlinear system, valid as $\kappa_0 \to 0$, is the same as that given in (2.11) and (2.4) with $A = 0$ and $E = 1$, which pertains to a closed system with Neumann boundary conditions and a spatially uniform bulk feed. Moreover, upon using (B.10), (B.6), and (B.8), we readily derive, for $\kappa_0 \to 0$, that (2.20) reduces to

$$v_e \sim \bar{v} - 2\pi D^{-1/2}\sum_{i=1}^N S_i G(\mathbf{x};\mathbf{x}_i)\,. \tag{B.12}$$

This expression is the same as that given by setting $A = 0$ and $E = 1$ in (2.5) for the closed system.

To examine the slow spot dynamics when $\kappa_0 \to 0$, we use (B.6) and (B.8) in (3.10), which yields that

$$\frac{d\mathbf{x}_j}{d\sigma} = \gamma_j\left[-\frac{|\Omega|}{\sqrt{D}}\nabla_{\mathbf{x}}\hat{G}(\mathbf{x}_j) - 2\pi\left(S_j\nabla_{\mathbf{x}}R_j + \sum_{i\neq j}^N S_i\nabla_{\mathbf{x}}G_{ji} - \nabla_{\mathbf{x}}\hat{G}(\mathbf{x}_j)\sum_{i=1}^N S_i\right)\right]. \tag{B.13}$$

Using the solvability condition (B.10), we observe that the terms in (B.13) involving $\hat{G}(\mathbf{x}_j)$ cancel, leaving

$$\frac{d\mathbf{x}_j}{d\sigma} = -2\pi\gamma_j \left(S_j \nabla_{\mathbf{x}} R_j + \sum_{i\neq j}^{N} S_i \nabla_{\mathbf{x}} G_{ji} \right) . \tag{B.14}$$

This is precisely the ODE system (3.8), where we set $A = 0$ and $v_2 \equiv 0$ in (3.8), corresponding to a closed system with homogeneous Neumann boundary conditions on $\partial\Omega$ and $E \equiv 1$ in Ω.

In summary, we conclude that by taking the limit $\kappa_0 \to 0$ in the DAE system (2.23) with (3.10) for slow spot dynamics, corresponding to letting $\kappa_0 \to 0$ in the Robin boundary conditions of Case II of (1.2), we recover the usual slow spot dynamics associated with a closed system with $\partial_n v = 0$ on $\partial\Omega$ and with constant bulk feed $E \equiv 1$.

Acknowledgments

Justin Tzou was partially supported by a PIMS CRG Postdoctoral Fellowship and M. J. Ward was supported by the NSERC Discovery grant 81541. We are grateful to a reviewer for their detailed comments on the initial manuscript.

References

[1] D. Avitabile, V. Brena-Medina, and M. J. Ward, *Spot dynamics in a reaction-diffusion model of plant root hair initiation*, SIAM J. Appl. Math., to appear, (2017).

[2] H. Berestycki and J. Wei, *On singular perturbation problems with a Robin boundary condition*, Ann. Soc. Norm. Super. Pisa Cl. Sci., 5 (2003), pp. 199–230.

[3] W. Chen and M. J. Ward, *The stability and dynamics of localized spot patterns in the two-dimensional Gray-Scott model*, SIAM J. Appl. Dyn. Sys., 10 (2011), pp. 582–666.

[4] R. Dillon, P. K. Maini, and H. G. Othmer, *Pattern formation in generalized Turing systems: I. Steady-state patterns in systems with mixed boundary conditions*, J. Math. Biol., 32 (1994), pp. 345–393.

[5] A. Doelman, P. Van Heijster, and J. Shen, *Pulse dynamics in reaction-diffusion equations with strong spatially localized impurities*, preprint, (2017).

[6] A. Doelman, P. van Heijster, and F. Xie, *A geometric approach to stationary defect solutions in one space dimension*, SIAM J. Appl. Dyn. Sys., 15 (2016), pp. 655–712.

[7] FlexPDE6, PDE Solutions Inc. URL http://www.pdesolutions.com.

[8] J. Gou and M. J. Ward, *An asymptotic analysis of a 2-d model of dynamically active compartments coupled by bulk diffusion*, J. Nonlinear Sci., (2016), pp. 1–51.

[9] L. Greengard and V. Rokhlin, *A new version of the fast multipole method for the Laplace equation in three dimensions*, Acta Numerica, 6 (1997), pp. 229–269.

[10] H. Ikeda and S. I. Ei, *Front dynamics in heterogeneous diffusive media*, Physica D., 239 (2010), pp. 1637–1649.

[11] D. Iron, J. Rumsey, M. J. Ward, and J. Wei, *Logarithmic expansions and the stability of periodic patterns of localized spots for reaction-diffusion systems in R^2*, J. Nonlinear Sci., 24 (2014), pp. 857–912.

[12] T. Kolokolnikov, M. S. Titcombe, and M. J. Ward, *Optimizing the fundamental Neumann eigenvalue for the Laplacian in a domain with small traps*, Europ. J. Appl. Math., 16 (2005), pp. 161–200.

[13] T. Kolokolnikov, M. J. Ward, and J. Wei, *Spot self-replication and dynamics for the Schnakenberg model in a two-dimensional domain*, J. Nonlinear Sci., 19 (2009), pp. 1–56.

[14] D. Lebiedz and U. Brandt-Pollman, *Specific external forcing of spatiotemporal dynamics in reaction-diffusion systems*, Chaos, 15 (2005), p. 023901.

[15] A. Madzvamuse, A. H. W. Chung, and C. Venkataraman, *Stability analysis and simulations of coupled bulk-surface reaction-diffusion systems*, Proc. Roy. Soc. A, 471 (2015).

[16] P. Maini, J. Wei, and M. Winter, *Stability of spikes in the shadow Gierer-Meinhardt system with Robin boundary conditions*, Chaos, 17 (2009), p. 037106.

[17] Y. Nishiura, *Far-from Equilibrium dynamics: Translations of mathematical monographs*, vol. 209, AMS Publications, Providence, Rhode Island, 2002.

[18] Y. Nishiura, T. Teramoto, and X. Yuan, *Heterogeneity-induced spot dynamics for a three-component reaction-diffusion system*, Comm. Pure. Appl. Anal., 11 (2012), pp. 307–338.

[19] I. Prigogine and R. Lefever, *Symmetry breaking instabilities in dissipative systems. II*, The Journal of Chemical Physics, 48 (1968), pp. 1695–1700.

[20] I. Rozada, S. J. Ruuth, and M. J. Ward, *The stability of localized spot patterns for the Brusselator on the sphere*, SIAM J. Appl. Dyn. Sys., 13 (2014), pp. 564–627.

[21] J. Sherratt, *A comparison of periodic travelling wave generation by Robin and Dirichlet boundary conditions in oscillatory reaction-diffusion equations*, IMA J. Appl. Math., 73 (2008), pp. 759–781.

[22] P. H. Trinh and M. J. Ward, *The dynamics of localized spot patterns for reaction-diffusion systems on the sphere*, Nonlinearity, 29 (2016), pp. 766–806.

[23] J. C. Tzou, A. Bayliss, B. J. Matkwosky, and V. A. Volpert, *Stationary and slowly moving localized pulses in a singularly perturbed Brusselator model*, Europ. J. Appl. Math., 22 (2011), pp. 423–453.

[24] J. C. Tzou, Y. Nec, and M. J. Ward, *The stability of localized spikes for the 1-d Brusselator reaction-diffusion model*, Europ. J. Appl. Math., 24 (2013), pp. 515–564.

[25] J. C. Tzou, S. Xie, T. Kolokolnikov, and M. J. Ward, *The stability and slow dynamics of localized spot patterns for the 3-d Schnakenberg reaction-diffusion model*, SIAM J. Appl. Dyn. Sys. (to appear), (2016), p. 35 pages.

[26] P. van Heijster, A. Doelman, T. J. Kaper, Y. Nishiura, and K. I. Ueda, *Pinned fronts in heterogeneous media of jump type*, Nonlinearity, 24 (2011), pp. 127–157.

[27] V. K. Vanag and I. R. Epstein, *Localized patterns in reaction-diffusion systems*, Chaos, 17 (2007), p. 037110.

[28] M. J. Ward, D. McInerney, H. P., G. D., and P. Maini, *The dynamics and pinning of a spike for a reaction-diffusion model*, SIAM J. Appl. Math., 62 (2002), pp. 1297–1328.

[29] J. Wei and M. Winter, *Spikes for the two-dimensional Gierer-Meinhardt system: The weak coupling case*, J. Nonlinear Sci., 11 (2001), pp. 415–458.

[30] ——, *Asymmetric spotty patterns for the Gray-Scott model in R^2*, Studies in Appl. Math., 110 (2003), pp. 63–102.

[31] ——, *Existence and stability of multiple spot solutions for the Gray-Scott model in R^2*, Physica D, 176 (2003), pp. 147–180.

[32] ——, *Stationary multiple spots for reaction-diffusion systems*, J. Math. Biol., 57 (2008), pp. 53–89.

[33] ——, *On the Gierer-Meinhardt system with precursors*, DCDS-A, 25 (2009), pp. 363–398.

[34] ——, *Spikes for the Gierer-Meinhardt system with discontinuous diffusion coefficients*, J. Nonlinear Sci., 12 (2009), pp. 301–339.

[35] ——, *Mathematial aspects of pattern formation in biological systems*, vol. 189, Applied Mathematical Sciences Series, Springer, 2014.

[36] S. Xie and T. Kolokolnikov, *Moving and jumping spot in a two dimensional reaction diffusion model*, submitted, Nonlinearity, (2016).

[37] A. Yochelis and M. Sheintuch, *Principal bifurcation and symmetries in the emergence of reaction-diffusion-advection patterns on finite domains*, Phys. Rev. E., 80 (2009).

[38] X. Yuan, T. Teramoto, and Y. Nishiura, *Heterogeneity-induced defect bifurcation and pulse dynamics for a three-component reaction-diffusion system*, Phys. Rev. E., 75 (2007).